Universidad Nacional Autónoma de México

Programa de Maestría en Ciencias Físicas
Instituto de Física

GEANT4 simulations for the calibration of the SBC detector using photonuclear sources

T E S I S

que para optar por el grado de

Maestro en Ciencias Físicas

PRESENTA:
Óscar Iván Valdés Martínez

Tutor Principal:
Dr. Eric Vázquez Jáuregui
Instituto de Física - UNAM

Ciudad de México, México. 2024

PROTESTA UNIVERSITARIA DE INTEGRIDAD Y HONESTIDAD ACADÉMICA Y PROFESIONAL
(Graduación con trabajo escrito)

De conformidad con lo dispuesto en los artículos 87, fracción V, del Estatuto General, 68, primer párrafo, del Reglamento General de Estudios Universitarios y 26, fracción I, y 35 del Reglamento General de Exámenes, me comprometo en todo tiempo a honrar a la Institución y a cumplir con los principios establecidos en el Código de Ética de la Universidad Nacional Autónoma de México, especialmente con los de integridad y honestidad académica.

De acuerdo con lo anterior, manifiesto que el trabajo escrito titulado:

GEANT4 simulations for the calibration of the SBC detector using photonuclear sources

que presenté para obtener el grado de -----Maestria----- es original, de mi autoría y lo realicé con el rigor metodológico exigido por mi programa de posgrado, citando las fuentes de ideas, textos, imágenes, gráficos u otro tipo de obras empleadas para su desarrollo.

En consecuencia, acepto que la falta de cumplimiento de las disposiciones reglamentarias y normativas de la Universidad, en particular las ya referidas en el Código de Ética, llevará a la nulidad de los actos de carácter académico administrativo del proceso de graduación.

Atentamente

Óscar Iván Valdés Martínez - 522013645

(Nombre, firma y Número de cuenta de la persona alumna)

Para Ezequiel y Juana, más que mi padre y mi segunda madre, mi tata y mi nana.

Agradecimientos

Muchas gracias al Dr. Eric Vázquez Jáuregui por guiarme y presentarme una de las mejores oportunidades de mi vida al introducirme a la física de partículas experimental. Aprecio enormemente todo su apoyo y dedicación a mi formación académica. Lo respeto y admiro mucho, y jamás olvidaré estos últimos años de mi realización como físico.

A mi Madre, no tengo palabras para expresar mi agradecimiento por el apoyo que recibí durante estos dos años. Sé que siempre cuento contigo. Te quiero mucho.

A la colaboración SBC, quedo en deuda con la experiencia que adquirí contribuyendo un grano de arena a este proyecto. Gracias por dejarme participar y por su apoyo continuo en el tema. Lo aprecio mucho. Aprovecho para dar un agradecimiento especial al Dr. Alan Robinson, quien me guió con mucha paciencia en parte de este trabajo.

Debo un agradecimiento a todos los profesores que tuve en el transcurso de esta maestría, en especial al Dr. Alexis Aguilar. Sus cursos fueron fundamentales para mi formación y lo considero uno de los mejores maestros que he tenido.

Amigos del Gallinero, los quiero mucho. Aprecio todas las tardes de trabajo, todos los cafés y todas las galletas que compartimos. En especial, gracias a Rolando, Dana, Camilo, Edmundo y Parce por su apoyo incondicional y hermandad. Los extrañaré mucho.

Este trabajo fue realizado gracias al apoyo del Consejo Nacional de Humanidades, Ciencia y Tecnología (CONAHCyT) proyecto CONAHCyT CB-2017-2018/A1-S-8960, al Programa UNAM-PAPIIT IN108020 y IN105923 y a la beca para posgrado CONAHCyT. Sin su apoyo este trabajo no hubiese sido posible.

Agradezco profundamente a la Universidad Nacional Autónoma de México y al Instituto de Física por brindarme la mejor formación académica y por su constante apoyo en mi educación. En particular, deseo expresar mi más sincero agradecimiento al Programa de Apoyo a los Estudios de Posgrado (PAEP) por su respaldo para asistir a la escuela de verano "14th International Neutrino Summer School" en Fermilab, Batavia, Illinois, Estados Unidos. Esta experiencia fue inolvidable y de un valor incalculable para mi desarrollo académico.

Contents

List of Figures

List of Tables

1 Introduction

In the last century, the enigma of dark matter has loomed large in the field of particle physics. Proposed in 1937 [1] and subsequently integrated into cosmological models [2], dark matter remains a profound mystery, defying resolution. A large number of detection strategies hinge on the possibility that it may consist of weakly interacting massive particles, particles that interact rarely with standard model particles through the weak force [3].

Directly measuring dark matter necessitates highly sensitive detectors capable of detecting low-energy nucleus recoils, similar to the requirements for detecting low-energy neutrinos through Coherent Elastic Neutrino Nucleus Scattering [4]. Neutrino physics has witnessed significant progress in recent years, marked by discoveries like the tau neutrino [5], neutrino oscillations [6, 7], experimental bounds of the mass spectrum [8, 9], and both direct and indirect detections [10, 11, 12, 13]. These advancements have enriched our understanding of particle physics and offered insights into phenomena beyond the standard model.

Liquid-noble bubble chambers hold promise as a technology for measuring low-energy nuclear recoils in the context of these studies [14]. Many dark matter candidates fall within the 1–10 GeV mass range [15], producing nuclear recoils of a few keV. This methodology may also reveal novel nuclear recoil statistics originating from reactor antineutrinos, which exhibit notable differences from neutrinos produced by other sources, thus opening doors to the exploration of new physics [16].

The Scintillating Bubble Chamber (SBC) collaboration is presently developing a 10-kg liquid-argon bubble chamber detector with an expected sub-keV nuclear recoil threshold for future versions [17]. These chambers offer scalability and effective background noise reduction, rendering them suitable for detecting dark matter and neutrino signals with minimal background. However, accurate data interpretation necessitates meticulous calibration techniques. The most promising calibration channel involves low-energy neutrons.

Neutrons, being uncharged and sharing a mass similar to WIMP-like particles, can potentially mimic nucleus-WIMP interactions. Low-energy neutrons can probe nucleation events close to the threshold limits, enabling proper calibration and the ability to build a detector response function [18]. This presents an experimental challenge, requiring the generation of a consistent flux of mono-energetic neutrons to establish correct calibrations. To induce nucleus-recoil events of a few keV for detector testing, we turn to the analysis of photonuclear reactions. These processes, within a specific energy range, can reliably produce low-energy neutrons [19]. Their efficacy relies on the careful study of photon sources, which inherently provide the energy range necessary for nucleus-recoil events [20].

To obtain preliminary statistics and theoretical insights based on the detector's geometry and potential interactions, we can employ simulations using the GEANT4 toolkit. These simulations offer valuable information about expected results and the potential for discovering new, unconsidered interactions. Nevertheless, even well-established simulation tools may introduce errors or unrealistic results, underscoring the importance of thoroughly understanding and validating these simulations to align with the practical goals of the detector [21].

This work provides a quick overview of dark matter, focused in WIMP detection via nucleus scattering, the SBC-LAr10 detector, and calibration schemes based on low-energy neutrons.

It focuses on the photonuclear reaction $^{9}\mathrm{Be}(\gamma, n)^{8}\mathrm{Be}$ as the neutron source and presents a thorough numerical analysis of the reaction and neutron energy. The challenge lies in achieving realistic simulations. Two approaches are considered for accurate identification with the use of updated GEANT4 libraries: a neutron generator with variables derived from theoretical calculations with biased angular distribution, and with an isotropic emission.

Exploring neutron interactions with liquid-argon enables us to identify potential calibration channels, multiplicities, interaction points within the detector, and, most importantly, the expected nucleus-recoil energy event rates. This latter aspect forms the crux of our research.

In this thesis, we commence by contextualizing the imperative need for low-energy nucleus recoil detectors within the framework of neutrino and dark matter theories. Subsequently, we delve into the SBC collaboration's new detector, the SBC-LAr10, offering a comprehensive inspection and technical overview. Following this, we analyze neutron sources for calibration, and finally, we present simulation schemes within GEANT4 alongside their corresponding results.

2 Dark Matter and Neutrinos

For the past half-century, dark matter has stood as one of the most profound mysteries in modern particle physics. Its inception can be traced back to its proposal proposal in 1937 [1], followed by its integration into the cosmological model [2]. Despite decades of research, dark matter remains an unsolved puzzle awaiting a definitive solution. In the realm of dark matter detection, arguably the most explored scenario is the existence of Weakly Interacting Massive Particles [3]. If they indeed constitute dark matter, they interact with Standard Model particles through the weak force, albeit extremely rarely. An alternative possibility, in a less optimistic scenario, is that dark matter belongs to the category of Feebly Interacting Massive Particles (FIMPs). In this case, the interaction mechanism is unknown, with the best chance of interaction involving the exchange of a known or unknown mediator with an standard model nucleus, but with a coupling much weaker than the weak interaction itself [22]. To directly measure weakly interacting massive particles, highly sensitive detectors are imperative, specifically those capable of detecting low-energy nucleus recoils. The requirements for such detectors are reminiscent of those needed for the detection of low-energy neutrinos through Coherent Elastic Neutrino Nucleus Scattering (CEνNS) [3]. Neutrino physics has emerged as one of the most successful and dynamic fields within particle physics over the past century. Significant achievements, such as the discovery of the tau neutrino [5], the revelation of neutrino oscillations [6], precise mass measurements [8, 9], and both direct and indirect detection methods [10, 11, 12], have not only enhanced our comprehension of particle physics but also unveiled cracks in the Standard Model. This chapter delves into a comprehensive exploration of neutrinos and weakly interacting massive particles, recognizing the parallels between them. The focus is on their interactions, with particular emphasis on the utilization of bubble chamber detectors for detection.

2.1 Neutrino Physics

Neutrinos convey a profound key to testing the fundamental laws of particle physics. Probing neutrino interactions and their properties offers exciting prospects to test the Standard Model and potentially usher into new theories in Beyond the Standard Model (BSM) physics. In this century alone, the study of neutrinos has yielded discoveries that have fundamentally reshaped our comprehension of particle physics. A landmark achievement was the identification of the tau neutrino, the last missing piece in the neutrino family. This confirmation marked a significant milestone, affirming the existence of all three neutrino flavors [5]. Equally groundbreaking was the confirmation of neutrino oscillations, which provided the first concrete evidence of neutrino mass, forcing theorists to rethink the otherwise well-established standard model [6, 7]. This discovery instigated a reevaluation of the fundamental properties of these particles. Subsequent precise measurements of neutrino mass differences and mixing angles, including contributions from the Planck collaboration [9], have further refined our understanding of neutrino oscillations. Additionally, neutrinos have been detected from diverse cosmic sources such as the Sun and supernovae, offering invaluable insights into astrophysical processes [23]. The ongoing exploration of neutrinos continues, holding the promise of unveiling further revelations about the nature of the universe. Since Pauli's proposition [24] and its eventual discovery by Cowman and Reines [25], physicists have engaged with the challenge of detecting neutrinos. This ongoing pursuit has led to the achievement of neutrino detections through several weak-interaction processes.

2.1.1 Neutrino Interactions

When tackling the possible neutrino processes, it's important to notice that energies determine the available interactions, and therefore, the required experimental technique. We characterize their interactions by the weak interaction mediators. Charged Current (CC) interactions occur by the exchange of a $W^{\pm}$ boson, while Neutral Current (NC) interactions via Z bosons. The key characteristic between the two is that in CC processes, a (anti)neutrino can change into an (anti)lepton, while in a NC interaction, for the most part, neutrinos only participate in an elastic scattering. To highly this, we will briefly discuss the main neutrino interactions and their properties and experimental opportunities [26]. Figure 1 has the corresponding Feynman diagrams for every process.

CC + NC Elastic Neutrino-Electron Scattering

$$\nu_\ell + e^- \to \nu_\ell + e^- \tag{2.1}$$

This process occurs when a neutrino (of any flavor) scatters elastically with an electron. The experimental threshold energy for this process is at the scale of hundreds of keV, making it a great interaction to probe for solar neutrinos. When the neutrino is of the electron kind, both charged and neutral current interactions add up to the total cross-section of the process. In the case of any other neutrino flavor, only the NC process occurs. As one can expect, the cross-section for these processes is extremely small[1]. The cross-section is on the order of 10^{-46} and it scales approximately linearly with energy. The cross-section differs for anti-neutrino by being smaller, the ratio between $\bar{\nu}_e + e^- \to \bar{\nu}_e + e^-$ to $\nu_e + e^- \to \nu_e + e^-$ is approximately 40%. For the scattering of other neutrinos flavors off electrons, this becomes nearly 20% smaller than the latter.[27].

CC Quasi-Elastic Neutrino-Nucleus Scattering

$$\nu_\ell + n \to p + \ell^- \qquad \text{or} \qquad \bar{\nu}_\ell + p \to n + \ell^+ \tag{2.2}$$

This interaction serves as an approximate model of a neutrino-nucleus interaction, with the complete description of this process often posing significant modeling challenges. Nevertheless, under specific conditions, it becomes achievable to approximate this process by considering a proton or neutron as a composite of three unbounded quarks. In essence, what happens is a quark flavor change through a CC interaction. It's worth noting that this simplification isn't universally applicable; for a comprehensive understanding of a neutrino-nucleus CC interaction, the internal interactions between quarks and gluons must be considered. At intermediate energy scales, it is permissible to make approximations that neglect these underlying structures, enabling the treatment of the interaction between the nucleus and neutrino as an effective process. The interaction involving the anti-neutrino is commonly referred to as *inverse beta decay* and stands as one of the fundamental interactions in neutrino detection. The minimum required energy for these processes varies depending on the type of lepton one aims to detect. For electron detection, electron-neutrinos need to possess a mere few keV of energy, whereas, for muon detection, the corresponding neutrino energy must be on the order of hundreds of MeV. The advantage of this process is evident as it finds application in various contexts, including collider experiments, solar observations, supernova

[1] A recurring theme for all neutrino interactions

studies, and reactor neutrino research [28]. Notably, the existence of muon neutrinos was confirmed through this very process by Lederman, Danby, Gaillard, and their collaborators [29].

CC Deep Inelastic Neutrino Nucleus Scattering

$$\nu_\ell + X \to \ell^- + X' \qquad \text{or} \qquad \bar{\nu}_\ell + X \to \ell^+ + X' \tag{2.3}$$

At high energies, neutrinos are not only capable of changing the flavor of the quarks via a CC interaction but are also capable of shattering the nucleus into different hadrons. This process is the most problematic to model since the internal structure and interactions of the nucleus are not well-known. Usually, for this scattering, energies above 1 GeV are required [13]. Before the starting scaling of this process, an intermediate well-known resonance interaction occurs. The production of pions in the scattering process. We call this **Resonance-Elastic Scattering** [30]. Figure 2 highlights this resonance that starts below the Deep-Inelastic energy scaling. The best sources to test this interaction are colliders and ultra-energetic atmospheric neutrinos.

All of the mentioned interactions share the necessity for medium to high energy scales (excluding the neutrino-electron scattering), a method to probe low-energy neutrinos is via a NC elastic scattering of a nucleus. Up next we will discuss this process in detail.

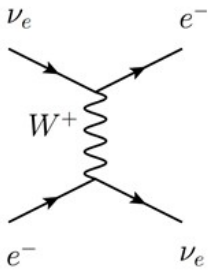

(a) Neutrino-Electron Scattering

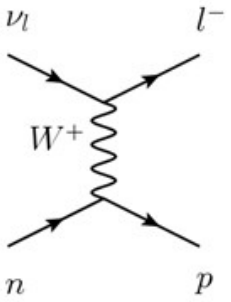

(b) Quasi-Elastic Neutrino Nucleus Scattering

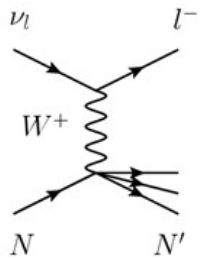

(c) Deep Inelastic Neutrino Nucleus Scattering

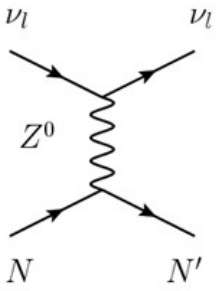

(d) Coherent Elastic Neutrino Nucleus Scattering ($N = N'$)

Figure 1: Feyman Diagrams from Neutrino-Electron Scattering, Quasi-Elastic Neutrino Nucleus Scattering, Deep Inelastic Neutrino Nucleus Scattering and Coherent Elastic Neutrino Nucleus Scattering.

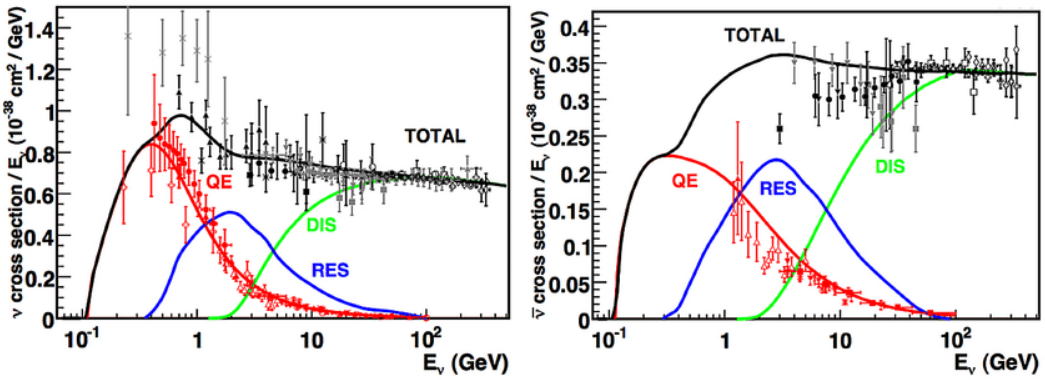

Figure 2: Total Neutrino-Nucleus Cross-Section Measurements with different interaction channels. Red: Quasi-Elastic Scattering, Blue: Resonant-Elastic Scattering and Green: Deep-Inelastic Scattering. Left: Antineutrino data. Right: Neutrino data. Taken from: [31].

Looking at Figure 2, we can identify that most CC neutrino-interaction channels start to acquire a significant cross-section at energies above ≈ 500 MeV. At low energies, the most probable neutrino interaction is the process described in Figure 1 d). This is important to notice since we can conclude that at energies below high-energy thresholds quasi-elastic and deep-inelastic scattering will not be occurring. Neutrino-Electron interaction also scales up with energies but does have a considerable low-energy cross-section. For this work, we will focus only on the neutrino-nucleus low-energy interaction. This will become apparent when discussing detection techniques.

2.1.2 Coherent Elastic Neutrino Nucleus Scattering

Coherent Elastic Neutrino Nucleus Scattering (CEνNS) is a neutral current interaction in which the neutrino is scattered coherently by all the nucleons in a nucleus, depositing some of its incoming energy into them. The required energy for this process must be below 50 MeV. At this scale, the neutrino sees a nucleus as a point-like particle, i.e. the effect of the internal structure of the nucleus can be neglected [32]. The Standard Model cross-section is

$$\frac{d\sigma}{dT} = \frac{G_F^2}{2\pi} M_N Q_W^2 \left(2 - \frac{M_N T}{E_\nu^2}\right) F^2(q^2), \tag{2.4}$$

where E_ν is the neutrino energy, T is the nuclear recoil energy, M_N and $F(q^2)$ are the nucleus mass and form factor respectively and $Q_W = Z g_p^V + N g_n^V$ is the weak nuclear charge, with N, Z the proton and neutron numbers of the detector, $g_p^V = 1/2 - 2\sin^2\theta_W$ and $g_n^V = -1/2$. The form factor is equal to 1 under the low momentum transfer and coherent approximations of neutrino interaction with the nucleus. Under this limit, an enhancement of the cross-section is achieved by a scaling of N^2 due to the weak charge [33]. This is given the accidental suppression of the proton weak charge [32]. Thus, CEνNS cross-section becomes more sensitive to the neutron distribution of the nucleus under the coherent approximation.

A CEνNS detector stands as a valuable tool for investigating low-energy neutrino sources, with nuclear reactor anti-neutrinos and low-energy cosmological neutrinos being the most prevalent examples. The exploration of CEνNS offers multifaceted benefits to the field

of neutrino physics. Notably, it provides a strong method to measure the weak mixing angle under low-momentum transfer conditions, thereby serving as an additional mean to scrutinize the Standard Model [33]. A comprehensive grasp of these interaction signals holds significant importance in the search for Weakly Interacting Massive Particle (WIMP) dark matter candidates. CEνNS signals can become a critical source of background in such searches, often challenging to distinguish from genuine dark matter signals. This emphasizes the vital role CEνNS plays in ongoing efforts to identify dark matter candidates. In the field of astrophysics, CEνNS assumes a key role in the study of solar and supernova neutrinos, aligning perfectly with the coherent scattering criterion. Consequently, CEνNS serves as an ideal avenue for investigating neutrino interactions in these astrophysical contexts [34].

The COHERENT collaboration was able to detect neutrinos via CEνNS for the first time in 2017 [4] by using a CsI scintillating detector. Figure 3 highlights these results.

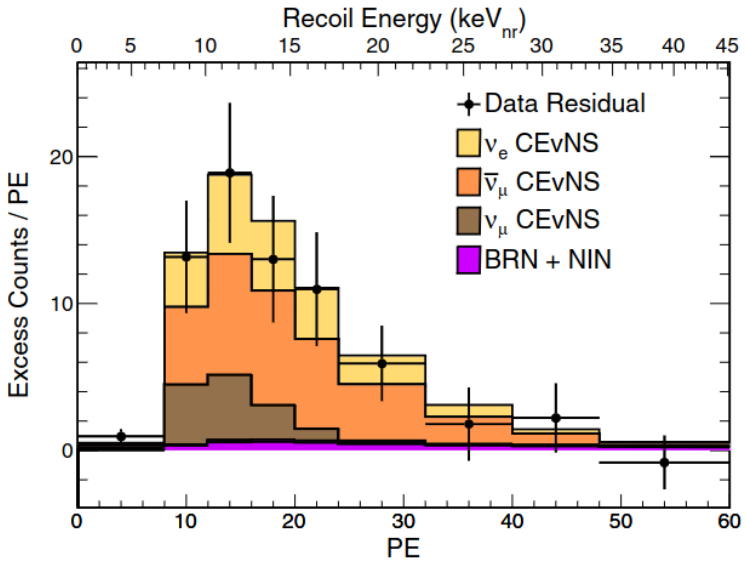

Figure 3: COHERENT Collaboration 2022 results for CEνNS measurements in a CsI scintillating detector. x-axis is the photo-electrons from the scintillation and y-axis the count rate per photo-electron. Upper x-axis shows a the expected recoil energy from xenon nucleus's. BRN (Beam Related Neutrons) + NIN (Neutrino-induced Neutrons) are the expected background counts. Taken from: [4].

The forthcoming chapter delves into a comprehensive examination of bubble-chamber detectors, overviewing the design and functionalities of these tools in neutrino detection. This analysis will preview the inner workings of these detectors, providing valuable insights into their applications and relevance in the realm of experimental particle physics.

Furthermore, it's worth noting that low-energy neutrino detection experiments can often exhibit striking resemblances to direct dark matter detection efforts. The subtle nuances of these experiments and their potential to mimic the signals of dark matter candidates will be explored in detail. This discussion will illustrate the intersections and distinctions between these two domains, offering a richer understanding of the challenges and opportunities they present. In the subsequent section, we review a dark matter candidate, commenting on its properties, theoretical implications, and the experimental methods employed to probe its existence.

2.2 Weakly Interacting Massive Particles

Since the latter half of the 20th century, the enigma of dark matter has been a prevalent problem in the fields of cosmology and particle physics. The existence of mass that appears to remain non-interacting with any known particles has puzzled physicists for decades. Extensive experiments have been conducted to explore their interactions with Standard Model particles, but these have yielded no conclusive results. The most promising hypothesis is that these mysterious particles are *Weakly Interacting Massive Particles* (WIMPs), meaning they are massive particles that interact primarily through the weak force [3]. Various models, based on cosmological observations [22], have provided insights into the potential mass range of WIMPs, spanning a wide spectrum. For our current discussion, our focus centers on masses within the range of 1-10 GeV [15], which will be contextualized in the forthcoming subsections.

Numerous dedicated experimental efforts have been embarked on to probe interactions between WIMPs and nucleons. Unfortunately, the outcomes of these researches have consistently delivered negative results. These persistent findings have led to the establishment of exclusion zones, a concept pivotal to the field of dark matter research. Exclusion zones delineate the regions of WIMP-nucleon parameter space where interactions are disallowed due to the absence of any positive detection signals. As shown in Figure 4, these exclusion zones vividly depict the boundaries within the parameter space of cross-sections relevant to interactions involving GeV-scale WIMPs and nucleons. This graphic representation shows the collective efforts and pursuits of experimental studies aimed at dark matter detection. The presence of exclusion zones underscores the precision and rigor of these experiments and also emphasizes the crucial need for innovative strategies and technologies to explore new frontiers in the ongoing search.

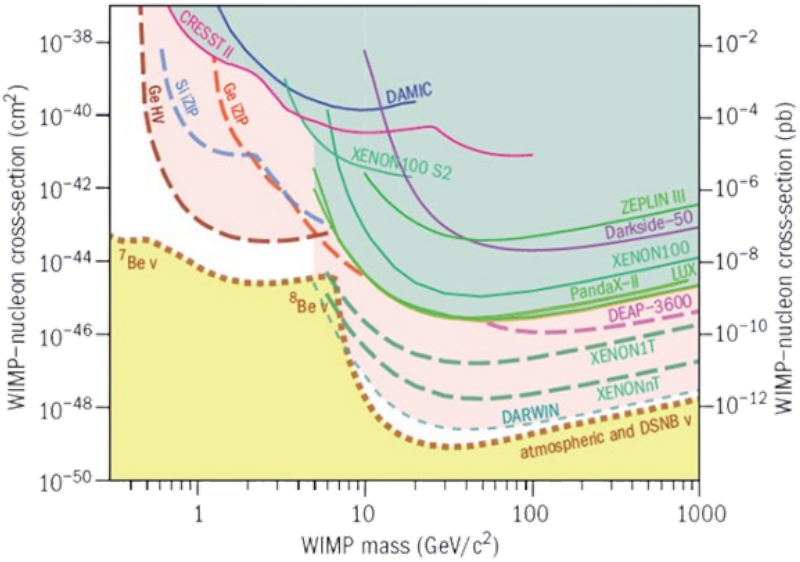

Figure 4: Current bounds for GeV-mass WIMP-nucleon cross-section. Curves are at a 90% C.L. Dotted Lines are expected future results. Taken from: [35].

If a WIMP exists and remains stable, it naturally possesses a relic density that matches the requirements for dark matter. This phenomenon, often termed the "WIMP miracle" suggests

that particles driven by the gauge hierarchy problem, a purely microphysical puzzle, make for strong contenders as dark matter candidates. This implies that dark matter could have originated simply and predictably as a thermal relic of the Big Bang [22].

During this chapter we will discuss WIMP interactions with matter and the expected rates of detection, this includes a review on the experimental requirements for detection.

2.2.1 Interaction with Matter

Similar to neutrino-nucleus interactions, the notion of considering a collision between dark matter and standard model particles seems like a viable option. For inelastic collisions, it is necessary to have at least two dark matter particles, thus, the interaction will look like the following,

$$\mathcal{X} + X \to \mathcal{X}' + Y, \tag{2.5}$$

where X and Y are standard model particles and $\mathcal{X}$ and $\mathcal{X}'$ are dark matter particles. This process can be seen as an inverse beta decay involving a certain dark matter and standard model particle. The theoretical exploration of elastic scatterings in this context has encountered problematic implementation, as elaborated in [3]. An alternative detection method, similar to neutrino interactions, involves the inelastic scattering off a nucleus. This process looks like the following:

$$\mathcal{X} + X \to \mathcal{X} + X. \tag{2.6}$$

While the theoretical models become more exploitable, as just one DM particle is required, the experimental setups for measuring become harder. Considering the process under the Ansatz that this kind of dark matter particles are WIMPs, using the Fermi low-energy transfer approximation, we can find an estimate of WIMP-nucleon cross-sections for masses $m_{\mathcal{X}} \geq m_n \approx 1$ GeV to be

$$\sigma_{\mathcal{X}n} \approx 10^{-37}\ \text{cm}^2 \tag{2.7}$$

This cross-section can be amplified when considering a nucleus with A number of nucleons and the assumption that the interaction is coherent. Hence, at a simple approximation, the WIMP-nucleus cross-section is

$$\sigma_{\mathcal{X}N} = \sigma_{\mathcal{X}n} A^2 \tag{2.8}$$

This approximation neglects several other coupling possibilities, like internal nucleus interactions and spin dependency [36]. Theories about these dependences can be found in [3]. In the case of equation 2.8, we consider it an approximate spin-independent WIMP cross-section[2]. The mentioned processes (both inelastic and elastic) are considered *direct detection*, and it stems from the observation of residual particles after the scattering. Meanwhile, we call *indirect detection* to the processes in which the residual or incoming particles are not detectable. For example, a dark matter collision resulting in a SM-pair creation scattering and vice-versa. While an interesting focus of experiment construction, for the presented work, we will focus on direct detection processes only.

2.2.2 Detection and Interaction Rates

When dealing with the inelastic scattering of a nucleus, it is essential to carefully design experiments that specifically target the measurement of the kinetic energy of the scattered

[2]This is the case of the plotted bounds in Figure 4.

nucleus. The effectiveness of WIMP detection heavily relies on sensitivity and resolution, necessitating a thorough understanding of the expected interaction and detection rates as per the underlying theory. In this context, we aim to illustrate the concept by making simplified assumptions and estimating interaction rates. The maximum nucleus recoil energy can be calculated via simple non-relativistic kinematics. References [37, 38] addresses the cosmological implications and predictions of WIMPs kinematic expectations. Thus, the maximum kinetic energy a nucleus can acquire by the elastic collision of a WIMP particle is:

$$E_{\max} = \frac{(2m_{\mathcal{X}}v)^2}{2m_N}, \tag{2.9}$$

where v is the velocity of the WIMP particle and $m_{\mathcal{X}}$ and m_N are the WIMP and nucleus mass respectively.

By considering an energy threshold denoted as E_{th} for a nucleus-recoil detector, we can derive an approximate velocity-mass relationship necessary for an event to be successfully registered. Typically, these energy thresholds are on the order of fractions of keV, implying that, under the assumption of a WIMP mass around 1 GeV, the corresponding velocity required falls within the range of 500-700 km/s. It's worth noting that for lighter WIMPs, the energy recoil diminishes to the point of being impractical for measurement. Consequently, we can deduce that, given the current state of experimental capabilities, nucleus recoils resulting from WIMP-like events should manifest within the keV energy range, necessitating the WIMP mass to be on the GeV scale, as elaborated in [39].

Since we established the required mass scale, a simple rate of detection calculation given an approximate flux and density can be made. Stefano argues in [3] that an approximate detection rate is

$$R = \frac{0.06}{\text{kg day}}\left(\frac{100}{A}\right)\left(\frac{\sigma}{10^{-38}\text{ cm}^2}\right)\left(\frac{\rho_{DM}}{0.3\text{ GeV/cm}^3}\right)\left(\frac{v}{200\text{km/s}}\right), \tag{2.10}$$

under the approximation that dark matter flux can be expressed as $\phi = v\rho_{DM}/m_{\mathcal{X}}$, where ρ_{DM} is the relic density of dark matter, v the velocity and $m_{\mathcal{X}}$ the mass of the particle. Thus the rate of detection can be expressed as the flux multiplied by the expected cross-section and the number of nucleons A expected in a kilogram of detection material. Examining Equation 2.10, considering a liquid-argon target of 10 kg, with an atomic mass $A = 40$, and assuming a typical WIMP velocity of approximately 500 km/s, along with a density of 0.3 GeV/cm^3 as per the anticipated Dark Matter density in the sun [22], and employing a standard cross-section for interaction on the order of 10^{-38} (in an optimistic scenario), the expected detection rate amounts to approximately 4 events per day[3].

This rate is extremely low compared to natural sources of radioactivity present in everyday objects. A lot of factors can create nuclear recoils, alpha particles, neutrons, electrons, cosmic muons, etc. The rate of production and interaction sit well above the simple calculation made above. Thus, dark matter detection needs to be isolated from backgrounds as much as possible. The main challenge of a dark matter detector is to have the most background-free environment. Physicists have developed creative techniques to suppress or identify as many signals as possible, from supermassive detectors deep underground [40], to periodical modulation due to earth's rotation [41], to the sun's motion about the galaxy [42], and more.

[3] Under highly optimistic assumptions

While Equation 2.10 serves as a valuable approximation for dark matter detection, a more comprehensive formulation is required to provide a better assessment of the detection rate. To achieve a precise characterization of the detection rate, it's crucial to express the rate of scattered events per unit of time, energy, and mass in terms of the nucleus recoil energy. This is similar to Equation 2.10, where we multiplied the number of target nuclei by the average flux of dark matter particles to find the number of detections per day. The flux inherently represents the average number of dark matter particles multiplied by their velocities, all further multiplied by the cross-section of the energy recoil of a nucleus. It's important to note that the cross-section is expected to be velocity-dependent. Consequently, the total detection rate per nucleus recoil energy can be expressed as follows:

$$\frac{dR}{dE_R} = N_T \; n_{\mathcal{X}} \left\langle v_{\mathcal{X}} \frac{d\sigma}{dE_R} \right\rangle. \tag{2.11}$$

The nucleus recoil energy can be found explicitly via kinematics and conservation of momentum in a center-of-mass frame. Thus

$$E_R = \frac{\mu_T^2}{m_T} v_{\mathcal{X}}^2 (1 - \cos\theta), \tag{2.12}$$

where, μ_T is the reduced mass of the nucleus and dark matter particle, m_T is the nucleus mass and θ is the scattering angle. The latter, in a minimum transfer approximation (i.e $\theta = 0$) provides certain boundaries in dark matter mass and velocities [37]. This play of variables can be shown as follows

$$v_{\mathcal{X}}^{\min} = \sqrt{\frac{m_T E_R}{2\mu_T^2}} \tag{2.13}$$

This proves useful for understanding the relation between the minimum velocity, energy recoil thresholds, and mass. For example, for low dark matter masses, (i.e. $m_T >> m_{\mathcal{X}}$) the velocity needs to increase to keep the same energy threshold. We can conclude then, that the velocity of the particle with respect to the energy threshold must be inversely proportional to the WIMP mass. This makes sense, as one expects a large massive particle to be able to deposit energy more easily with a smaller velocity than its counterpart. To constrain the event rate per recoil energy, it's convenient to express it over a continuous range of velocities, it is highly unlike that all dark matter particles are inciting with the same velocity. For this, given the relationship between recoil energy, velocity, and scattering angle, we can differentiate equation 2.12 with respect to $\cos\theta$ and find that $dE_R = (d\cos\theta)(\mu_T^2/m_T)v^2$. Considering bias in the velocity as a radial function [43], the full rate event per nucleus recoil energy as a function of the differential cross-section can be written as

$$\frac{dR}{dE_R} = N_T \; \frac{\rho_{DM} m_T}{m_{\mathcal{X}} \mu_T^2} \int_{v_{\min}}^{v_{\max}} d^3v \frac{f(v)}{v} \frac{d\sigma}{d\cos\theta} \tag{2.14}$$

where $f(v)$ is a dark matter halo velocity probability distribution. Up to this moment, we have focused on just two different things, the expected event rate and the difficulty of creating a free background environment. There is plenty more literature about the internal processes of the WIMP-nucleus interactions [44], as well as considering as previously mentioned the spin coupling [45]. These derivations and discussions go beyond the scope of this work and are not necessary for the further discussion. Although this method of calculating the rates,

while oversimplified, has served the direct detection community of dark matter to reach a sort of consensus for comparing their observations, it's crucial to acknowledge that employing this framework demands a comprehensive consideration of all the underlying assumptions, some of which are rather crude. However, we highly encourage conducting an in-depth analysis of this theoretical framework. From here on out, we would like to focus more on the experimental challenges and efforts performed for WIMP detection.

2.2.3 Neutrino Floor

WIMP search and neutrino detection are entangled via the sensitivity and resolution of detectors. When probing for WIMP detection, exclusion bounds are set and the necessity for bigger and more sensitive detectors is proposed. However, there exists a threshold of how far we can push for this sensitivity before detectors become filled with backgrounds. Let us talk briefly about neutrino production and continuous sources. Extraterrestrial neutrinos have been detected and have been studied for the last 40 years through the sun's nuclear reactions. Given our known cross-section, the solar model [46] and experiments, the expected neutrino flux is close to 6×10^{10} cm^{-2} s^{-1} [47] in a wide energy spectrum up to 20 MeV's. The supernovae' diffusive neutrino background expected from collapsing cores from all over the galaxy account for an approximate flux of 10 cm^{-2} s^{-1}[48]. Finally, neutrinos are being generated due to the inelastic collision of cosmic rays with our atmosphere [49], the energies of these neutrinos can reach up to 50 MeV and estimates about their production rates predict a flux in the orders of 10^{-1} cm^{-2} s^{-1}. As we can see, there exists a neutrino background that goes up to 50 MeV in energy scales and accounts for flux in the orders of 10^10 cm^{-2} s^{-1}. As we showed in the previous subsection, up to the orders of a couple of MeV, neutrinos can interact elastically with the nucleus coherently. The response function of the detector (energy threshold) is independent of neutrino or WIMP detection. Thus, even when we consider a massive, background-less[4] detector, neutrinos represent a large source of background. To set a perspective, a theorized 5 GeV WIMP scattering of a nucleus produces up to 0.25 keV in recoil energy. A 2 MeV neutrino can produce the same nuclear recoil. This implies that for masses below 10 GeV, solar neutrinos would pose a huge source of background. This becomes a larger problem when we consider detection rates, since SI WIMP-nucleon cross-section are unknown, there exists a limit in which detection rates (i.e. cross-section) becomes identical to neutrinos rates. We call this limit, the neutrino floor. If the WIMP-nucleon cross-section ends up being in this limit, it would be both, exciting and disappointing. Exciting since reaching this level of sensitivity would enhance our knowledge of neutrino physics and help us understand better the interaction of low-energy cosmological neutrinos, disappointing because it would also make direct WIMP detection extremely difficult. New experimental techniques should be developed to achieve this kind of distinction. The main challenge has been to scale up detector target masses while decreasing energy thresholds and eliminating or rejecting backgrounds to a potential signal [50].

Having laid out the basic theoretical ideas for understanding neutrinos and their similarities with WIMPs through nucleus recoil detection, it is natural to delve into the practical aspects of conducting experiments in this field. In the following sections, we will explore the operational principles of liquid-noble detectors, known for their efficiency in measuring low-energy nuclear recoils, with particular emphasis on the Scintillating Bubble Chamber detector.

[4]In this instance, we refer by background-less concerning muons, electrons, neutrons, alphas, etc.

3 The Scintillating Bubble Chamber Detector

The Scintillating Bubble Chamber detector (SBC) is a Liquid-Noble bubble chamber detector currently being built in Fermilab by the SBC collaboration. It consists of a 10 kg Liquid-Argon chamber capable of producing scintillation for low-energy nucleus recoil events. The main physics motivation is low-energy WIMP-nucleus interactions and reactor-neutrino detection via CEνNS [18]. The SBC detector is part of the bubble chamber detector family that has been developed since 2008 [51]. Bubble chambers excel in achieving the most effective discrimination between nucleus and electron recoils. While nucleus scatterings at a specific energy threshold induce the formation of bubbles within the superheated liquid target, electron recoils do not produce such bubbles. This discrimination capability is rooted in the special thermodynamic properties of the target liquid. However, achieving this critical discrimination technique necessitates specific characteristics that can be limited by background-induced electron recoils. The central intent of the SBC is to implement an additional measure to further suppress the production of bubbles triggered by electron recoils. This strategic approach aims to establish an environment characterized by minimal interference from electron recoils, effectively creating a quasi-background-free setting at the energy thresholds relevant to nucleus recoils. This innovative initiative holds the prospect to substantially enhance the detector's operational sensitivity, potentially extending its capabilities by up to one order of magnitude below the current energy thresholds. This section provides an analysis of, liquid-noble or not, bubble chambers, the key operation, and experimental techniques as well as the discrimination of an event. We utilize this prologue to give an overview of the SBC detector and the physics opportunities.

3.1 Bubble Chamber Detectors

A liquid-noble bubble chamber is an upgrade over the more traditional moderately superheated bubble chamber techniques first employed by the COUPP collaboration [51] and now being perfected and utilized by PICO [14]. The target material is a super-heated homogeneous fluid, this is achieved by dropping the liquid pressure below its vapor threshold at a constant temperature. This state is now meta stable (super-heated) and it remains like this for approximately 10 minutes. If a particle with enough energy interacts with a nucleus of the liquid at this stage, a nucleation[1] point is produced, we call this a *proto-bubble*. Within milliseconds this bubble expands to a visible size, this happens until the chamber pressure compresses it, driving the liquid back into a stable super-heated state. We call this process an **event** [17].

As indicated in the chapter's introduction, these detectors inherently exhibit insensitivity to electron recoils due to specific thermodynamic constraints associated with nucleation. The process of nucleation requires an adequate energy input to surmount the free energy barrier stemming from surface tension, ultimately leading to the formation of proto-bubbles. Virtually any interacting particle can impart sufficient energy to the nucleus, locally heating the liquid and instigating proto-bubble creation. This phenomenon is aptly described by the Seitz "Hot-Spike" model [53], which elucidates the underlying physics of liquid nucleation.

[1] In thermodynamics, nucleation is the initial stage in the creation of a new thermodynamic phase or structure through self-assembly or self-organization within a substance or mixture. Nucleation essentially sets the time frame for when the new phase or self-organized structure will emerge, determining the waiting period for an observer [52].

To delve deeper into the intricacies of liquid nucleation, it is imperative that we first provide a comprehensive overview of this model.

3.1.1 Seitz Model

The conditions in which the bubbles grow are defined by the forces acting at the nanoscale. Most importantly, the critical bubble size which is being expanded by a pressure P_b balances with the surface tension (σ) and pressure (P_l). With this play of variables, the condition for which a bubble is capable of continuing to expand is

$$P_b - P_l \geq \frac{2\sigma}{r_c} \tag{3.1}$$

where r_c is the critical radius of the bubble. Given these conditions, it is essential to recognize the existence of a net positive pressure acting upon the bubble of sufficient magnitude to overcome the surface tension of the forming bubble. While this condition holds generality, it allows us to gain valuable insights into the required energy deposition for nucleation to occur [54]. The pressure within the bubble, denoted as P_b, must remain lower than the vapor pressure, P_v, corresponding to the temperature T at which the system operates. This constraint arises from the fact that the vapor within the bubble and its surrounding environment are in a state of chemical equilibrium. Consequently, P_b can be perceived as a perturbation of the vapor pressure P_v [55]. Leveraging Maxwell's relations, we can infer that the change in chemical potential with respect to pressure at a constant temperature is inversely proportional to density. Thus, a perturbation in pressure, as represented by P_b, can be approximated as follows:

$$P_b \approx P_v - \frac{\rho_v}{\rho_l}(P_v - P_l) \tag{3.2}$$

where ρ_v and ρ_l are the saturated vapor and liquid densities of the fluid. In theory, they should be closely similar, hence for practical purposes $P_b \approx P_v$. For the calculation of the critical radius, we can substitute Equation 3.2 in Equation 3.1 and solve for r_c:

$$r_c \approx \frac{2\sigma\rho_l}{(P_v - P_l)(\rho_l - \rho_v)} \tag{3.3}$$

The critical radius is usually in the order of a dozen nanometers. Once the critical radius is defined, it becomes possible to calculate a range of other essential properties. Among the most valuable are the energy and thermodynamic variables. The necessary work to create a bubble can be calculated by integrating equation 3.1 from 0 to the critical radius, thus

$$W_{min} = \int_0^{r_c} 4\pi r^2 dr \left(\frac{2\sigma}{r} - (P_b - P_l)\right) = \frac{4\pi}{3}\sigma r_c^2 \tag{3.4}$$

This result can be understood as a summation of two distinct contributions: a surface energy term and an expansion energy term. The first component, $4\pi\sigma r_c^2$, represents the free energy associated with the surface, while the second term, $\frac{4\pi}{3}(P_b - P_l)r_c^2$, signifies the energy required to expand the superheated fluid as it forms. These combined contributions should be equal to the total surface tension energy expected in the final state. It is crucial to note that the energy expended during the expansion process is drawn from the surrounding regions near the nucleation point, emphasizing that proto-bubbles can exclusively originate in areas

where the surroundings are cooler. Taking this into account, a comprehensive description of the requisite energy can be written as:

$$Q_{Seitz} \approx 4\pi r_c^2 \left(\sigma - T\frac{\partial\sigma}{\partial T}\right) + \frac{4\pi}{3} r_c^3 \rho_b (h_b - h_l) - \frac{4\pi}{3} r_c^3 (P_b - P_l) \tag{3.5}$$

where h_b and h_l are the specific enthalpies of the gaseous and liquid states, respectively, and ρ_b is the density of the bubble. An additional correction term has also been considered in the free surface tension energy $(-T(\partial\sigma/\partial T))$, this way, the total energy of the surface can be captured. This quantity mimics and models with great accuracy the nuclear recoil energy threshold [56].

3.1.2 Electron Recoils

Having conducted this analysis, we can now apply these insights to understand why electron recoils rarely induce nucleation. To perform this, let's introduce a probability function $\mathcal{P}$ that characterizes the likelihood of nucleation as a function of pressure and temperature.

$$\mathcal{P} = Ae^{-Bf(P,T)} \tag{3.6}$$

A, B are free statistical parameters and $f(P,T)$ is a function of pressure and temperature. The number of events is expected to be proportional to the deposited energy, thus, it would not be an absurd conclusion to expect $f(P,T) \approx Q_{Seitz}$, but in practice, it could be proportional to many other thermodynamic properties or energy thresholds and critical radius. It is important to remark that super-heated liquids are extremely sensitive to the position of the energy deposition. This consideration can lead us to analyze the stopping power of electrons. Electrons have a low stopping power and are inefficient at depositing energy in concentrated chunk of space. Considering that the velocities of scattered electrons are in the scales of a few keV's, the required energy deposition for nucleation is not achieved. The Bethe-Bloch equation provides a description of the energy deposited per unit length within a given material. At low energies, even in denser materials, electrons possess a relatively long mean free path, resulting in a gradual energy deposition that is not concentrated at a single point [57]. To illustrate this point, let's examine the energy threshold for nucleation caused by electrons, focusing solely on energy considerations. For this purpose, we introduce a function denoted as $f(P,T)$ with units of dE/dx. We can now define the radius of the liquid containing the molecules that will eventually coalesce to form a critical bubble as:

$$r_l = r_c \left(\frac{\rho_b}{\rho_l}\right)^{1/3} \tag{3.7}$$

Typically, the characteristic length scale, denoted as r_l, falls within the range of 5 to 10 nanometers, which is also the scale at which the energy threshold needs to be reached. Stopping powers exhibit proportionality to material density. When we divide Equation 3.7 by the density, we obtain a fully density-independent stopping power for the fluid. This resultant stopping power is directly proportional to the function $f(P,T)$, as expressed in:

$$f(P,T) \propto \frac{E_{th}}{r_l \rho_l} \tag{3.8}$$

Important to notice that B, from equation 3.6, due to the adimensional requirements, has units of stopping power. Based on the discussions presented, we can analyze how a bubble

chamber detector responds to nucleus recoils by employing gamma sources for scattering. To gauge this response, numerous tests have been conducted under varying thermodynamic conditions, specifically in terms of pressure and temperature, to calibrate the detector. A comprehensive overview of this calibration performance is provided in a study conducted by the PICO collaboration over the course of recent years, as detailed in [56]. The gathered results from these tests, focusing on electron recoil-induced nucleation, are presented in Figure 5. One notable observation is the diminishing probabilities of nucleation as the Seitz energy threshold increases. Attempting to characterize this behavior, a black line representing the probability function for C_3F_8 (as per Equation 3.8) is depicted in the figure. This line diverges from the empirical data as the threshold energy rises. This discrepancy serves as an essential insight into understanding the relatively low production of electron recoil-induced bubbles. However, even though the probability of nucleation is extremely low for low Seitz threshold energies, it is crucial to acknowledge that they can still be considered as a potential source of background noise in the context of bubble chamber experiments.

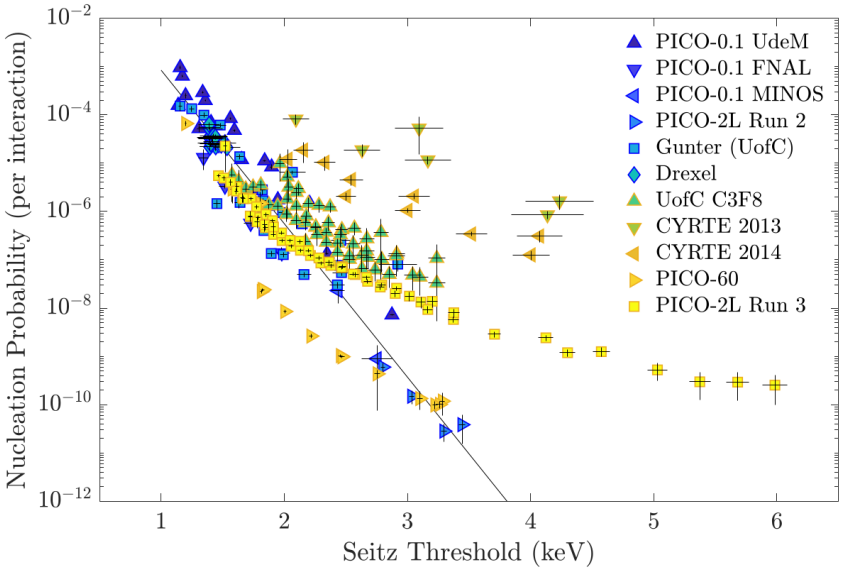

Figure 5: Electron Recoil Bubble Nucleation Probability in C_3F_8, the probability of electron recoil nucleation for a single poton scatter is a function of Seitz threshold only. Model fails to predict nucleation probability as Seitz Thresholds above $\approx$ 3 keV's. Taken from: [56].

3.2 Liquid Noble Detectors

Liquid-noble bubble chambers, such as the SBC, offer a notable advantage over conventional Freon bubble chambers. The crucial distinction lies in their use of liquid scintillator targets. In these detectors, nucleus recoils can generate both bubbles and scintillation, whereas electron recoils exclusively produce scintillation signals. This fundamental divergence facilitates an additional discrimination technique for identifying electron recoil-induced bubbles. The emitted light during scintillation can be precisely quantified to reconstruct the total energy deposited in the detector, achieving resolutions of up to keV. In contrast, traditional bubble chambers rely on acoustic and visual detection methods (cameras) for event reconstruction. The incorporation of scintillation as a third detection channel provides invaluable insights for event reconstruction and enhances the overall capabilities of the detector [18]. Liquid-noble

detectors also have the advantage of running at much lower energy thresholds while remaining nearly blind to electron induced nucleation events. Bubble nucleation by electron recoils has never been observed in pure xenon [58] and has only been detected at extreme super-heat conditions in pure liquid-argon [59]. The absence of electron recoil-induced nucleation is a direct consequence of the lack of molecular degrees of freedom. In the previous sub-section, we discussed how the stopping power was not enough to deposit enough energy to incite the creation of bubbles. In the liquid-noble case, the analysis becomes easier to discuss. Since noble elements do not have any more vibrational degrees of freedom available, the only way to incite energy losses is through the full center of mass elastic collisions, which once again, leads to large stopping power and low-energy deposition efficiency [60]. Instead, the electron recoils energy deposition is mostly carried away by scintillation (like from bremsstrahlung from electron-atom scattering). The thermodynamic limits for which electron recoil-induced bubbles can become a source of background are unknown.

Scintillation brings a new challenge for event reconstruction, this is because a simultaneous nucleation and scintillation from the same event must be detected. In 2016, Northwestern University detected a simultaneous event in a 30-gram xenon bubble chamber [61]. During these tests, additional evidence against electron recoil events was brought to light. This device successfully tested sensitivity to 152 keV neutrons produced by a ^{88}Y/ ^{9}Be source[2], which leads to a maximum nucleus recoil energy of 4.8 keV. This detection and sensitivity also matched with great accuracy the Seitz model, giving a great predictability power, which at certain thermodynamic limits, could reach down to 1 keV. Given all these characteristics, we can discuss the possible sources of background and the techniques for eliminating them.

3.2.1 Quasi-Background Free Strategy

As mentioned, while electron recoils do not pose a significant background, many sources can produce nucleation [62]. All these interactions can bring significant sources of background that need to be studied and suppressed as much as possible. We will discuss this below.

Alpha particles from decay chains can produce nucleation that are indistinguishable from nucleus recoil-induced single-bubbles, even though the deposited energy is up to 1000 times larger than one expected out of nucleus recoils. This event can be identified and veto by the scintillation signal, this has been performed in xenon in [63].

Low-energy alpha particles stemming from the final stages of their decay chains, such as ^{206}Po, may deposit relatively low amounts of energy[3] on the detector's surface, potentially resulting in the formation of isolated bubbles. When this occurs in proximity to the chamber walls, it can be readily identified and dismissed through the use of high-resolution cameras with millimeter precision. To prevent the occurrence of such events, meticulous and thorough cleaning procedures should be diligently executed.

Neutrons represent a significant source of background noise, primarily owing to their evasive nature and challenging control. Fast neutrons, characterized by energies exceeding 1 MeV, can be generated through alpha-nuclear reactions within the detector materials and as a result of cosmic rays interacting with the detector's immediate surroundings. Fortunately, the shielding employed by detectors typically effectively blocks these fast neutrons from

[2]This is a photonuclear reaction, and this process is highly discussed in the next chapter, with a special mention of this reaction in particular. For this context, this reaction creates nearly mono-energetic neutrons.

[3]When referring to "low-energy," we are comparing to the latter case.

infiltrating the sensitive detector region. The remainder of neutrons can be identified by the following technique:

1. By multi-bubble events: The neutron mean free path is around 10 centimeters, so any free neutron that enters the detector geometry is expected to interact a couple of times.
2. Scintillation detection: The latter produces several scintillation signals, if the light emitted is more than the target scintillation detection threshold[4] the event gets disregarded.
3. Material rejection. In addition, if a scintillation is identified from a specific material (n,γ) reaction, the event is not counted.

Point three becomes important when scaling the detector, as additional materials can be added to the detector for improvement in detection. For example: Scintillating thermal and hydraulic fluid and gadolinium-doped materials. Additionally, thermal neutrons[5] can also produce nucleation through a few neutron capture reactions. These events are also heavily suppressed by the detector's shielding and the few that could interact with the target are, just like for fast neutrons, identified by scintillation and surrounding sensitive media by the correlated photons interacting.

Similarly, external high-energy photons (with energies equal to or greater than 1.5 MeV) have the capability to generate single bubble events through Thompson scattering. This phenomenon closely resembles Coherent Elastic Neutrino-Nucleus Scattering (CEνNS), but it occurs with photons instead of neutrinos. This source of background introduces a substantial influx of additional events for several significant reasons:

1. The cross-section for photon scattering is considerably larger than what would be expected for neutrinos or WIMPs.
2. The detector's internal electronics have the potential to emit photons with energies reaching these levels.
3. The extent of this background is heavily contingent on the shielding design implemented for the detector.

Any inconsistencies with signal detection must lead to several additional techniques to be considered [18] .

3.3 The SBC Detector

The SBC collaboration is building its first detector officially called the SBC-LAr10. This project is currently in development and commissioned at Fermi National Accelerator Laboratory. As we have discussed, SBC's main purpose is to characterize new low-threshold opportunities of a liquid-argon bubble chamber for accurate identification of neutrinos and WIMPs [64]. This is sought to be achieved by validating and providing a full study of many backgrounds and calibration sources, many of which are discussed in this chapter and the next. The chamber is expected to deliver the following design specifications:

[4]By reference, the SBC detector is expected to have a 5 keV threshold
[5]Neutrons with energies around 0.025 eV's.

Design	Goals
Target Volume	10 Liters (10 kg liquid-argon at 130 K)
Target Fluid	Xenon-doped Argon with options for pure Ar, Xe, N_2, and CF_4
Super-heat capabilities	40 eV (liquid-argon at 1.4 bars, 130 K)
Thermodynamic Regulations	$\pm$ 0.5 K, $\pm$ 0.1 bar ($\pm$ 5 eV Seitz Threshold)
Scintillation	1 photon per 5 keV nucleus-recoils in Xe-doped Argon
Imaging	Bubble Image Capturing: Cameras running at 100 fps, mm-resolution with stereoscopic imaging
Acoustic Detection	$\pm$ 25 μs resolution for time-of-nucleation reconstruction
Zero-scintillation single bubble rate	1 background event per live year

Table 1: SBC-LAr10 design goals: Target Volume, Target Fluid, Super-heat capabilities, Thermodynamic Regulations, Scintillation, Imaging, Acoustic Detection and Zero-scintillation single bubble rate. Adapted from: [18].

These set goals would allow for the ability to measure low-energy nuclear recoils allowing the search for GeV-scale dark matter and the measurement of coherent elastic neutrino-nucleus scattering on argon from MeV-scale reactor anti-neutrinos. These goals are bounded by background suppression and calibration strategies. In the previous sub-section, we discussed the strategies for an almost background-free scheme, an overview of the calibration strategies shall be discussed in this chapter. Before this, we need to understand more detail the detector's design.

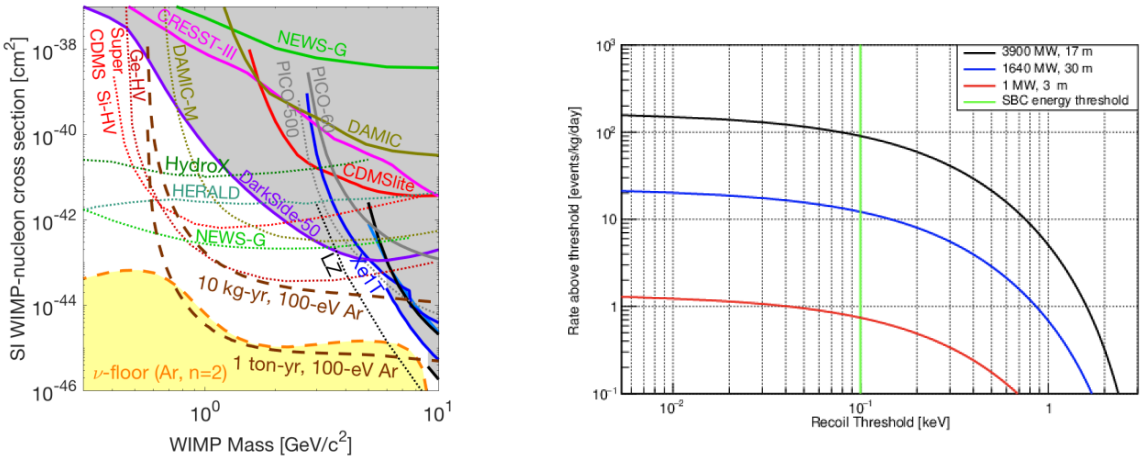

Figure 6: Physics Opportunities for SBC-LAr10. Right: Expected spin independent WIMP-nucleus cross-section bound for SBC given a one year exposure. Neutrino Energy Detection Rate for different reactors given SBC capabilities. Taken from: [17].

3.3.1 Design and Construction

Given the functioning conditions required for the SBC-LAr10 and in general, for any low-background particle detector, a shielding is required for operation. This protective layer should block out as many particles as possible from different sources that can induce a bubble-like event (cosmic rays, radioactive decay, etc.). The calibration setup will be deployed at Fermilab in the MINOS tunnel, which is located 100 meters underground. This allows to reduce the cosmic-ray induced muons rate by a significant amount, this will be sufficient for low-energy calibration without any additional shielding. Additionally, the SBC collaboration is currently analyzing further projects for similar detectors in different locations. These new detectors will implement design modifications based on the experience gained during the construction and commissioning of SBC-LAr10. SBC-SNOLAB is a proposed project, also desired for dark-matter detection, that will be located in the ladder labs at SNOLAB with water and copper shielding designed to attenuate rock-based neutrons and gamma rays respectively. Another SBC detector study has also been initiated to understand the feasibility of measuring anti-neutrino detection at the Laguna Verde nuclear power plant in Mexico [65]. For this project, we will focus only on the SBC-LAr10 in Fermilab.

Figure 7 shows the schematic of the SBC-LAr10 detector. This gives a preliminary design of the detector. We will review the most important components and elements of the design below.

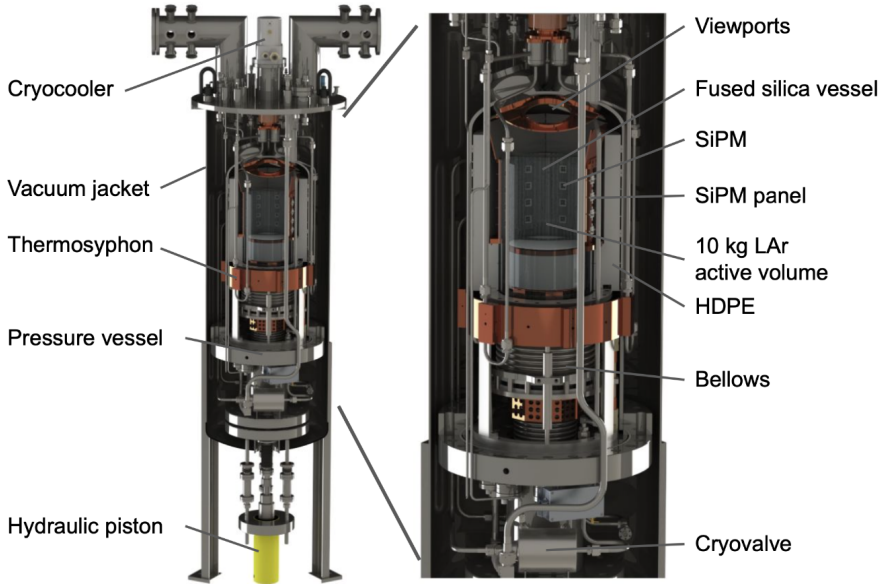

Figure 7: SBC-LAr10 Schematic. Left: Solid model base design with main components annotated. Right: Zoom-in vessel design with components. Taken from: [64].

Thermo-mechanical design. For the SBC-LAr10 to achieve a ± 5 eV Seitz threshold, the liquid-argon needs to be maintained in a super-heated state with a ± 0.5 K and ± 0.1 bar precision while expecting a nucleation event. When a bubble event occurs, the chamber needs to be re-compressed for a fraction of a second to bring the fluid back to a liquid state. For this to occur, a high-precision compression regulation system must be achieved, without generating nucleation in the surfaces of the liquid-argon. The tackled strategy is a buffer-free, dual-temperature-zone system. This is used by PICO-500 [40] and has also been successfully tested in SBC and other PICO test chambers [66, 63].

Pressure control To prevent surface nucleation, the super-heated fluid target is enclosed in a UV-transparent fused silica vessel with a smaller concentric vessel acting as a pressure control piston. Both vessels are sealed using spring-energized polytetrafluoroethylene (PTFE) seals and maintained at lower temperatures than the target fluid to keep it stable. A cryogenic hydraulic fluid, CF4 [67], is used to maintain pressure balance and is contained in a separate stainless steel vessel. Cryogenic valves isolate both the hydraulic and target fluids, creating a sealed environment. Pressure control is achieved through a bellows piston driven by a room-temperature hydraulic cylinder connected to a custom hydraulic system [64]. Figure 8 displays the completed hydraulic system and initial performance test results.

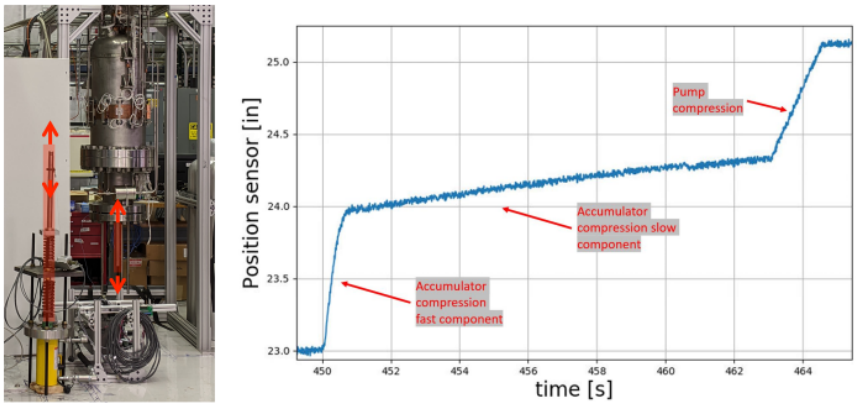

Figure 8: SBC-LAr10 Pressure System. Left: Main detector construction. Right: Piston Position vs. time for compression system. Taken from: [63].

Thermal Control To prevent bubble nucleation on stainless steel components and seals within the SBC-LAr10 pressure vessel, a dual-temperature system is implemented. The pressure vessel is cooled to a stable temperature (90 K for liquid-argon), while an isolated region around the target fluid is heated to a super-heated temperature (130 K for liquid-argon). This temperature gradient is maintained using a high-density polyethylene (HDPE) "castle" surrounding the target volume, which features vertical tubes with check valves to allow bi-directional fluid flow and prevent pressure buildup. Flexible plastic "wipers" further restrict convection. A nichrome wire heater heats the warm region. In the warm region, the CF4 liquid provides a convection thermal bath for the super-heated target, while in the cold region, CF4 is more viscous and insulating. Metal components in the inner assembly are thermally connected to the cold pressure vessel wall with spring-loaded copper fins. Liquid CF4 layers serve as thermal grease to enhance heat conduction. Heat is transferred from the pressure vessel wall to a copper band wrapped around the vessel's exterior, which is then cooled by closed-loop nitrogen thermosyphons. A 300-W Gifford-McMahon cryocooler finally dissipates the heat. The pressure vessel, thermosyphons [68], and cold head are insulated and enclosed in a vacuum jacket with feed-throughs for various systems. The estimated heat load on the pressure vessel is 220 W, with approximately half used to maintain the thermal gradient between the warm and cold regions.

Process Control The system described above includes approximately 125 "slow" instrumentation channels for monitoring parameters like pressure, temperature, and position, controlled by a Programmable Logic Controller (PLC) and a Python-based SCADA system. The

PLC manages control loops, interlocks, and automated procedures to regulate the chamber state, ensuring safe operation and precise control of various system components. Additionally, the PLC can store high-resolution instrument traces for detailed analysis, contributing to the data acquisition system's capabilities.

A more detailed analysis of all the controls can be found in [18] and [64].

3.3.2 Data Acquisition

Continuing with the design of the SBC-LAr10, scintillating bubble chambers have a range of data acquisition channels. This is mainly characterized by their time resolution, which turns critical for event reconstruction. From fast to slow, the four event signals come from: Scintillation ($\mathcal{O}(100)$ ns), Acoustic Signals ($\mathcal{O}(100)$ μs), Bubble Imaging ($\mathcal{O}(10)$ ms) and Pressure and Temperature histories ($\mathcal{O}(0.1$ - $1000)$ s). The latter is comprised in the Process Control description in the last subsection. Up next, we will briefly review the aforementioned channels. While quickly overlooking the reconstruction process.

Events We discussed in Section 2.1 what constitutes an event in a bubble chamber. The transition from a super-heated state to a pressurized can be activated by several trigger signals. This can be from either the imaging processing, a rise detection in the pressure, a random trigger by Run Control, etc. In all the presented cases, the information is intermediately broadcasted to all data acquisition systems allowing for offline synchronization for all possible channels.

The Run Control software initiates data acquisition in each data stream at the beginning of every event, ensuring complete data recording from each stream after the bubble chamber trigger, which marks the event's end. For instance, at the event's start, it instructs the PLC to record 10-ms resolution data for later retrieval. Once all data subsystems are prepared, Run Control initiates the pressure cycle through the PLC. When the bubble chamber is triggered, the PLC compresses the chamber, and Run Control stops acquisition while copying PLC data into the event record. Other data streams follow similar procedures.

Bubble imaging The SBC-LAr10 has three cameras continuously looking at the chamber. They provide both a trigger on nucleation and video recordings of the growing process of the bubbles in the liquid-argon. These cameras are Arducam OV028 1-megapixel shutter cameras, they are mounted in the vacuum space and are recorded through three separate sapphire windows on top of the pressure vessels. Raspberry Pi 4Bs (RPi's) located outside the vacuum jacket capture images from each camera at 100 frames per second and run a motion detection algorithm to generate triggers when necessary. When a bubble chamber trigger is received, the RPi captures post-trigger images. The cameras require a relay lens system to separate the sensor from the optics for cryogenic compatibility. Illumination for bubble images comes from three rings of 850-nm LEDs inside the pressure vessel, providing front-lit views of the inner assembly lined with PTFE. These LEDs are pulsed in sync with camera exposures, and a custom LED driver ensures stable illumination. Tests confirmed the system's functionality under the required conditions, but fluorescence in the cryogenic CF4 cell suggests the possibility of operating the imaging system with illumination only after a bubble chamber trigger to enhance scintillation detection while preserving post-trigger images for event reconstruction.

Scintillation Scintillation photons in the vacuum ultra-violet range are detected by silicon photomultipliers (SiPMs) placed just outside the target volume, submerged in the cryogenic hydraulic fluid. To efficiently collect these scintillation photons, the argon target is doped with xenon, shifting the scintillation wavelength to 175 nm, where both the fused silica and CF4 hydraulic fluid have long absorption lengths [69]. Reflective PTFE covers all surfaces visible to the target volume except for the SiPMs, camera viewports, and the annular region between vessels, resulting in an estimated light collection efficiency of approximately 10%. SBC-LAr10 at Fermilab uses Hamamatsu VUV4 SiPMs, powered by custom bias boards and connected to a CAEN multichannel digitizer for signal amplification and waveform recording. The CAEN triggers on any input channel exceeding a set threshold and timestamps the triggers, allowing synchronization with other data streams. Additionally, some SiPMs are positioned to collect scintillation from liquid CF4, serving as a veto for external backgrounds, marking the first use of scintillation from liquid CF4, with ongoing research in this area.

Acoustic Detection In previous low-background bubble chambers, analyzing acoustic data from each event was crucial for distinguishing events caused by nuclear recoils from those caused by alphas [70]. However, with the introduction of scintillation data, the role of acoustic data has shifted primarily to determining the precise timing of bubble nucleation, achieving an accuracy of 25 microseconds in xenon prototypes [61]. The shockwave generated by the growing bubble and subsequent high-frequency ringing of the detector is detected by textured lead zirconate titanate (PZT) piezoelectric elements mounted in the HDPE castle, which are spring-loaded against the outer fused silica vessel. These signals are then pre-amplified (with both cold and warm preamp options available) and digitized for a window extending approximately 100 milliseconds before and after the bubble chamber trigger. Further details on these sensors can be found in [55].

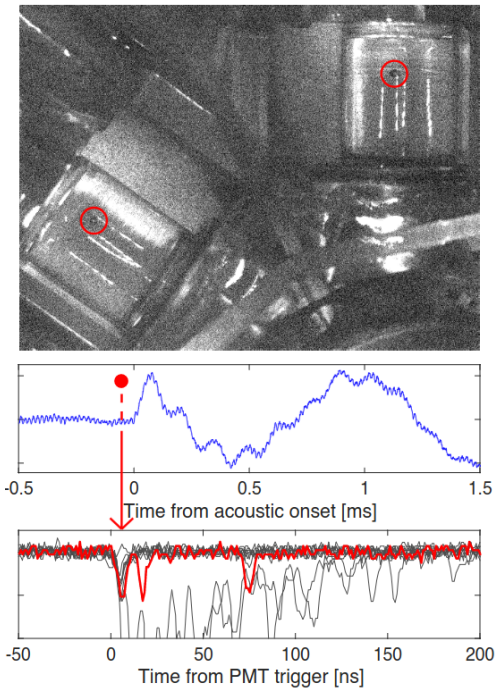

Figure 9: Example of a nuclear recoil event captured in the prototype xenon bubble chamber. Taken from: [61].

In Figure 9, the upper section presents a stereo image pinpointing a distinct xenon vapor bubble outlined in red. Moving to the middle plot, it illustrates the acoustic data capturing the actual formation of the bubble. Below, the plot showcases waveforms from photomultiplier tubes (PMTs) indicating xenon scintillation. The identifiable red pulse corresponds to the event coinciding with the bubble formation, while the surrounding gray traces signify scintillation pulses generated by electron recoils occurring within the same timeframe as the bubble's formation but without concurrent nucleation

Data Analysis Utilizing the four mentioned data acquisition channels, the analysis involves multiple modules that process raw data to reconstruct events. These modules include quality checks for pressure and temperature control, bubble identification in camera images, 3D bubble position reconstruction, acoustic nucleation time determination, and identification of scintillation signals, whether coinciding with bubbles or not. The 2D positions of bubbles in images are found by detecting pixel clusters with significant frame-to-frame variation [55]. Combining data from multiple images yields the 3D bubble position and a goodness-of-fit measure. Acoustic sensor signals are analyzed to pinpoint when the bubble shockwave reaches each sensor, and position-dependent delays are calibrated for precise nucleation time. Coincident scintillation signals are identified, with events associated with expected scintillation being tagged. Dark matter candidates, expected to have no scintillation, are rejected if coincident with any scintillation signal.

3.4 Calibration Strategy

After discussing the technical design and data acquisition process of the SBC-LAr10, the next step is to utilize the characteristics of the detector to employ calibration techniques. The main purpose is to determine events that are responsible for background noise, by this, we mean to understand the noise rejection as a function of the nuclear recoil bubble energy threshold. To characterize this function, a detailed analysis of the response of the detector to several background sources must be understood. In this sub-section, we will talk about the required strategies for event identification.

3.4.1 Electron Recoil Discrimination

The calibration strategy for electron background stems from observing electron-induced nucleation in the detector. The rate of electron-induced nucleation events will be used to characterize the thermodynamic properties (pressure and temperature) of the detector. As we previously mentioned, the desired nucleation events should be nearly zero, a strong gamma source will be used to calibrate this property. Additionally, to understand the detector response, another gamma source will be used for the identification of liquid-argon and CF4 scintillation. The light yields are not a significant factor in the calibration of nuclear recoils at sub-keV scales, as most recoils at these energies do not produce detectable scintillation light. However, they hold great importance in the context of characterizing and managing background signals for future rare event searches[6].

[6]Important to notice the following, while electron recoil-induced nucleation events are extremely rare, electron recoils do occur at a noticeable rate. This means that electron recoils can produce scintillation. The use of scintillation as a data acquisition channel becomes extremely useful to identify and discriminate between an electron-recoil scintillation and a nucleus-recoil scintillation.

3.4.2 Nucleus Recoil Sensitivity

For nuclear recoil calibration, the task becomes more challenging. This is because the interested nucleus recoil energies for a proposed $\approx$ 1 GeV WIMP are in the region of 100 eV to 1 keV, this is below the nucleus recoil-induced scintillation threshold of around 5 keV. Thus, the chamber essentially works as a threshold detector, where nucleation needs to be characterized by the nucleus-recoil energy spectrum. For an effective nucleus-recoil calibration, a neutral particle at low energies can probe the detector response at the desired near-threshold nucleation energy. Given the characteristic of the dark matter mass and the absence of charge, the neutron becomes the best candidate for a low-energy calibrator for the detector response. Other methods for low-energy nucleus interactions calibration given the characteristics are photon-nucleus scattering and thermal neutron captures. We will discuss the three up next.

Photo-Nucleus Scattering This technique capitalizes on the bubble chamber's insensitivity to electron recoils. It involves observing photon-nucleus Thomson scattering caused by high-energy gamma rays. For instance, the 2.6 MeV gamma emitted by ^{208}Tl (a decay product of ^{228}Th) can generate argon recoils with energies of up to 370 eV. These gamma sources do not produce multi-bubble events but instead yield much more distinct and sharp low-energy spectral features [71].

Thermal Neutron Capture A thermal neutron capture[7] in ^{40}Ar allows for a characterized gamma spectrum with a maximum in 4.7 MeV. The resulting ^{41}Ar recoil energy spectrum peaks at 320 eV [72]. This process can be used for ultra-low energy calibration techniques, however with low detection efficiency. ^{36}Ar is also prone to thermal neutron capture, producing a nearly mono-energetic 1.1 keV ^{37}Ar recoil [73]. The neutron capture events can be identified via scintillation signals.

Low-energy Neutrons The previous methods of calibration bring strategies up to a few hundred eV's. However, they pose difficulty in efficiency. A controlled method of neutron radiation with known energies can probe nuclear recoils at energies around 1 keV. The process for producing mono-energetic low-energy neutrons will be discussed in the next section. The specifics lie in analyzing photonuclear reactions. This calibration technique is the main focus of this work [20].

Preliminary analysis for these three low-energy scale threshold calibration techniques has been studied before. Results for the SBC-LAr10 can be found in [18]. Figure 10 shows plots for simulated events.

[7] A Thermal Neutron Capture is a $N(A,N)+n \rightarrow N(A+1,Z)+\gamma$ nuclear reaction.

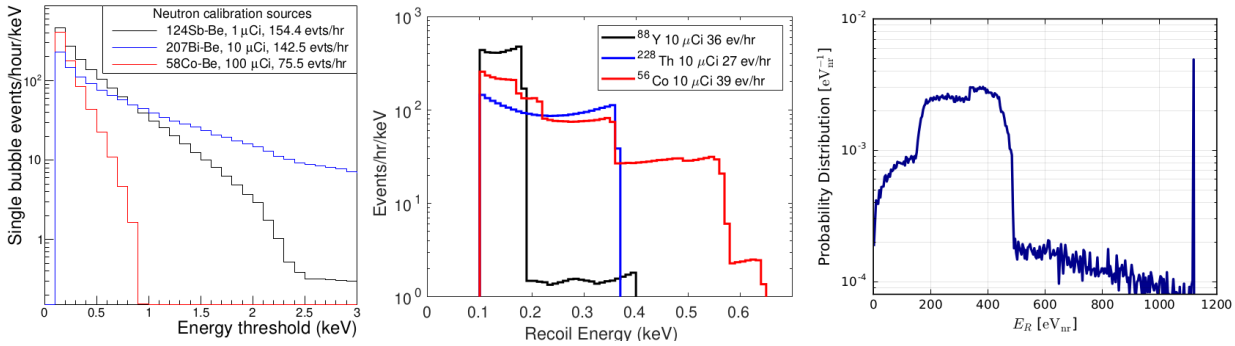

Figure 10: Simulated nucleus energy recoil spectrum in the SBC-LAr10 for different calibration techniques. Left: Photo-neutron nucleus scattering. Center: Photon-nucleus scattering. Right: Argon-40 neutron capture. Taken from [18] and [74].

SBC-LAr10 may encounter challenges in achieving the desired ER discrimination at low thresholds initially. In such a scenario, there are four potential approaches for enhancing low-threshold discrimination using the existing SBC-LAr10 hardware: 1.-Reduced Xenon Doping: Operating without or with reduced xenon doping can eliminate potential Auger-cascade backgrounds [75]. 2.- Pure Liquid Xenon (LXe): Shifting to pure LXe operation may reduce prompt local heating associated with dimer formation along the electron track. 3.- Applied Electric Field: Implementing an applied electric field of around O(100) V/cm could diminish heating linked to electron-ion recombination. 4.- Reduced Pressure and Temperature: Operating at reduced pressure and temperature, as demonstrated in previous research, can potentially decrease electron recoil sensitivity while maintaining a constant Seitz threshold.

If SBC-LAr10 achieves low-threshold capabilities right from the start, the focus will shift to extensive calibrations aiming for a 5% threshold uncertainty, a requirement for precise CEνNS detection [16]. Achieving this level of precision calibration will involve using photon-nucleus scattering with recoil characteristics closely matching the operational threshold.

With the design, construction, operation, and calibration strategies discussed, as mentioned previously, we will start to focus on the low-energy neutron-nucleus scattering process as a means of calibration. Keeping in mind the detector's abilities and restrictions, we will go in-depth about the available neutron sources to achieve this calibration.

4 Photo-Nuclear Reactions for Nucleus Recoil Calibration

Neutron radiation can be a source of background and a calibration signal produced by the SBC-LAr10 detector. Nucleus recoils produced in the liquid-argon by the interaction with low-energy neutrons can probe the detector nucleation thresholds, as well, given the neutron mass and expected nucleus recoil, closely resemble and mimic a WIMP signal [20]. Neutrons, however, can be difficult to produce in a controlled environment. This issue comes from the fact that most neutron sources produce a continuous energy spectrum, to fully isolate a signal with significant statistics, the neutron energy needs to be known. In this chapter, we will discuss all the available neutron sources and specifically focus on the ^{9}Be(γ,n)^{8}Be photonuclear reaction, which produces nearly mono-energetic neutrons. A detailed analysis of this process is required to understand its experimental and numerical implications.

4.1 Neutron sources

Isotopes that emit neutrons are extremely impractical for use in the lab. While artificially produced isotopes that emit neutrons exist, they are highly unstable and difficult to produce. Neutron sources for experimental applications need to be carefully studied as the energy and angular distributions need to be fully understood. The more reliant and common sources of controlled-laboratory neutrons are spontaneous fission and nuclear reactions. In the following two sub-sections, we will discuss these processes.

4.1.1 Spontaneous Fission

This process occurs in many trans-uranium elements which release neutrons and fission fragments. The most common isotope for this source is ^{252}Cf, the energy spectrum of the released neutrons is a continuous Maxwellian shape plot that extends up to 10 MeV. While this method of neutron production is effective, the energy range of the emitted neutrons is extensive, thus, for high-precision measurements they tend to be quite ineffective [76].

4.1.2 Nuclear Reactions

The method of producing neutrons via nuclear reactions is much more convenient, many nuclei have the property of producing neutrons via (α, n) or (γ, n) reactions in various ranges of energies. These sources are usually made up by a target material being enveloped in a suitable alpha or photon emitter. The most common target materials are light nuclei with low binding energy, like beryllium-9. Alpha particles interacting with beryllium undergo several reactions, many of which produce neutrons [77]. It is important to notice that depending on the inciting alpha particle energies, the cross-section for all the reaction modes (channels) change, and some reactions become more prevalent at different energy scales. The rates at which neutrons are being produced depend on the reaction cross-section and the activity of the alpha emitter. This method of producing neutrons, while more controlled, pertains to the same energy spectrum problem as the spontaneous fission sources, they are highly unpractical for experiments where the neutron energy needs to be fixed. However, many nuclear reactions have the ability to produce nearly mono-energetic neutrons at some low-energy scales.

4.2 Mono-energetic neutron sources

The previously mentioned sources, while effective in producing neutrons at good rates, lack the ability to have a definite energy. Up next we will continue the discussion on nuclear reactions, focusing on mono-energetic processes. Let us first discuss the usefulness and the reason why we need mono-energetic neutrons.

When measuring nuclear recoils, a spectrum of the transferred energy from the neutron to the nucleus is expected. The maximum amount of energy transferred can be calculated via kinematics and is:

$$E_r^{\max} = \frac{4m_n m_X}{(m_n + m_X)^2} E_n, \tag{4.1}$$

where $E_r^{\max}$ is the maximum possible recoil energy of the nucleus, m_n is the mass of the neutron, m_X the mass of the nucleus and E_n the energy of the neutron. Low mono-energetic neutrons, i.e. when E_n is fixed and produces a small energy spectrum, are extremely useful to produce nuclear recoils. Up next we will review the most common reaction.

4.2.1 AlphaNuclear sources

For alpha particles at a set energy, the emitted neutron energy spectrum shows theoretically mono-energetic lines, corresponding to all the different transitions and modes available. However, for mixed sources, which is how usually these sources are built, there is smearing on the alpha's energy spectrum, consequently also producing a smear in the neutron spectrum. There is also a considerable Doppler broadening that amounts to up to 2 MeV of noise [78]. Additionally, $X + \alpha$ reactions tend to have multiple modes of reaction, that as previously mentioned, depend on the energy of the alpha particle. One must be careful in choosing the correct target and source to produce mono-energetic neutrons via alpha's. In this work, we will not focus on this method.

4.2.2 PhotoNuclear sources

For photonuclear reactions (γ, n), the two most suitable target materials for low mono-energetic neutron production are:

$$\begin{aligned} {}^{9}\mathrm{Be} + \gamma &\rightarrow {}^{8}\mathrm{Be} + n, \\ {}^{2}\mathrm{H} + \gamma &\rightarrow {}^{1}\mathrm{H} + n. \end{aligned} \tag{4.2}$$

These targets are the most convenient because of their small binding energy of the neutrons in the nucleus (1.687 MeV for ^{9}Be and 2.23 for ^{2}H). For a photonuclear reaction to occur, the energy of the incident photon in the target must have at least the same energy as the binding energy of the neutron. The major advantage is that, at energies close to this Q value, the neutrons are emitted mono-energetically. This happens since photons are not slowed down as easily as alphas, the reaction is completely inelastic, and most importantly: the energy transfer range is low. Theoretically, via kinematics, these neutrons are not exactly mono-energetic, but the spread is extremely low. Given an inverse two-body decay, we can calculate an approximate energy relation for the maximum neutron energy (in the case where the nucleus does not acquire kinetic energy) $\gamma + A(Z, N) \rightarrow N + A(Z, N-1)$ to be

$$E_n^{max} \approx \frac{N-1}{N}(E_\gamma - Q), \tag{4.3}$$

where N is the number of nucleons, E_γ the photon's energy and Q the binding energy of a neutron. Analyzing the previous equation, a cut-off appears when $E_\gamma = Q$[1]. Since (eq above) is only the value of the maximum energy, one could expect an energy spectrum from E_γ to Q. However, if the energy E_γ is close to Q by a δE, one could theoretically expect a near Dirac delta function for the energy of the neutron. With this, an interesting play of variables starts to occur, since at low energies, the rate of production is extremely low, up to two orders of magnitude less compared to an alpha-nuclear source, but at higher energies (>10 MeV), not only does the mono-energetic spectrum starts to smear, but also more decay channels with higher cross-sections start to appear, one must carefully select the correct gamma energy so it does not bring either other channels into play or produce a large continuous energy spectrum.

Equation 4.3, while useful as an approximation for understanding the maximum energy, it lacks the ability to predict the small, yet important, energy spectrum. A full classical relativistic correction and full kinematic derivation for this process can be found in [79], where it shows that the emitted neutron energy follows the next formula:

$$\begin{aligned} E_n = & \frac{N-1}{N}(E_\gamma - Q) \\ & + \frac{E_\gamma^2}{Nmc^2}\left[\left(\frac{\cos^2\theta}{N} - \frac{1}{2}\right) + \cos\theta\sqrt{\left(\frac{\cos^2\theta}{N^2} - \frac{1}{N}\right) + \frac{N-1}{N}2mc^2\left(\frac{E_\gamma - Q}{E_\gamma^2}\right)}\right] \end{aligned} \tag{4.4}$$

where mc^2 is the rest mass of the neutron, θ the angle in which the neutron is emitted with respect to the photon, N the number of nucleons in the target, E_γ the photon energy, and Q the reaction threshold energy (binding energy). It is extremely important to note that in this equation, the energy is dependent on the angle of emission, this will become important for numerical implementation and analysis. Using this relationship, we can also find the maximum and minimum values of the neutron energy, which are when $\theta = 0$, or when $\cos\theta = \pm 1$.

$$\begin{aligned} E_n^{\max} &= \frac{N-1}{N}\Delta E + \frac{E_\gamma^2}{Nmc^2}\left(\frac{2-N}{2N} + \sqrt{\frac{N-1}{N}\left(2mc^2\frac{\Delta E}{E_\gamma^2} - \frac{1}{N}\right)}\right) \\ E_n^{\min} &= \frac{N-1}{N}\Delta E - \frac{E_\gamma^2}{Nmc^2}\left(\frac{N+2}{2N} + \sqrt{\frac{N-1}{N}\left(2mc^2\frac{\Delta E}{E_\gamma^2} - \frac{N-3}{N(N-1)}\right)}\right) \end{aligned} \tag{4.5}$$

where $\Delta E = E_\gamma - Q$. We can observe that, the maximum energy differs from the one found in equation 4.3 by a factor $\propto E_\gamma^2$. This is important to notice since the maximum nucleus recoil energy will be proportional to this. Additionally, we can also find the lowest nucleus recoil energy expected from this scattering, however, as we will mention in further analysis, this will not always be the case.

This equation will become useful for a numerical implementation and analysis in the next chapter.

For future reference and consideration, we will take a special interest and fully detailed analysis of the $^9\mathrm{Be}(\gamma, n)^8\mathrm{Be}$ reaction, as this is the neutron source that is being used for the SBC calibration program.

[1] Under the approximation where the mass of the proton is the same as the mass of the neutron

4.3 The ^{9}Be$(\gamma, n)^{8}$Be reaction

Out of the two suitable photonuclear reactions discussed, beryllium-9 is the preferred target due to its low binding energy, pure abundance, and stability. As the selected process for the production of neutrons, a full detailed analysis of the reaction is discussed in this subsection, with the intent to implement it for nucleus recoils in liquid-argon.

4.3.1 Cross-section

Since the 1930s, the ^{9}Be$(\gamma, n)^{8}$Be process has been subject to testing, yielding conflicting results [80, 81, 82]. The primary objective of this studies has been to comprehend how the cross-section varies in relation to photon energy. For this purpose, a source of mono-energetic photons with well-documented production rates, intensities, and detection efficiencies is required. Several methods are available to measure the cross-section under these specific conditions. One approach involves the generation of photons through bremsstrahlung emission from decelerated electrons [83], although this method carries inherent uncertainties due to the wide range of photon energies produced. Alternatively, inverse Compton scattering offers a more controlled environment for mono-energetic photon production, albeit with limited available data for this particular process. The simplest and most effective method is through the emission of photons by radioisotopes. Historical experimental data from the latter half of the 20th century often employed this approach, although many of the results lack high precision. In a notable effort, Robinson. A, as detailed in [84], compiled early cross-section measurements and implemented corrections to construct the most accurate possible compilation of the cross-section data for this process. Figure 11 illustrates this compiled work.

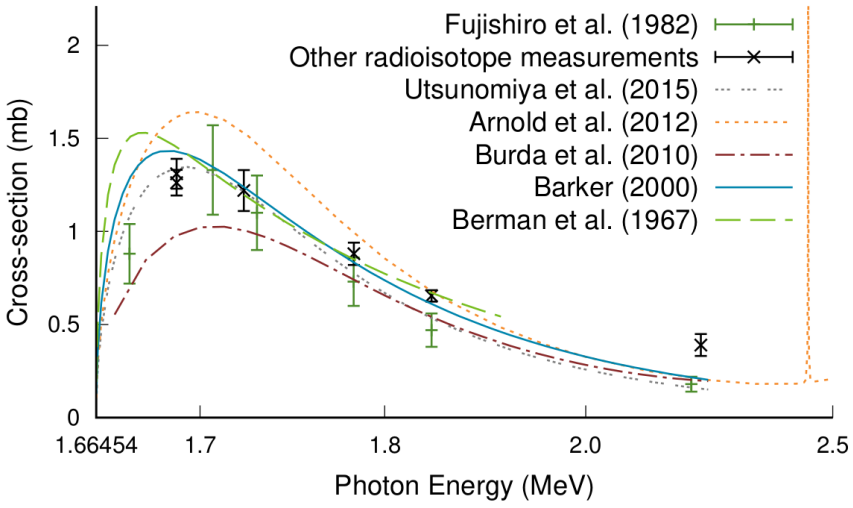

Figure 11: Corrected cross-section for the ^{9}Be$(\gamma, n)^{8}$Be reaction as a function of the photon energy. Taken from: [84].

As expected, a cutoff occurs at 1.66454 MeV, the Q value of the reaction (energy threshold). A small resonance follows up after this limit.

Up to this point, our sole focus has been on the (γ,n) channel, as previously discussed.

However, it's essential to note that, depending on the energy scale involved, various other reactions come into play. A comprehensive summary of all potential interactions and their respective energy thresholds can be found in Table 2, as documented by [19].

Reaction	Threshold Energy (MeV)
(γ,n)	1.67
(γ, n+2α)	1.67
(γ, p)	16.89
(γ,t)	17.69
(γ, ^{3}He)	21.18
(γ, 2n)	20.56
(γ, np)	18.92
(γ, 2p)	29.34
(γ, 3n)	31.34

Table 2: Different reactions for ^{9}Be + γ and the respective energy threshold for each process. Adapted from: [19].

To generate a quasi-mono-energetic energy spectrum from the emitted neutrons, it is crucial to focus on photon energies below 15 MeV. When conducting neutron-nucleus calibration, as emphasized in [20], it is imperative to keep the neutron energy as low as feasibly possible. This aligns with the principles outlined in the previous sub-section, where the photon energy should closely approach the threshold energy Q.

4.3.2 Suitable Isotopes

As previously highlighted, the energy of photonuclear neutrons is dependent on the energy of the incident photons. Therefore, a critical factor in generating mono-energetic neutrons is the availability of a source of mono-energetic photons closely matching the energy value Q. Thankfully, there are numerous methods for producing photons with fixed energies. As discussed in Section 4.2.2, one of the most efficient methods involves the utilization of radioactive gamma decay from various isotopes. However, when selecting the appropriate radioisotope, several considerations come into play. The chosen isotope should ideally emit photons with energy values near Q and possess a high branching ratio (BR) at this specific energy emission. Branching ratios with energy values below Q or below 0.01% are generally not taken into account, while also bearing in mind considerations of efficiency and availability.

Robinson A., in [85], compiled the most suitable radioisotopes for this reaction, a table (Table 3) with the most relevant information about the isotopes, including the neutron energy range calculated from equations 4.5, is followed.

Isotope	$t_{1/2}$	E_γ (keV)	BR(%)	E_n (keV)
^{28}Al	2.245(2) min	1778.99	0.399(12)	98.59 - 104.49
^{38}Cl	37.230(14) min	2167.40	44.4(9)	439.22 - 454.19
^{58}Co	70.86(6) d	1674.73	0.517(10)	8.04 - 9.73
^{72}Ga	14.10(1) h	1862.00	5.410(18)	171.27 - 179.35
^{88}Y	106.627(21) d	1836.06	99.2(3)	148.54 - 155.98
		2734.0	0.71(7)	936.42 - 963.95
		3219.7	0.007(20)	1362.21 - 1401.29
^{105}Ru	4.44(2) h	1698.17	0.0766(9)	28.18 - 31.26
		1721.15	0.0299(3)	48.13 - 52.16
^{124}Sb	60.20(3) d	1690.97	47.57(18)	21.96 - 24.68
		2090.93	5.49(3)	372.10 - 385.41
^{206}Bi	6.243(3) d	1718.7	31.9(5)	45.10 - 49.93
		1878.65	2.01(4)	185.86 - 194.35
^{207}Bi	31.55(4) yr	1770.23	6.87(3)	90.94 - 96.58
^{226}Ra	1600(7) yr	1729.60	2.878(8)	55.48 - 59.82
		1764.49	15.30(3)	85.92 - 91.39
		1847.43	2.025(9)	158.50 - 166.22
		2204.06	4.924(18)	471.40 - 487.17

Table 3: Suitable radioisotopes for near mono-energetic photo-neutrons.

Out of the suitable candidates, the most convenient radioisotopes, due to natural abundance, commercial availability, branching ratios, energies, and cross-section are ^{58}Co, ^{124}Sb, and ^{207}Bi. ^{88}Y has a really good BR close to Q, but the other BRs smear the neutron energy spectrum, many experiments have used this source for calibration [20], but for the purpose of this study, we will set it aside. ^{226}Ra has the same problem but also with a large half-life time. The issues remain similar among all the remaining radioisotopes. We also report the expected energy of the neutron due to each isotope, the range goes from the minimum energy and the maximum calculated with the formulas found in section 4.2.2.

4.3.3 Neutron Yield, Rates and Expected Recoil Energy

Given the chosen radioisotopes, it is important to analyze the expected neutron rate, yield, and cross-section. In order to find these properties, an analysis of the photonuclear cross-section at said radioisotope photon energy must be performed. Looking at Figure 11, we find the cross-section of the interaction at said radioisotope photon energy, multiplying by the

BR, we can find the yield of said reaction. Given the specific activity of the radioisotope, one can find the neutron production rate. Since the SBC detector will have a small radioisotope source inside the ^{9}Be calibration tube, we can use the yield, number of atoms, and half-life time to calculate an approximate neutron production rate per gram. While this analysis is useful for a theoretical calculation of the photon flux, for practical purposes, it's not. In the next section, we will discuss the reason for this. However, for now, we will describe the characteristics of the radioisotope sources.

Its important to denote the maximum elastic nucleus recoil energy for every source, utilizing equations 4.1 and 4.3 we find that the energy will be proportional to the number of nucleons in the target and the photon energy. For a $X(A, N)$ nucleus, the maximum recoil energy by a neutron produced via a X'/^{9}Be source is

$$E_r^{\max} \approx \frac{4N}{(N+1)^2} E_n^{\max} \tag{4.6}$$

where $E_r^{\max}$ is the maximum recoil energy in the nucleus, N is the number of nucleons in the nucleus[2,3] and $E_n^{\max}$ the maximum neutron energy (reported in Table 3 and calculated with equation 4.5) [4].

Source	Yield (BR $\times$ σ) (mb)	Specific Activity (Bq/g)	Neutron Rate (Bq/cm*g)	E_r^{max} (keV) (LAr)
^{58}Co/^{9}Be	0.0058	5.1959×10^{14}	373.04×10^{6}	0.92
^{124}Sb/^{9}Be *low*	0.6720	2.8111×10^{14}	23.383×10^{9}	2.34
^{124}Sb/^{9}Be *high*	0.0145	2.8111×10^{14}	504.56×10^{6}	36.68
^{207}Bi/^{9}Be	0.0660	8.7974×10^{11}	7.1873×10^{6}	9.19

Table 4: Photo-Neutron information of ^{58}Co/^{9}Be, ^{124}Sb/^{9}Be and ^{207}Bi/^{9}Be sources.

We have denoted ^{124}Sb/^{9}Be *high / low* to make the distinction between the two, close to Q energies, BR's. They produce two very different rates and recoils, so given the detector's resolution, it should be able to identify two different responses. The neutron detection rate will dependent on the detector's calibration chamber geometry. Its important to highly again that the neutron production rate in Table 4 should only be taken as an approximate of the neutron rate capabilities. As we can observe, these rates are extremely high, a feature that will pose a significant problem due to the detector response time. A discussion about this issue is reviewed in the next chapter and Appendix C. Additionally, Appendix A has a discussion of the calculations required for the reported table.

It is also important to keep in mind that equation 4.6, just like equation 4.3, is an approximation of a non-relativistic neutron-nucleus scattering. Thus a full correction would be

[2]Note that this N is different than the one introduced in equation 4.3

[3]Given the SBC configuration, we will start to use N =40, as this corresponds to liquid-argon nucleons.

[4]This under the approximation of proton mass being equal to neutron mass

performed as well, however, due to the nature of the low-energy scattering, these corrections are not meaningful for analysis. Instead, we are only performing a calculation of an approximate expected maximum nucleus recoil. Simulations and calibrations under this paradigm should reach a maximum of around the reported energy.

4.3.4 Angular Distribution

An important feature to consider is the angular cross-section, specifically considering the geometry efficiency of the detector. Even more than for the photon energy-dependent cross-section, a huge uncertainty is apparent in both models and experimental data. Models like proposed in [19] incite an elegant yet complex angular distribution, that unfortunately, for the purpose of this work, are out of scope for the implementation. Guth, Mullin, and Czyz [86, 87] calculated a theoretical angular distribution assuming that the ^{9}Be consisted of a ^{8}Be nucleus plus a valance neutron. This approximation led them to find a distribution by the form $a + b\sin^2\theta$. Under this assumption, authors Fabricand, Allison and Halpern [88] measured the angular distribution for the ^{12}C(γ,n)^{11}C and ^{9}Be(γ,n)^{8}Be photoneutron reactions. By using photons from bremsstrahlung of a maximum energy of 15 MeV, they found an approximate angular distribution.

$$\frac{d\sigma}{d\Omega} = (1.26 \pm 0.11) + \sin^2\theta \tag{4.7}$$

A detailed experimental setup for this result can be found in [88]. For future references, this angular distribution will be used for calculations[5].

This distribution is extremely relevant for the energy of the emitted neutrons. We have calculated the expected, small, energy spectrum of the selected radio-isotopes to perform calibrations, this with the full neutron energy spectrum formula detailed in equation 4.4. This describes all the possible energies the neutron can be emitted as a function of the angle of emission with respect to the incoming photon. This analysis will performed in the next section when exploring the numerical implications of the characteristics of the photonuclear reaction presented in this section.

[5] An exact $d^2\sigma/d\Omega dE_\gamma$ should be considered, however, due to experimental and model uncertainties, we will use equation 4.7 as an approximation given that we are working in a low-energy <15 MeV range.

5 GEANT4 simulations for the Photo-Nuclear Calibration of the SBC

GEANT4 is a MonteCarlo based tool-kit designed to simulate how particles traverse material media. In the field of particle physics, GEANT4's significance lies in its ability to emulate the complex experimental conditions and processes that occur within particle detectors and accelerators [89]. The SBC collaboration, in particular the IF-UNAM group, has designed and tested the detector's geometry and functioning in GEANT4 version 10.03. The SBC GEANT4 project tries to replicate and mimic the expected live conditions and measurements of the SBC-LAr10. A snapshot of the SBC-LAr10 design in GEANT4's visual program can be observed in Figure 12 .

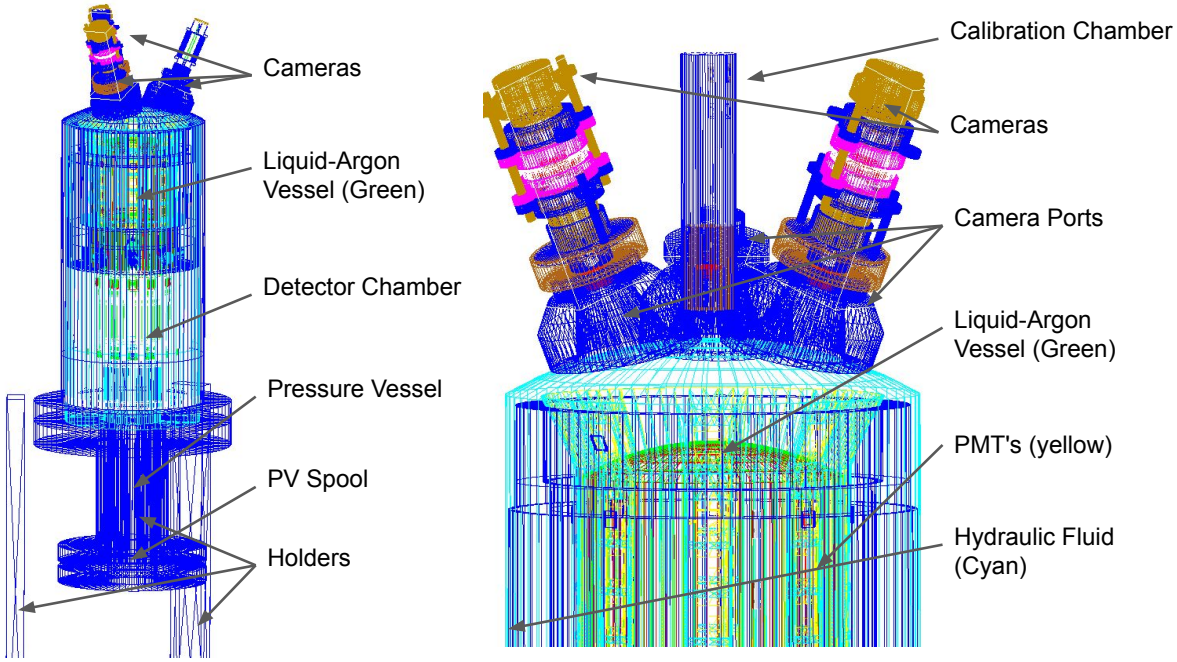

Figure 12: SBC-LAr10 GEANT4's Construction without the Vacuum Vessel. Left: Full detector geometry of the detector. Right: Zoom in into the top of the detector. Calibration Tube (middle one), Three Cameras Systems (Pink with Brown), Top of the Pressure System (Green) and Photo-multipliers (Yellow).

Simulations for different processes within GEANT4 would bring important information for the expected detection rates, threshold limits, unknown interactions, and more. For this, we need to delimit the expected physics processes. The SBC GEANT4 runs with a specific list of physics process libraries. This libraries are bounded by models and experimental data. A library can contain fundamental processes like, for example, the photo-electric effect, to more complicated ones, like hadronic capture reactions. A detailed analysis of the physics lists can be found in the DMXPhysicsList.cc source file within the SBC GEANT4 project. This discussion will become keen in further analysis.

Continuing with the line of work for photonuclear calibration, we would like to discuss the experimental efforts and design for the calibration scheme of the detector. In Chapter 3

we reviewed and discussed the technical aspects of the SBC-LAr10, due to the scope of the project and this work, it is impossible to mention the full design abilities and construction procedures. For the context of this work, we would like to add the following design description to the detector construction design overview. The SBC-LAr10 has a calibration chamber, this, is referred to in the right model in Figure 12. Using the GEANT4 schematic visual aid, we can zoom in and analyze what this is.

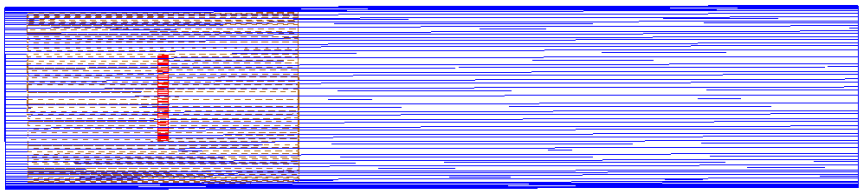

Figure 13: Zoom into the calibration chamber of the SBC-LAr10. Detector located at the right end.

This calibration chamber is a steel tube with a diameter of 5.08 cm and length of 24 cm situated at the top of the detector, this is shown as the blue geometry in the figure above. Inside this tube lies a small beryllium-9 block of 4.76 cm in diameter and a height of 7.62 cm, this is located almost at the end front of the steal chamber. Within the beryllium-9 block, a small disk-like radioisotope source can be found. While officially, the dimensions of this are not known, a considerate estimate of a radioisotope disk of 2.38 cm in diameter with a height of 0.3 cm is implemented. The beryllium and the radioisotope source are simulated by the geometry corresponding to the orange and red blocks respectively. These geometry specifications, while not yet installed, should match the expected dimension of the GEANT4 project.

Analyzing the physics opportunities, this calibration chamber matches exactly the method discussed in the previous section for neutron production. Hence, when substituting the radioisotope source with any of the ^{58}Co, ^{124}Sb, and ^{207}Bi, should begin to generate low-energy neutrons. GEANT4's simulation of this process will bring important information for the detector's geometry efficiency, nucleation rates, threshold energies, and more. In order to achieve this, a large number of events must be simulated to obtain sufficient statistics to perform analysis.

For this work, we will present two different procedures to simulate the photonuclear reaction for the calibration of the detector.

1. **Photo-Nuclear Library**: Utilizing GEANT4's own libraries.
2. **Neutron Particle Generator**: Simulate neutrons with the correct corresponding qualities.

During the next sub-sections, we will discuss the implementation of each of these approaches and report the results given by each.

5.1 Photo-Nuclear Library Approach

GEANT4 has an implemented physics library called G4PhotoNuclear, which is responsible for the interactions between photons and nucleus. For its functioning, it implements both a high-energy and low-energy model. These models depend on a variety of parameters, but since we are working at low neutron energy emission, we should focus on that. Unfortunately, GEANT4 does not have a great track record when it comes to low-energy interactions. Usually, at this energy scale, cross-sections and reactions tend to fail to be produced. For version 10.03 of GEANT4, this is the case for low-energy photonuclear reactions. We shall test and hope to fix this library in order to obtain the necessary results.

5.1.1 Vanilla G4PhotoNuclear Library

To test the SBC GEANT4 project in version 10.03 for photonuclear processes, first, we need to understand how the library is functioning. For this, we must first enable the *Shielding* physics lists. This is a built-in selected physics process produced by GEANT4. This list contains almost all particle-matter interactions and thus, includes all the models and requirements for a photonuclear interaction.

After performing this, simulations in the SBC geometry were performed with null results, by this we mean that no neutrons were generated, and hence, no neutron-nucleus interactions were recorded. To understand this, an analysis of this reaction was performed using this version of GEANT4. For this, a large beryllium block[1] was built in GEANT4 in order to enhance as much as possible the cross-section, inside this block multiple photons at different energies where simulated and the results were the following.

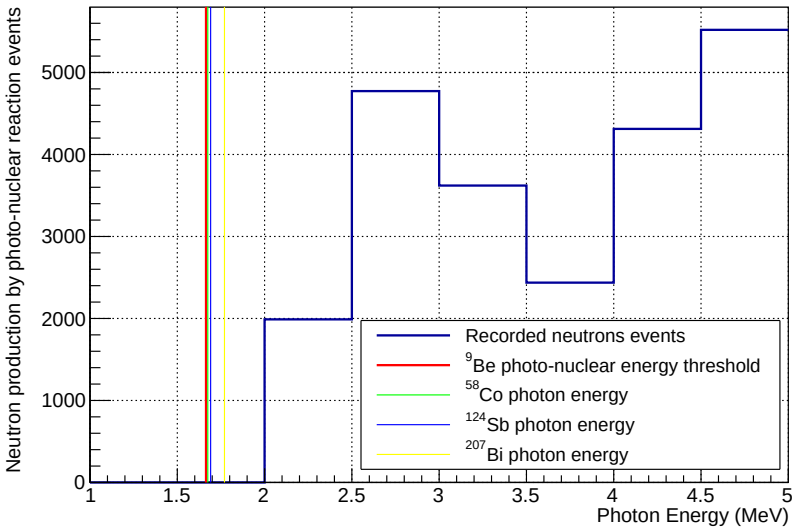

Figure 14: Neutrons produced by the photonuclear reaction in Beryllium-9 for different energies for 10^8 simulated photons using the vanilla GEANT4 PhotoNuclear Library. For reference, lines for the reaction energy threshold and radioisotope energy sources are plotted.

[1]Since we are only analyzing the reaction thresholds and performance, we did not calculate the specific cross-section related to the given geometry of this block.

A cutoff for the reaction occurs at photons with energies below 2 MeV. This is detrimental to the analysis desired to be performed, since almost all the neutron sources are created with photons close to 1.6654 MeV, hence, utilizing this library is not useful.

The issue appears to arise within the cross-section model. Instead of observing the expected cutoff at 1.6654 MeV for the ^{9}Be(γ,n)^{8}Be reaction, there seems to be a noticeable deviation or step occurring at exactly 2 MeV. We need to update this to obtain the correct corresponding production.

Many efforts were performed in order to achieve a photonuclear reaction utilizing GEANT4 libraries at this energy scale with no success. In particular, an in-depth analysis of the different models used for photonuclear production was carried out by carefully checking all relevant libraries. One of these is the *G4PhotoNuclearCrossSection* library under the hadronic processes cross-section libraries. A minimum energy variable was found with the 2 MeV minimum energy threshold. Upon modifying it, null results were found, leading us to believe that this is more of a low-energy model problem.

During discussions for this, we stumbled upon Robinson A. updated photonuclear calibration libraries [21]. As part of his work, Robinson. A realized that the scattering processes between neutrons and bubble chamber liquid targets were incorrect. As part of updating this, in the next subsection, we discuss these updated libraries which will bring useful corrected data for the nucleus recoils.

5.1.2 Robinson A. Updated Library

In [21], Robinson A. gathered and analyzed all available information concerning the $^{9}\mathrm{Be}(\gamma, n)^{8}\mathrm{Be}$ photonuclear reaction in GEANT4. The initial goal was to update the libraries related to this reaction, but it became evident that the problem with the reaction cutoff persisted. During this analysis, Robinson A. identified an issue with the recoil nuclei produced by neutrons at the expected energies for photonuclear reactions. Consequently, he focused his efforts on improving the elastic scatterings libraries for neutron-target interactions, with Argon-40 being one of them.

Appendix B gives more details about GEANT4 internal libraries concerning neutron interactions as well as the proper guidance to update these libraries.

While a relevant bug, a direct fix for the photonuclear reaction within GEANT4 libraries is not trivial and presents many challenges for proper implementation. Hence, our second approach to simulation is employed. Continuing forward, we will be using the updated GEANT4 neutron elastic libraries.

5.2 Neutron Particle Generator

The next approach for neutron generation via photonuclear reaction is to manually create a Monte-Carlo particle generator and simulate them in GEANT4. This has a major advantage over the previous method: The control of all variables. As we mentioned in Section 4, the study of the properties of the photo-neutrons is known to a certain analytic precision. For this, in this section, we will review the process in which this method was deployed. Essentially it ends in a macro generator.

5.2.1 Radioisotope Simulation

The first step in this approach is to generate photons with the corresponding energies of the suitable isotopes in the radioisotope geometry. For this, we implement a macro that performs the following:

1. Set a "Flag" so that the geometry generated in the SBC is only the calibration tube chamber[2].
2. Generate photons inside the radioisotope disk with the corresponding energies of selected channels for ^{58}Co, ^{124}Sb and ^{207}Bi.
3. Record relevant information at the point of interaction of the photon with the beryllium-9. This information is then printed into a text file called *photoNpoints.txt*. These recorded points will be where the neutrons will be emitted. Further discrimination is performed later. These macros can be run as jobs or locally in the GEANT4 SBC geometry, they go by the name *photoNcalibration1(Radioisotope).mac*, where Radioisotope can be 58Co, 124Sb_low, 124Sb_high and 207Bi.

For our purpose, let us analyze the assumption that the first point of interaction can be the point of a photonuclear reaction. Firstly, as of right now, we are not involving any kind of rate of interaction calculation, i.e., we just want to find points where interactions of photons occur, the photon-to-neutron cross-section is not being considered. Secondly, let's take a look at the mean free path for the reaction in beryllium-9. Using an approximate for a photon of energy of 1.8 MeV[3] we find that the free mean path

$$\ell = \frac{1}{\sigma(1.8 \text{ MeV}) \times n} \approx 10,000 \text{ cm} \tag{5.1}$$

where n is the number of atoms of beryllium-9 in a cubic centimeter and σ is the cross-section for the photonuclear reaction for a photon of 1.8 MeV of energy. As we can tell, this number is extremely high. More than the dimensions of the calibration chamber. Hence, we can approximate that the probability of interaction in the beryllium block is equally as unlikely in any part of the calibration chamber. Hence, any point of interaction can be counted.

Another important thing to notice is scatterings, since all photon-matter processes are being performed, a photon can lose energy throughout the interactions with the beryllium block, this will be accounted for by the first analysis performed. This is described in the next subsection.

5.2.2 Energy, Position and Angular Emission

After the photon interaction with the beryllium is acquired, the analysis for the neutron emission is performed. For this, let us review two key information that the *photoNpoints.txt* file has (using the corresponding energy and length units (MeV and cm)).

1. Energy of the photon at the point of interaction.
2. Coordinates for the point before interaction (point of generation or previous scatter).

[2]We do this to only record the interactions within the calibration chamber and also to avoid interactions with other materials in the detector that could interact with the beryllium

[3]This is a good approximation for an average given the used photon energies in the radioisotopes

3. Coordinates of the point of interaction.

Given this information, we can calculate all the variables we need for the neutron emission.

At this point, we must understand the following challenge. While GEANT4 allows to declare histograms for energy and angular distribution, it would be quite challenging to implement them into a simple macro. Since many variables are changing. For example, the angular dependency in the energy emission and the point of emission. Thus, we need to consider making a *macro generator*. By a generator, we mean a script that would allow us to write a GEANT4 macro for different neutrons all with corresponding energies and angular emissions given the photon interaction. We will call this macro generator *photoNcalibration2.cc* and will input the *photoNpoints.txt* and output GEANT4 macros for a correct neutron emission. Let us consider the remaining subsections of this method to be part of this macro-generator.

With these implications, the first step is to create a random variable between $-\pi$ and π with a bias given by the angular distribution of the cross-section mentioned in section 4.3.4. Let us observe that this distribution is not normalized and has an uncertainty in the linear term. In order to sample a random value of θ, first, a number is selected out of a normal distribution with a mean of 1.26 and a standard deviation of 0.11. Given this number, the cross-section is then normalized by numerically integrating from $-\pi$ to π and dividing the angular distribution function by this value. With this concluded, the next step consists of choosing a random number a between $-\pi$ and π and another one b between 0 and 1. The random number a is evaluated in the newly normalized angular distribution, if b is bigger than the evaluated value a, then a is taken as the randomized θ. In the other case, a new value of a and b are chosen until it meets the criteria. This is known as the Acceptance-Rejection Algorithm for continuous random variables [90]. We can plot an histogram of the used θ values and verify that they follow an angular distribution like the one expected. An example of this can be found in Figure 17. For ϕ, since there is no bias, a randomized number between 0 and 2π is chosen using a uniform distribution. A θ and ϕ are chosen for every neutron emission, they are stored in a specific vector, one for θ and one for ϕ.

Since there is a lot of ambiguity with the angular distribution. A special analysis without this bias was also be performed. To do this, the only variable to modify is θ, for this, we randomly select a number between $-\pi$ and π using a uniform distribution. This is also then stored in the θ vector for future emission.

Afterward, the points of emission of the neutrons are selected. For this, additional discrimination needs to be performed. As we mentioned in the previous subsection, photon scatters can occur and are registered in the output list of the photon macro. Thus, energy losses can happen, so at this point, the first discrimination is that the event must have an energy above the reaction threshold[4]. After this is done, the points of emission are stored in a vector for all three coordinates. Also, the photon energy can start to fill out a histogram, with a majority, if not all events in the radioisotope simulated energy.

Given the photon energy and the θ sampled (either with the bias or uniformly distributed),

[4]Since scatters are caused by non-photonuclear reactions, it is correct to assume that photons with less energy than the expected from the radioisotopes could theoretically produce neutrons. Since all the photon energies from the selected radioisotopes are close to the Q value of the reaction, it is highly unlikely that a scattered photon will produce a neutron. However, for practical purposes, we will impose the condition.

using equation 4.4, the neutron energy can be found. Afterward, this energy is stored in a vector.

Even though it seems like all the required variables for an accurate neutron emission are obtained (energy, point of emission, and angular emission), a big problem still is pending when it comes to angular emission. Before going into details about how these variables are written in the macro, we will tackle the aforementioned problem.

5.2.3 Rotation Matrix

The angular distribution presented in equation 4.7, relates the probability of the angle of emission for a neutron given the photon relative direction. By this, we mean the following: Let us imagine a photon is traveling perpendicular to the y axis on the negative region in a xy plane and interacts with a beryllium-9 atom at $(0, 0)$. Fixing $\phi = 0$ for practical uses, the scattered θ will be in the xy plane, with the best probability of a neutron emission being in the x axis. Given this, for practical purposes, when emitting a particle with a certain angular bias in GEANT4, it will be with respect to the reference frame of the detector. This will generate an incorrect angular emission of the neutron.

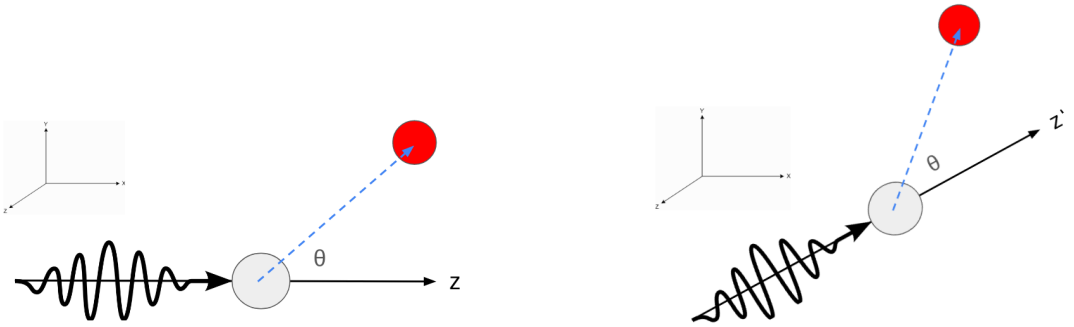

Figure 15: Angular Distribution for Neutron Emission in different frames. Left: Neutron (red ball) being scattered of a photon traveling perpendicular to the z axis seen from the reference frame of the detector. Right: Neutron being scattered of a photon traveling by a rotated z' axis seen from the reference frame of the detector.

To fix this, we need to rely on the point of photon emission or of previous scatter. Given the two given coordinates, we can create a directional vector for the photon[5]. Afterwards, we need to rotate the whole reference frame, so that the z axis is now perpendicular to this new directional vector.

[5]To obtain this vector, we just subtract the coordinates from the point of interaction with the coordinates of emission or last scatter.

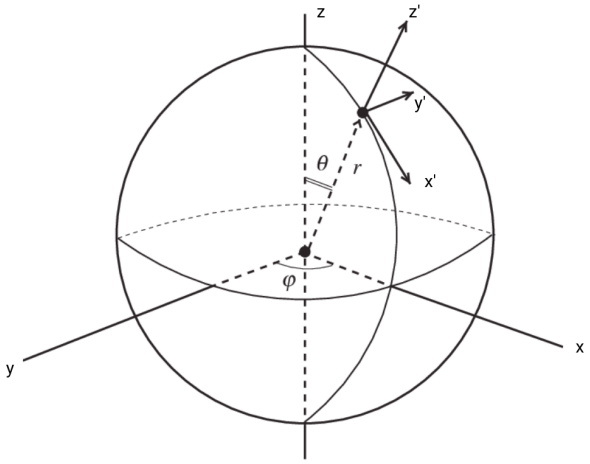

Figure 16: Schematic of the new coordinate systems required.

Using the schematic in Figure 16, in order to rotate from $(x, y, z) \rightarrow (x', y', z')$, the basis vectors from the original must be multiplied by a certain rule of transformation. This transformation is a rotation matrix, to obtain it we need to do rotations around the three axes, this process is well characterized by quaternions.

Unit quaternions, referred to as versors, offer a practical mathematical framework for expressing spatial orientations and rotations of objects within three-dimensional space. More precisely, they encapsulate details regarding an axis-angle rotation performed around an arbitrary axis [91].

The summary using the quaternion-based rotation matrix to achieve the corresponding rotation matrix is the following. Consider $\vec{n}$ the directional photon vector, lets normalize it so that $\hat{n} = \vec{n}/|n|$. Now, we find the angle between this directional vector and z as $\theta = \arccos\left(\hat{n} \cdot \hat{k}\right)$ where $\hat{k} = (0, 0, 1)$. Finally, lets construct a vector completely orthogonal to $\hat{k}$ and $\hat{n}$ by calling $\vec{b} = \hat{k} \times \hat{n}$, and then normalize it so that $\hat{b} = \vec{b}/|b|$. With this information, we are ready to construct the rotation matrix. Using the quaternion matrix rotation formulation, it's useful to define the following variables:

$$\begin{aligned} q_0 &= \cos(\theta/2) \\ q_1 &= \sin(\theta/2)\hat{b}_x \\ q_2 &= \sin(\theta/2)\hat{b}_y \\ q_3 &= \sin(\theta/2)\hat{b}_z \end{aligned} \tag{5.2}$$

Analyzing this parameter we can make a key observation that simplifies further calculations. Lets assume a random $\hat{n} = (a, b, c)$, since given our reference frame, $\hat{k} = (0, 0, 1)$, then $\hat{b}_z$ is always 0. This makes sense since there is no way to get an orthogonal vector in the same direction as $\hat{k}$. With this remark, we can construct the rotation matrix Q so that $\vec{x'} = \bar{\bar{Q}}\vec{x}$ as:

$$\bar{\bar{Q}} = \begin{pmatrix} q_0^2 + q_1^2 - q_2^2 & 2q_1q_2 & 2q_0q_2 \\ 2q_2q_1 & q_0^2 - q_1^2 + q_2^2 & -2q_0q_1 \\ -2q_0q_2 & 2q_0q_1 & q_0^2 - q_1^2 - q_2^2 \end{pmatrix} \tag{5.3}$$

With this, we can find the new unit vectors by multiplying the original unitary vectors times the matrix.

$$\begin{aligned}\hat{u} &= (q_0^2 + q_1^2 - q_2^2, 2q_2q_1, -2q_0q_2)\\ \hat{v} &= (2q_1q_2, q_0^2 - q_1^2 + q_2^2, 2q_0q_1)\\ \hat{w} &= \hat{u} \times \hat{v} = \hat{n} = (2q_0q_2, q_0q_1, q_0^2 - q_1^2 - q_2^2)\end{aligned} \tag{5.4}$$

where $\hat{u}$, $\hat{v}$ and $\hat{w}$ are the new rotated coordinate system unit vectors. This will become important for numerical implementation in the next subsection. For the moment, the 6 coordinates u_x, u_y, u_z and v_x, v_y, v_z are stored each one in a vector. Since $\hat{w}$ is just the normalized directional vector, it's not necessary to store, as a matter of fact, due to the implementation, it is not required at all.

This procedure is not required for the isotropic emission of neutrons. Any differences will be discussed in the analysis section.

5.2.4 Macro Writing and Job Submission

After all the previous steps are done, we can start to write GEANT4 macros to start running simulations. The acquired quantities are, as a recap:

- Neutron Energy
- θ and ϕ (With a angular distribution or isotropically).
- Point of Emission.
- New x', y' and z' coordinates.

To start, all the available data is being stored in vectors, this is done so that photonuclear analysis can be performed at once and then macro creation can be done in blocks. By this, we mean that for every macro, 1200 neutrons will be simulated. The way this is done goes as follows. First, we denote our verbosity and flags in the macro, afterward all the relevant information is declared and finally, the command */runBeam 1* is written[6]. We will focus on the middle step, that is, how the information is implemented for simulation.

The first steps are simple enough, in the macro declare the particle as */gps/particle neutron*, the energy by using the command */gps/ene/mono* [Energy] MeV, and the position by */gps/position* [x, y, z] cm.

The following two become more complicated, starting with rotating the detector's reference frame. GEANT4 command */gps/pos/rot(1/2)* allows to change the unit vector in x and y (corresponding to rot1 and rot2 respectively) to the desired one. They are by default set to $(1, 0, 0)$ and $(0, 1, 0)$ correspondingly. For this, given the six variables stored from the rotation matrix, we declare the new unit vectors for x and y given each neutron. Finally, the angular emission is given by θ and ϕ. While there are a couple of commands that allow for a specific angular emission, we use */gps/direction*$[a, b, c]$. Here, a, b, and c are the coordinates of the directional vector in which the particle will be emitted. In order to denote these coordinates, we will use spherical coordinates, where $a = \sin\theta\cos\phi$, $b = \sin\theta\sin\phi$ and $c = \cos\theta$. This

[6]In practice, we could run thousands of events with the same angular distribution and energy, but this is un-practical since it's unrealistic to believe that every neutron will be emitted from the same point and with the same characteristics.

creates a plane rotated in the θ and ϕ which then will emit a particle perpendicular to it at the notified point of emission.

With this, the macro generator is completed. All the macros are then saved in a specific folder corresponding to the macro number. Inside this directory, a .sh file can be found as well. *photoNcalibration2.cc* has the ability to send the desired macros as jobs to compute.canada.ca. or one could manually run every desired macro. After every job or run is finished, the most important output file is called *Information.txt*. The content of this file will be discussed next. If one desires to send all the macros to run as jobs, the output after all the jobs are done can be stored in one single folder with all the *Information.txt* files, each with a sub-index corresponding to the macro number.

5.3 Analysis

Following the completion of simulations for all radioisotope neutron sources, the next crucial step involves analyzing their interactions with the liquid-argon. To facilitate this, a script is employed to filter the relevant information from the *Information.txt* files, isolating the events associated with argon nucleus recoils. These files encompass a wide range of interactions, including neutron-electron scattering, photon interactions, scintillation emissions, and more. It is convenient to discern and record only the events related to neutron-nucleus interactions accurately. Nucleus recoils exhibiting energies below 0.1 keV are disregarded, as they fall below the expected threshold. Consequently, any events registering values lower than this threshold are not taken into consideration.

As discussed in preceding chapters, several significant reactions are of interest in liquid-argon, including neutron-nucleus interactions in ^{40}Ar, Thermal Neutron Capture resulting in ^{41}Ar, and Thermal Neutron Capture in ^{36}Ar, leading to ^{37}Ar. Additionally, the possibility of neutron-argon scattering exists in all relevant argon isotopes, namely ^{36}Ar and ^{38}Ar. This consideration arises from the natural abundance of argon, composed of 99.6% ^{40}Ar, 0.34% ^{36}Ar, and 0.06% ^{38}Ar [92]. Therefore, it is essential to initially identify which reactions occur within the detector to enable a comprehensive analysis of each. In this final section, we present the results of various analyses of neutron-nucleus interactions and provide detailed insights for practical implementation. The analyses are conducted using two different simulation schemes: one employing the neutron particle generator with an angular bias and the other featuring isotropic emission. A comparative assessment of the two methods will be discussed within each section. All relevant plots for the discussed analysis of each source and simulation scheme are available in Appendix E, with the most pertinent and illustrative plots highlighted in this subsection.

5.3.1 Neutron Production Rate Given Simulations

Before tackling the recorded neutron interactions, it will be important to obtain the correct neutron rates for proper normalization and simulation analysis. When one simulates photons for neutron production inside the radioisotope source, this is being performed isotropically. Hence a collective flux is being formed around the disk geometry. One must consider the full experimental geometric setup for a correct photon rate and flux. The full calculation of this flux is performed in Appendix C. Theoretically, the photon source and hence, the neutron rate, would be given by the natural activity of the radioisotope source's mass. However, as we calculated in Appendix A and reported in Table 4, these rates are in order of millions

per second per gram. This is an unrealistic detection goal since the detector's dead time is in order of seconds. Given a detector's geometry efficiency of 0.1%, it would still mean thousands of events are occurring every second. For this, it's suitable to fix the photon source to a realistic number aligned with the detector's capabilities. A more detailed description of this is can be found in Appendix C as well. The theoretical neutron rate for the radioisotope sources is

$$R(N) = R \times \delta x \times \sigma_{\mathrm{PN}} \times BR \times \rho_A \tag{5.5}$$

where $R \times \delta x$ is the photon flux per centimeter, which is calculated and argued in Appendix C, σ_{PN} is the photonuclear cross-section for the photon energy, BR is the branching ratio of the photon emission and the beryllium nuclei density $\rho_A = N_A/A \times \rho$ with $A = 9$, N_A Avogadro's constant and ρ the beryllium density in g cm^{-3}.

Taking into account the considerations outlined in this discussion, we have the flexibility to select arbitrary yet physically feasible gamma sources for each radioisotope. The chosen sources should ideally generate only a small number of neutrons per second, resulting in a few dozen neutron detections per hour. The selected emission rates are presented in the subsequent table.

Source	Activity (μCi)	Activity (Bq)
^{58}Co	100	3.7×10^6
^{124}Sb	1	3.7×10^4
^{207}Bi	10	3.7×10^5

Table 5: Chosen Gamma Rates for every radioisotope source for an accurate neutron detection rate.

As we can see, the rates are up to 8 orders of magnitude lower per gram than the ones reported in Table 4. The expected neutron rates and interaction rate are reported below using these sources. Before we perform this, it will be important to report the following simulation-related quantities.

Given the number of neutrons simulated, we can find the physical time required for this number of neutrons to be generated.

$$t_{\mathrm{emi}} = \frac{\text{Neutrons Simulated}}{\text{Neutron Rate } (R(N))} \tag{5.6}$$

This, however, while useful for understanding the normalization time for the detection rate in our simulations, is not for practical use since neutron detection only occurs when there is an interaction with the liquid-argon. Utilizing simulations we can obtain geometrical efficiency, which is defined as

$$\epsilon_{\mathrm{geo}}^{\mathrm{MC}} = \frac{\text{Neutrons interacting with the LAr}}{\text{Neutrons Simulated}} \tag{5.7}$$

where the subscript MC stands for Monte Carlo. Given this efficiency, a great approximation for the desired number of events given a radioisotope source will be

$$\text{Neutrons interacting with the LAr} = \epsilon_{\mathrm{geo}}^{\mathrm{MC}} \times \text{Neutron Rate} \times t_{\mathrm{emi}} \tag{5.8}$$

Another remarkable interesting simulation-only quantity we can obtain is the (n, γ) ratio, which gives us a Monte Carlo-only efficiency of the neutron production given any number

of photons. The real observable differences will be at the neutron interactions with liquid-argon. In fact, as we can see since the angular emission or energy of the neutron has nothing to do with what kind of bias we are using, the efficiency of the photon to neutron is equal for both cases. The calculated efficiencies are reported here.

Source	^{58}Co	^{124}Sb-low	^{124}Sb-high	^{207}Bi
$\epsilon^{\mathrm{MC}}_{\gamma\to n}$ Efficiency (%)	16.675	16.635	15.519	14.747
Neutrons Simulated	2167750	2162550	2017470	1917110

Table 6: MonteCarlo Efficiencies and neutron production given 13,000,000 simulated photons for every corresponding radioisotope source.

Given this, we show the simulation results for the neutron production and efficiencies. The statistics goes as follows: For every source, 13,000,000 photons with the corresponding radioisotope energy were simulated being emitted from the calibration disk. The scatters were recorded and the macros were run with an angular distribution and a uniform distribution on θ. The following Table highlights important physical and numerical efficiencies for each simulation scheme.

Neutron Source	Simulation Scheme	$R(N)$ (n/s)	t_{emi} (hr)	$\epsilon^{\mathrm{MC}}_{\mathrm{geo}}$ (%)	$R_{\mathrm{int}}(N)$ (n/hr)
^{58}Co at 100μCi	Angular Bias	2.656	226.714	1.046	100.104
	Isotropic			1.104	105.560
^{207}Bi at 10μCi	Angular Bias	3.022	176.218	1.112	121.082
	Isotropic			1.107	120.492
^{124}Sb - *low* at 1μCi	Angular Bias	3.077	195.225	1.058	117.300
	Isotropic			1.129	125.117
^{124}Sb - *high* at 1μCi	Angular Bias	0.066	8491.042	1.551	3.686
	Isotropic			1.606	3.817

Table 7: Neutron Production Rate, Time of Emission, Geometric Efficiency and Neutron Interaction Rate for every source and simulation scheme.

The data presented in Table 7 play a crucial role in refining our simulations by converting them from arbitrary numerical values into practical rates. Specifically, the neutron emission histograms have been normalized to $R(N)$, while the nucleus recoil energy spectrum is normalized to $R_{\mathrm{int}}(N)$. Further insights regarding neutron interactions will be provided in the Multiplicity section of the analysis, as it relates to different types of recorded events. For now, we offer a comprehensive overview of the neutron energy emission rates for each source, along with their corresponding angular distributions (bias and isotropic).

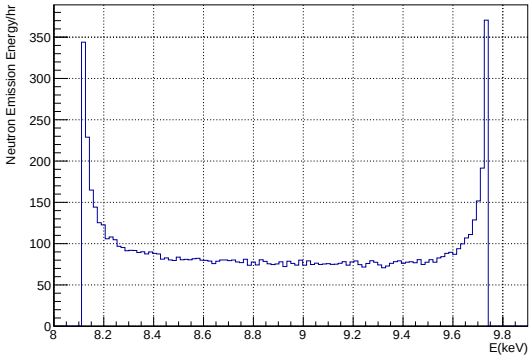

(a) ^{58}Co/^{9}Be neutron source energy distribution rate for an angular bias.

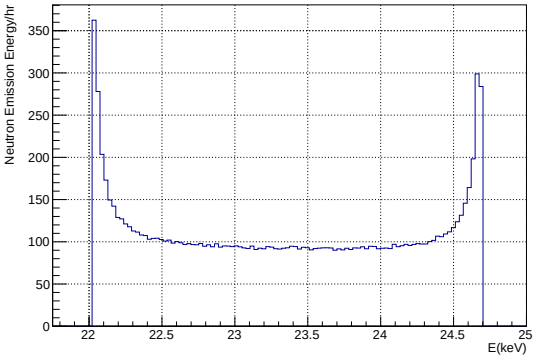

(b) ^{124}Sb-low/^{9}Be neutron source energy distribution rate for an angular bias.

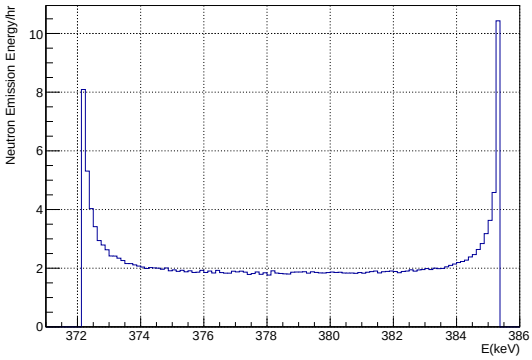

(c) ^{124}Sb-high/^{9}Be neutron source energy distribution rate for an angular bias.

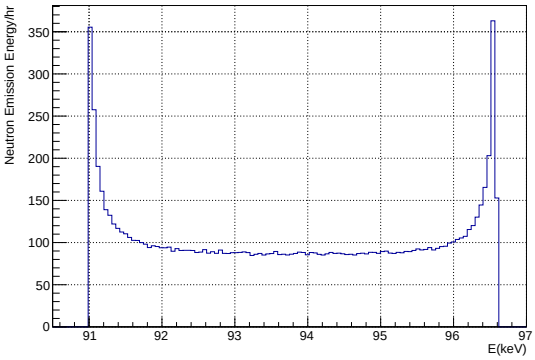

(d) ^{207}Bi/^{9}Be neutron source energy distribution rate for an angular bias.

Figure 17: Neutron Energy Spectrum Histogram for selected radioisotope-neutron sources given an angular distribution.

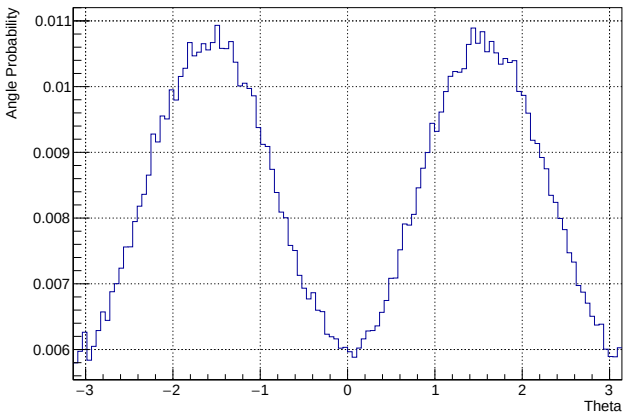

(a) θ sampling histogram given an angular distribution.

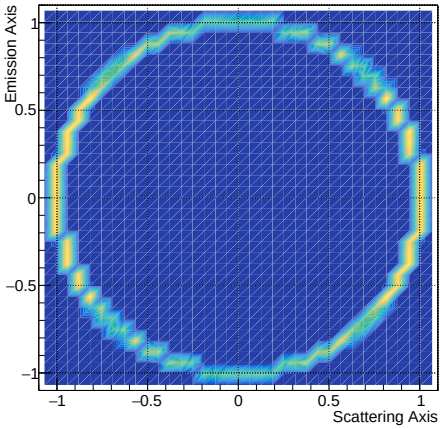

(b) Unitary Emission Vector.

Figure 18: Angular information given the neutron production simulation for a ^{124}Sb-high/^{9}Be neutron source with an angular distribution.

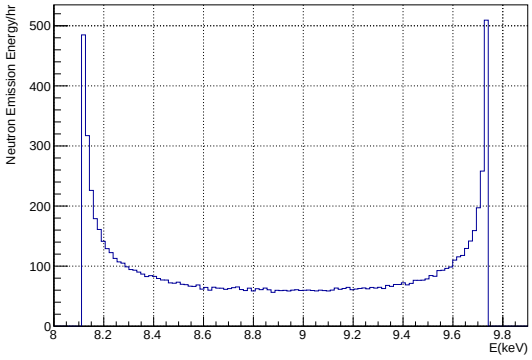

(a) ^{58}Co/^{9}Be neutron source energy distribution for an uniform angular distribution.

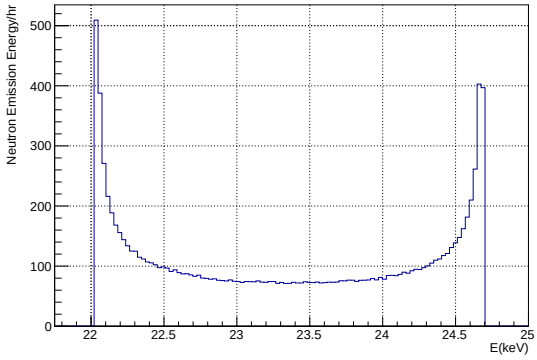

(b) ^{124}Sb-low/^{9}Be neutron source energy distribution for an uniform angular distribution.

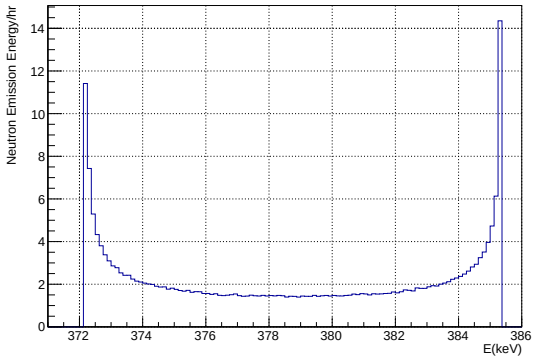

(c) ^{124}Sb-high/^{9}Be neutron source energy distribution for an uniform angular distribution.

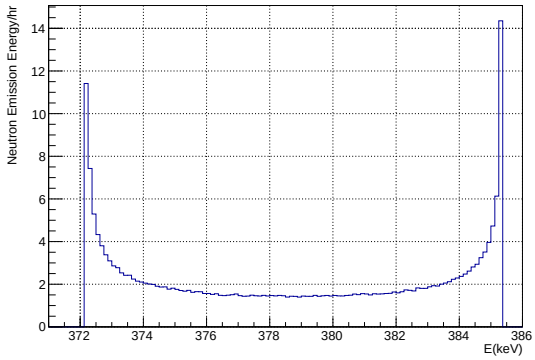

(d) ^{207}Bi/^{9}Be neutron source energy distribution for an uniform angular distribution.

Figure 19: Neutron Energy Spectrum for selected radioisotope sources given an uniform angular distribution.

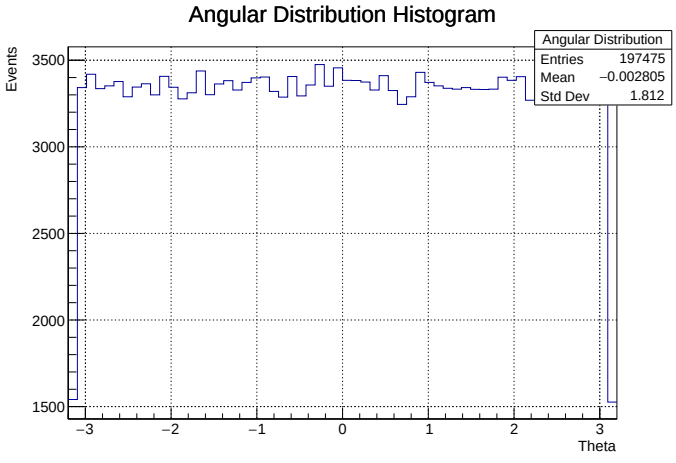

(a) θ sampling histogram given an uniform distribution.

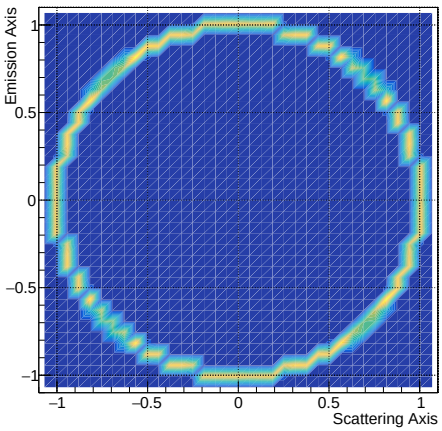

(b) Unitary Emission Vector.

Figure 20: Angular information given the neutron production simulation for a ^{124}Sb-high/^{9}Be neutron source with an uniform angular distribution.

In the respective plots denoted as (b) in Figures 18 and 20, the X-axis represents the neutron emission scattering axis, while the Z-axis indicates the photon propagation direction. Consequently, we can deduce that in the case of angular bias, neutron emission is predominantly concentrated around $\pi/2$ and $-\pi/2$, whereas in the uniform case, neutron emission is isotropic, as expected. A noteworthy aspect to examine is the distribution of neutron energy. Although the energy distributions appear similar, the angular bias scenario results in more events occurring between the maximum and minimum energy points, whereas the isotropic emission case exhibits the opposite trend. This phenomenon is a direct consequence of the neutron energy spectrum as defined in Equation 4.4 and shall be studied as the main difference of our study.

The geometric MonteCarlo efficiency remains consistent with all schemes and sources. This means that, around 1% of all neutrons being simulated interact once or multiple times with the liquid-argon. This information is useful given the geometric boundaries of the detector construction and the neutron production rate. With this, the time and source (photon) rate was selected for the proper statistic required.

Further analysis reveals that, for the isotropic emission scheme, interaction rates have increased for almost all sources by a small margin. In the case of the ^{207}Bi source, the rates remained largely consistent, while for ^{124}Sb - *low*, there is a notable difference, with approximately 7 more events per hour compared to the angular bias case. Additionally, for ^{58}Co, there is also a significant improvement, with nearly 6 more events per hour. This leads us to the conclusion that neglecting the angular distribution of the photonuclear reaction results in a higher rate of interactions. Whether this difference is significant enough to warrant experimental validation remains to be determined.

5.3.2 ^{124}Sb High/Low Identification

Before delving further into our discussion about observable quantities, it is essential to clarify the specific combination of the two available gamma decay channels employed for ^{124}Sb. In practical terms, the neutron energy spectrum is a composite of these two channels, with their rates constrained and directly proportional to their respective branching ratios. Notably, the probability of ^{124}Sb *low* surpasses that of the *high* counterpart. Consequently, given the production rate, there will be a substantially greater accumulation of events within the low-energy range. It's worth underlining that the number of emitted neutrons remains consistent for both scenarios, necessitating the multiplication by a fraction of the reported statistics to obtain accurate results.

The branching ratios for the *low* and *high* gamma decays are 47.79% and 5.51% respectively. With this, given the N number of neutrons simulated, then the percentage of neutrons as a fraction of the simulated neutrons from the *high* decay is

$$\%(high) = \frac{\mathrm{BR}(high)}{\mathrm{BR}(low)} \times N \times 100 \tag{5.9}$$

which is approximately 11% of the simulated neutrons. By this, we mean, that for every 100 neutrons simulated, 11 are from the *high* decay. All statistics corresponding to the *high* branching will be multiplied by this factor. While for the *low*, they will be multiplied by the complement of the fraction $(1 - \%(high))$. If the reported quantity is an integer number then it will be rounded up to the closest. From now on, the reported data will only be for three sources: ^{58}Co, ^{124}Sb, and ^{207}Bi.

5.3.3 Event Multiplicity

When discussing the number of events, its important to highlight two different ideas that need to be clear: The *number of interactions* and the *number of interacting neutrons*. Analyzing neutron's properties while traveling in a material, due to its short free mean path in argon, it has the capability of scattering multiple times in the detector. Every scatter is considered an *interaction*. In practice, it would be convenient to have only one scatter per interactions, reason that will be apparent and will be discussed in later sections, but for now, it key calculate the ratio of multiplicity per number of interaction neutrons. Table 8 reports the percentage of interaction for multiple number of events per neutron for both simulation schemes and neutron sources.

Isotope	Simulation Scheme	1 (%)	2 (%)	3 (%)	4 (%)	5+ (%)
^{58}Co	Angular Bias	92.78	6.40	0.70	0.10	0.00
	Isotropic	92.07	7.17	0.66	0.08	0.00
^{124}Sb	Angular Bias	86.46	10.55	1.89	0.59	0.49
	Isotropic	86.68	10.26	1.93	0.60	0.51
^{207}Bi	Angular Bias	84.43	11.01	2.83	1.05	0.66
	Isotropic	84.82	10.81	2.62	1.14	0.58
Average	-	87.87	9.36	1.77	0.59	0.37
SD*	-	3.32	1.85	0.84	0.41	0.26

Table 8: Neutron-Argon interaction multiplicity percentages. Angular Bias: Angular Distribution and Isotropic: Uniform Angular Distribution. *Standard Deviation.

As our analysis indicates, the most probable scenario for interactions typically involves a single event on average. However, as we compute the averages for higher multiplicity rates, we observe increasing deviations. These deviations can be attributed to several factors, including limited statistical data and, most significantly, the energy channel. It is evident that as the energy of the neutron increases (ranging from ^{58}Co, the lowest, to ^{124}Sb, the highest), the likelihood of multiple interactions becomes more noticeable. Consequently, the low probability for multiple bubbles leads to the overall error to grow across all sources, necessitating more statistic.

On particular interest is the ^{124}Sb source, as the statistics for the 2+ bubble events are predominantly influenced by the "high" channel. Even with a 0.11 ratio, it is apparent that the contribution to multiple bubbles primarily stems from this branching ratio.This becomes evident during the statistical analysis of this source, as detailed in Table 7, the high channel for ^{124}Sb demonstrates higher statistical significance due to the greater number of neutrons produced and emission duration. Upon normalization to the interaction rate, it becomes clear that this channel contributes significantly to the statistics associated with multiple interaction events.

On a helpful note, let's present both the number of interactions and neutron interactions. This information can provide valuable data on the extent to which multiple interactions are being triggered by the simulated neutrons.

Isotope	Simulation Scheme	# of Interaction	# Neutrons
^{58}Co	Angular Bias	25861	22695
	Isotropic	27388	23932
^{124}Sb	Angular Bias	29674	23868
	Isotropic	31428	25346
^{207}Bi	Angular Bias	26990	21337
	Isotropic	26676	21233

Table 9: Number of Neutron-Argon Interactions and Number of Events. Angular Bias: Angular Distribution and Isotropic: Uniform Angular Distribution.

Following the neutron interaction rate data presented in Table 7, it is apparent that the isotropic source generates a relatively higher number of interactions. This observation aligns with the neutron energy distribution illustrated in Figures 17 and 19, where a concentration of events is observed at the higher end of the energy spectrum. In contrast, the angular bias case exhibits a more evenly distributed energy spectrum, with events scattered across the middle range of energies. This disparity suggests a potential overestimation of events in the isotropic case.

Having addressed this discussion, our focus now shifts to the different interaction channels. Given the analysis shared thus far, there is no immediate justification for disregarding multiple interaction events. They hold the potential to give valuable insights into the various reaction channels at play within the detector. Our next step involves delving into the analysis of isotope interactions. All specific multiplicity plots for every neutron source can be found in Appendix E.

5.3.4 Isotopes Interactions

As mentioned in the introduction to this section, it's important to identify the possible neutron interactions with the liquid-argon in order to understand the rate of desirable calibration relevant processes. The interactions are dependent on the neutron energy, thus, we should expect approximately a similar ratio of interactions with respect to the natural abundance of argon. The following are the results from the simulation schemes, Table 10 gives a brief overview of the physical processes for every detected argon isotope interaction channel.

Isotope	^{36}Ar	^{37}Ar	^{38}Ar	^{40}Ar	^{41}Ar
Reaction Channel	Elastic Scattering	Neutron Capture in ^{36}Ar	Elastic Scattering	Elastic Scattering	Neutron Capture in ^{40}Ar

Table 10: Possible reaction channels for neutron-Argon interactions.

As mentioned in the introduction, the most probable reaction channel should be, due to abundance, the elastic scattering in ^{40}Ar and neutron capture to ^{41}Ar. Table 11 offers a breakdown of events per isotope as a percentage of the total number of neutron interactions for all possible reaction channels.

Isotope	Simulation Scheme	^{36}Ar (%)	^{37}Ar (%)	^{38}Ar (%)	^{40}Ar (%)	^{41}Ar (%)
^{58}Co	Angular Bias	9.66	1.57	0.17	32.09	56.49
	Isotropic	9.85	1.52	0.22	33.55	54.84
^{124}Sb	Angular Bias	9.00	1.30	0.18	47.81	41.68
	Isotropic	8.77	1.01	0.22	48.90	41.06
^{207}Bi	Angular Bias	6.72	1.07	0.14	53.79	38.26
	Isotropic	6.55	0.99	0.14	54.53	37.77

Table 11: Neutron-Argon interactions percentages. Angular Bias: Angular Distribution and Isotropic: Uniform Angular Distribution.

As we can observe, the rates tend to be in the same order for all simulation schemes, however, they seem to be higher in the elastic channels for the isotropic emission. Again, this can be explained by the neutron energy shift in the spectrum, which tells us that at higher energies, for each corresponding source, the elastic scattering is enhanced.

The rate of interaction seems almost proportional to the desired composition of argon. In order to check this, we can add the ^{41}Ar contributions to the ^{40}Ar and so with ^{37}Ar and ^{36}Ar to inspect the full interaction composition of argon. Since the added processes occur due to the interaction with one of the three available isotopes, then we can conclude the following (taking an average over the two simulation schemes, since they are at similar orders).

Isotope	^{36}Ar	^{38}Ar	^{40}Ar
^{58}Co	11.30	0.19	88.48
^{124}Sb	10.04	0.20	89.72
^{207}Bi	7.66	0.14	92.17

Table 12: Percentages of Interactions in Natural Abundance Argon Isotopes across all Neutron Sources

As we can notice, there seem to be more Argon-36 interactions than expected, this could be for multiple reasons ranging from simulations parameters or statistical fluctuations, however, we must also remember that these interactions cross-sections are dependent on the energy of the neutron, thus, Argon-36 reactions could be benefited by the low-energy of the neutrons being simulated. This, however, is an open problem to resolve. We should maintain these interactions in their current state since they involve possible nucleation events in argon. It's crucial to retain these interactions rather than dismiss them, as they contribute substantial events. All isotope interactions histograms are presented in Appendix E. After providing the percentage breakdown of interactions, we can delve into the analysis of each of these processes, potentially yielding practical insights. However, before proceeding further, an aspect worth considering is the precise interaction point within the detector.

5.3.5 Point of Interaction

One significant advantage of employing simulations is the ability to explore complex variables that may be challenging to measure in practical experiments. One such variable is the point of interaction within the argon, which can provide valuable insights into the locations of scattering or interaction during a reaction, as well as practical simulation test. While this

interaction point is not directly measurable, it offers a valuable approximation of where various interactions are likely to occur. This information can serve as a foundation for future discrimination techniques aimed at reconstructing different interaction events.

As we mentioned in the introduction to this chapter, the calibration chamber is situated at the top of the SBC-LAr10 geometry. Therefore, it is reasonable to anticipate that the most probable interaction points will be located at the upper part of the detector. To visualize and better comprehend the detector's geometry, we will utilize GEANT4's visual toolkit.

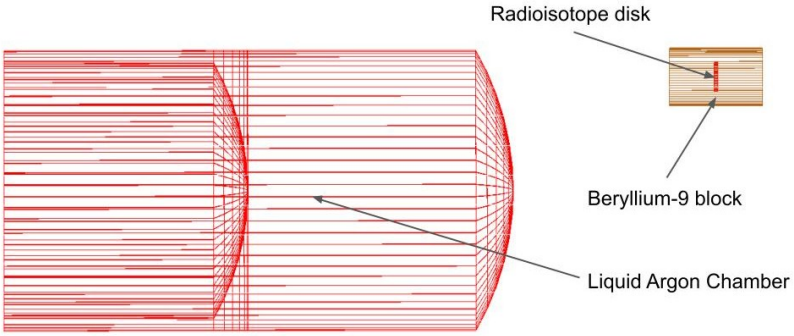

Figure 21: Schematic of liquid-argon chamber geometry with the calibration beryllium-9 block position as reference. r axis is vertical and z axis is horizontal in this reference frame.

A gap separates the neutron source from the liquid-argon chamber, and the geometry, as depicted in Figure 21, assumes the shape of a cylinder. This cylinder features a central, hollow tube extending from its bottom, capped at the top.

By plotting the relationship between r^2 and z, we can gain valuable insights into the vertical distribution of events and discern at what heights these events predominantly occur.

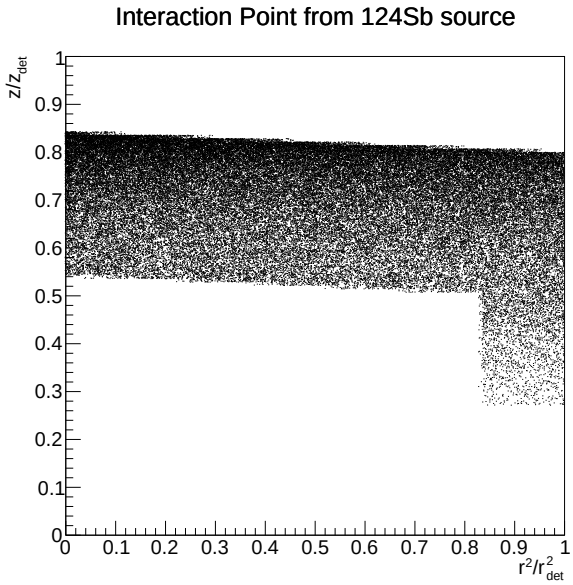

Figure 22: r^2 vs. z for point of interaction of neutrons in the liquid-argon. Normalized to the detector radius (r^2_{det}) and to the distance between the beryllium-9 to the bottom of the detector (z_{det}), respectively. Taken from ^{124}Sb source with an angular bias sample.

As we can see, for small radii values, an accumulation of events starts to appear at the top of the detector, this can understood by the detector geometry. The liquid-argon chamber has a bump in the top, thus allowing for a few events to interact in this position, we can see that these events are missing for big radii values. We can also analyze that some events appear at low values of z at almost the detector radius distance, we can interpret this as events that are going into the small gaps at the bottom of the detector.

The plot for all samples and simulation schemes looks similar, and yet, the important thing to notice is just where the accumulation of events is occurring. Which is at the top of the detector. An analysis of possible interaction points of emission patterns for some reactions or sources was performed as well. This can be seen in Figure 23, where we report the elastic scattering and capture processes point of interaction for all simulated neutrons.

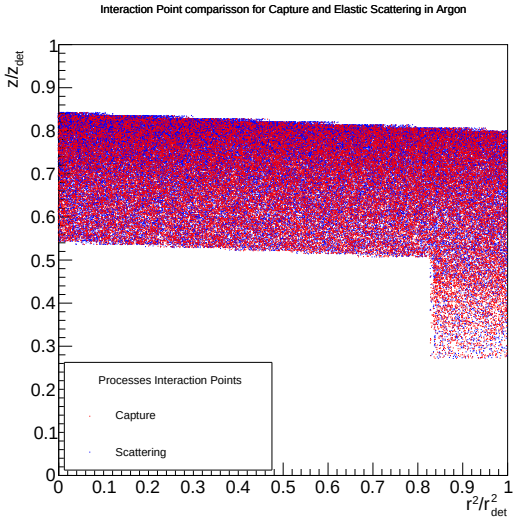

Figure 23: r^2 vs. z for point of interaction of elastic scatterings and neutron captures in liquid-argon chamber for all sources. Normalized to the detector radius (r^2_{det}) and to the distance between the beryllium-9 to the bottom of the detector (z_{det}), respectively. Taken from the angular bias sample.

As we can observe, as expected, there is no apparent pattern for any processes. The preference for scattering at the top of the detector is highlighted in the plot and serves as a reaffirmation tool for proper simulation running and detection.

5.3.6 Total Nucleus Recoil Energy

Following our interaction analysis, we can now start the discussion of the nucleus recoil energy spectrum across all interaction channels and multiplicities. As explained in Section 4, the nucleus recoil energy spectrum exhibits a distinct maximum, which is determined by the maximum elastic energy transfer. While this calculation was specifically conducted for Argon-40, it remains a valid estimate for the maximum recoil energy, given that this limit is directly proportional to the number of nucleons. Consequently, Argon-36 and Argon-38 maxima fall below this threshold. It's worth noting that, for the capture processes, we have not yet conducted an analysis of the nucleus recoil energy. Therefore, it becomes necessary to explore this aspect.

With this mentioned, Figure 24 presents the integrated simulated nucleus recoil energy rates, encompassing all processes and multiplicities, within both simulation schemes and across all neutron sources. This simulation provides the most accurate depiction of the energy distribution without employing any discrimination techniques.

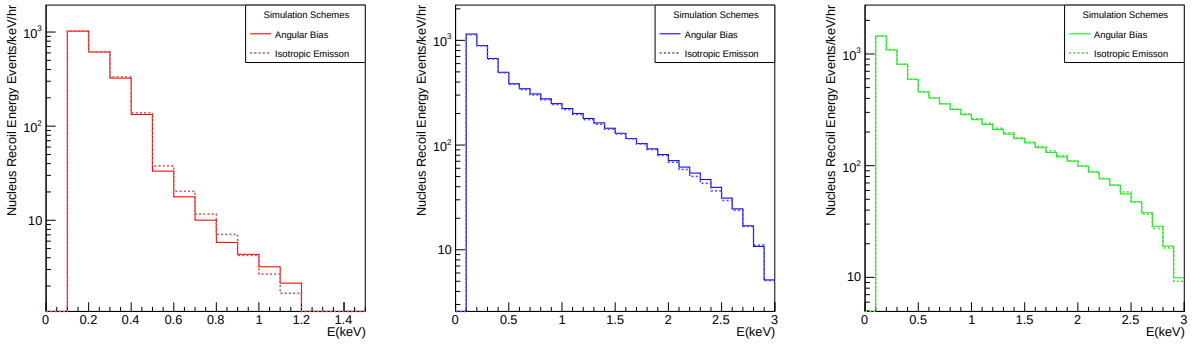

Figure 24: Nucleus Recoil Energy Rate Spectrum Histogram for all radioisotope-neutron sources given all simulation schemes. Left:^{58}Co/^{9}Be at 100 μCi. Center:^{207}Bi/^{9}Be at 10 μCi. Right:^{124}Sb/^{9}Be at 1 μCi.

As we can observe, nucleus recoil energy rate in both schemes looks similar with small deviations. We chose to plot from 0 to 3 keV since this is the threshold range and should give us an idea of events near the searched limit. As expected and reported in Table 4, for ^{58}Co, the maximum dies off near 1 keV, for the other sources is beyond 3 keV and the spectrum shows that. However, in both simulation schemes, an interesting peak forms above the expected 0.9 keV ^{58}Co neutron source maximum nucleus recoil energy. This is due to the neutron capture processes not being accounted for. This motivates us to perform an in-depth analysis, taking advantage of our simulation discrimination capabilities, of all the different energy spectrum regarding each interaction. In the next sections, we will present an analysis of the all the neutron-argon interactions contributing to the energy spectrum.

Before delving into this discussions, the energy spectrum presented, while theoretically viable, can be improved upon for practical uses since it poses unrealistic standards. Its important to employ the correct photon sources, interaction rates, thermodynamic properties and efficiencies to obtain a similar spectrum.

5.3.7 ^{40}Ar and ^{36}Ar Thermal Neutron Capture

As previously discussed in the calibration strategy section, neutron capture in argon serves as a valuable tool for calibration, harnessing both nucleation identification and scintillation arising from the photon emission during thermal capture. Notably, it's essential to keep in mind that scintillation linked to bubble formation does not manifest until the energy level reaches 5 keV. Therefore, neutron capture emerges as a particularly useful probe for sub-keV investigations. It's important to understand that the thermal capture of a neutron can only contribute once to the multiplicity. This process occurs at the end of the interaction chain or only one time. In other words, a neutron can trigger a capture event only once. Subsequently, Figure 25 shows the expected nucleus recoil energy spectrum attributable to neutron capture interactions.

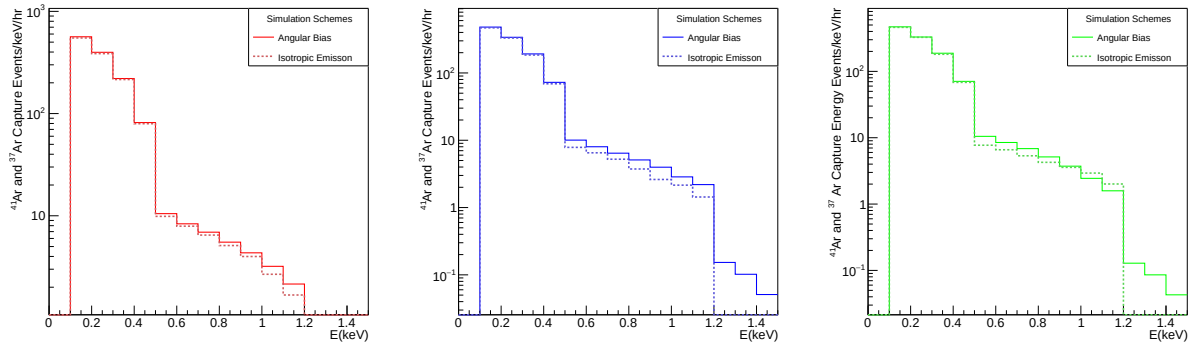

Figure 25: Energy Spectrum Histograms for ^{41}Ar and ^{37}Ar Nucleus Recoil for all radioisotope-neutron sources given all simulation schemes. Left:^{58}Co/^{9}Be at 100 μCi. Center:^{207}Bi/^{9}Be at 10 μCi. Right:^{124}Sb/^{9}Be at 1 μCi.

As evident from the data and as underscored in Table 11, the energy spectrum exhibits remarkable similarity between both simulation schemes. This spectrum is predominantly composed of events with energies below 0.5 keV. However, a few events are noticeable in the 0.5 keV to 1.2 keV range, which theoretically have the potential to introduce nucleation backgrounds if the energy threshold hovers around 1 keV. To do this, it is useful to separate between the ^{41}Ar and ^{37}Ar Capture events, we do this motivated by the idea that every capture event has a nucleus energy spectrum.

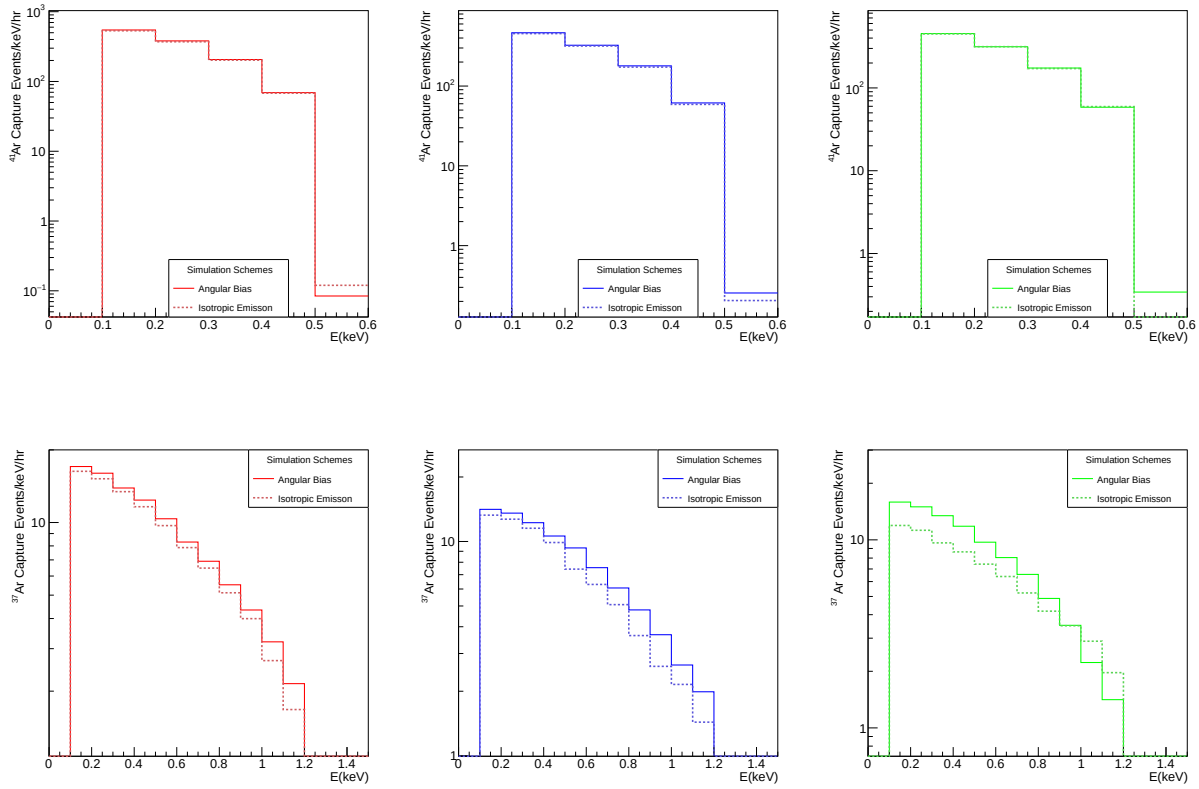

Figure 26: Energy Spectrum Histograms Comparison for ^{41}Ar and ^{37}Ar Nucleus Recoil for all radioisotope-neutron sources given all simulation schemes. Top: ^{41}Ar Capture. Bottom: ^{37}Ar Capture. Left:^{58}Co/^{9}Be at 100 μCi. Center:^{207}Bi/^{9}Be at 10 μCi. Right:^{124}Sb/^{9}Be at 1 μCi.

Figure 26 presents the nucleus recoil energy rate for ^{41}Ar and ^{37}Ar Capture. (All plots for every Capture Event can be found in Appendix E.).

Most of the events occurring in the 0.5 keV to 1.2 keV are coming from the neutron capture in ^{36}Ar. On average, this occurs $\approx$ 1% of time and just a few dozen events should be expected per hour. Thus, in high-running statistics, it could bring a noticeable background that should be taken into consideration. These events could be discriminated with the characteristic photon emission in capture processes and it should be analyzed further. Additional simulations and analysis should be performed to understand the complete relation and efficiency between the emitted photons and low-energy nucleation.

In the sub 0.5 keV range, ^{41}Ar capture events are occurring up to a couple of hundred per hour. As mentioned in the calibration strategy, this seems to be the most optimal sub-keV energy threshold calibration strategy. Similar to the previous case, the capture interaction emits a photon at a characteristic range, hence, further simulation, analysis, and tests are encouraged.

Given the energy threshold rates we discussed in the preceding sub-section, we can conclude the following: There are several dozen events surpassing the anticipated ^{58}Co threshold, primarily attributed to ^{36}Ar neutron capture. Additionally, there are numerous events, numbering in the hundreds, contributing to the sub-keV energy range as a result of neutron capture in ^{40}Ar. This observation is of significant importance and will serve as a focus point for further discussion in the upcoming sub-sections, particularly within the context of multiplicities.

5.3.8 ^{36}Ar and ^{38}Ar Elastic Scattering

During the theoretical development for the expected nucleus recoil threshold, we kept the main focus on ^{40}Ar, as it is the most abundant isotope of argon. As reported in Table 12, ^{40}Ar is responsible for nearly 90% of all interactions, hence the relevance of studying it. However, elastic scatterings from the other abundant argon isotopes also contribute to the full energy spectrum. Thus, a similar analysis should be employed as in the last-section.

Let us present Figure 27, which report for both simulation schemes the elastic processes contributions to the nucleus recoil energy rate spectrum for all neutron sources.

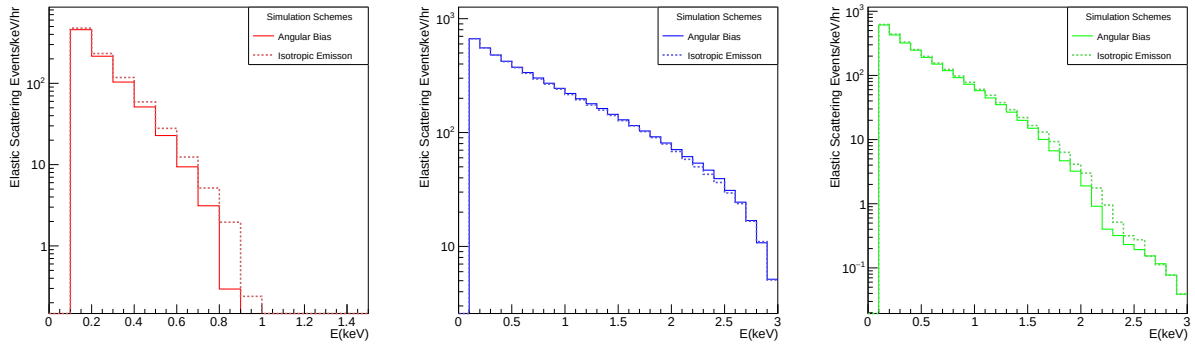

Figure 27: Energy Spectrum Histograms for Elastic Nucleus Recoil for all radioisotope-neutron sources given all simulation schemes. Left:^{58}Co/^{9}Be at 100 μCi. Center:^{207}Bi/^{9}Be at 10 μCi. Right:^{124}Sb/^{9}Be at 1 μCi.

Similar to the previous cases, both simulation schemes exhibit consistent behavior with no significant differentiation. As anticipated, the clustering of events around 1 keV in the ^{58}Co source is absent, suggesting that the events in this range were primarily a result of neutron capture. Another noteworthy outcome is the impact on the ^{124}Sb source, indicating a high dependence on capture events. To further analysis, its worth plotting the contribution of the other abundant isotopes in comparison to ^{40}Ar.

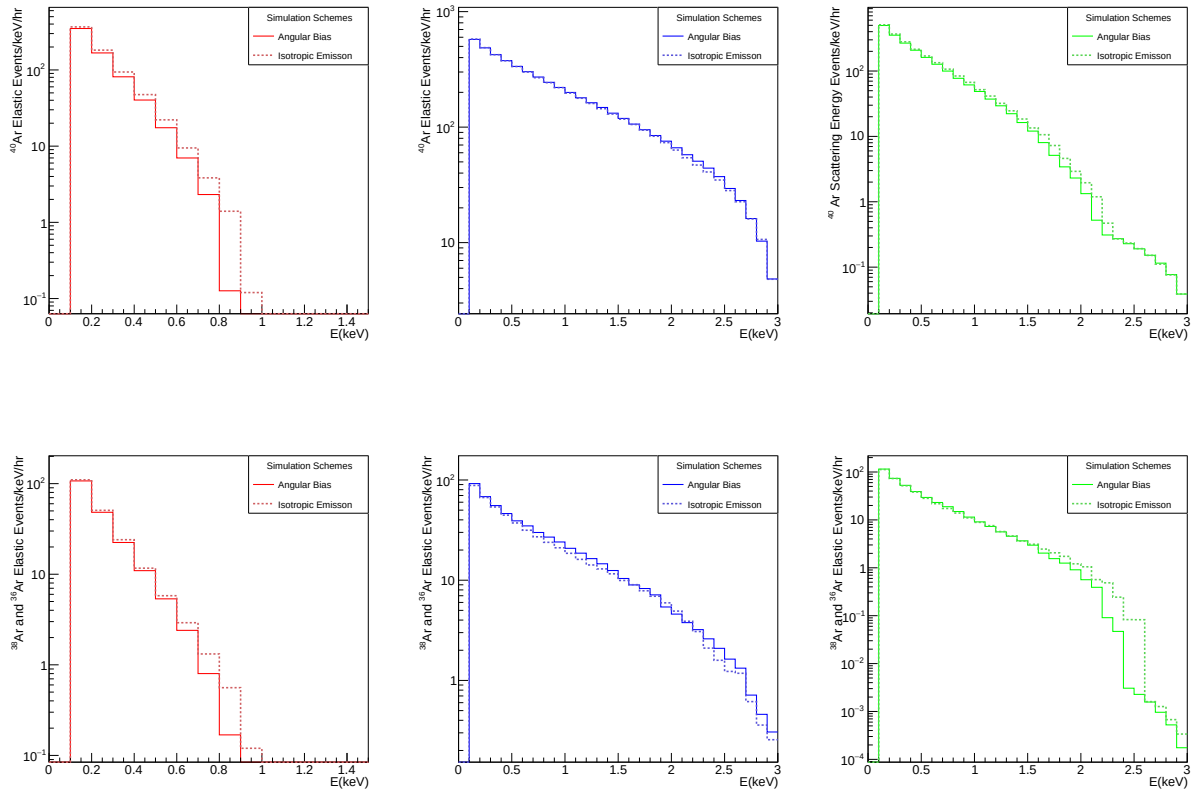

Figure 28: Energy Spectrum Histograms Comparison for ^{40}Ar and ^{38}Ar/^{36}Ar Nucleus Recoil for all radioisotope-neutron sources in the angular bias case. Top: ^{40}Ar Elastic Events. Bottom: ^{38}Ar and ^{36}Ar Elastic Events. Left:^{58}Co/^{9}Be at 100 μCi. Center:^{207}Bi/^{9}Be at 10 μCi. Right:^{124}Sb/^{9}Be at 1 μCi.

Upon initial examination, it becomes evident that elastic scattering in ^{38}Ar and ^{36}Ar is responsible for a substantial number of events within the sub-keV range. When we consider individual sources, such as ^{207}Bi and ^{124}Sb, interactions in ^{38}Ar and ^{36}Ar predictably result in lower interaction rates in the 1 keV and higher range. Another direct observation is in the case of ^{58}Co, where the maximum recoil energy for the less abundant isotope elastic interaction is below the calculated 0.92 keV for ^{40}Ar, aligning with the theory of nucleus recoil energy. Once again, it is crucial to emphasize the significance of certain observations that should not be overlooked. In the case of recoils in ^{36}Ar, they account for almost 10% of the recorded events in the simulations, making it essential not to neglect them. As for ^{38}Ar, although these events occur in approximately 0.1% of cases, it's still pertinent to consider them in situations involving high statistical significance.

In an early simulation attempt, E. Alfonso reported single event from elastic scatterings only in [18]. In this scheme, neutrons were simulated isotropically from the beryllium calibration

chamber. Importantly, argon capture recoils were not considered in this study. Considering only the elastic scatterings, the histogram behavior and rates coincide with our results and reaffirm the high-statistic nature of our analysis. To make a full comparison, it is important to discuss single bubble events and their relevance to our study. A single bubble elastic only scattering nucleus recoil histogram is also present in Appendix E.

5.3.9 Single Bubble Nuclear Recoil Rate

Up to now, our analysis has focused on the examination of processes contributing to the overall nucleus recoil energy distribution rate, considering all interactions regardless of their multiplicity. However, for a comprehensive and detailed analysis, particularly within the context of neutrino and dark matter searches, it becomes crucial to examine single bubble events more closely. In argon, the mean free path for neutrons spans orders of centimeters, guaranteeing regular occurrences of multiple interactions, as presented in Table 9. Nonetheless, from a practical standpoint, neutrinos or WIMP's are expected to interact only once within the detector. Therefore, it is more pragmatic to delve into the rates of single bubble events in the context of the specific physics searches being conducted.

An additional advantage of this approach arises from the discrimination techniques employed by SBC. When more than one bubble is formed, the cameras and acoustic detection system can promptly veto the event. Consequently, single bubble event rates represent a realistic and practically attainable quantity, aligning closely with the physics search objectives.

Figure 29, we present the single bubble event rate for nucleus recoil energy for both simulation schemes and all neutron sources.

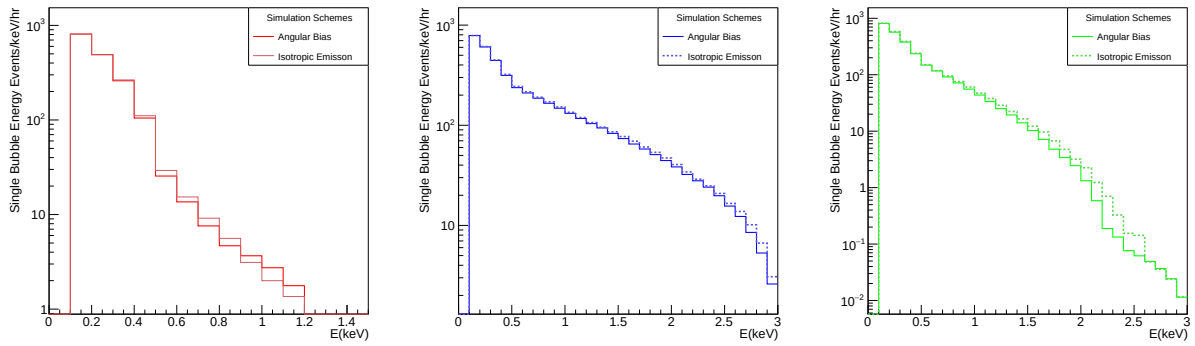

Figure 29: Energy Spectrum Histograms for Single Bubble Event Rate for Nucleus Recoils for all radioisotope-neutron sources given all simulation schemes. Top: Angular Bias. Bottom: Isotropic Emission. Left:^{58}Co/^{9}Be at 100 μCi. Center:^{207}Bi/^{9}Be at 10 μCi. Right:^{124}Sb/^{9}Be at 1 μCi.

This result holds fundamental significance for calibration techniques, representing the most practical assessment of the expected nucleus recoils. Just as in Figure 24, we can distinguish the presence of neutron capture events and events with energies in the 0.1 keV to 3 keV range. A similar analysis to that conducted for the multiple interaction rate can be applied to this result. For a more detailed examination, all specific interaction-related plots for single bubble event rates can be found in Appendix E. We encourage readers to analyze the performance and behavior of these plots, which remain consistent with the presented above.

For a full behavioral performance, we can plot all three sources in a single plot for all simulation schemes and compare with E. Alfonso results in [18] (and in Figure 10).

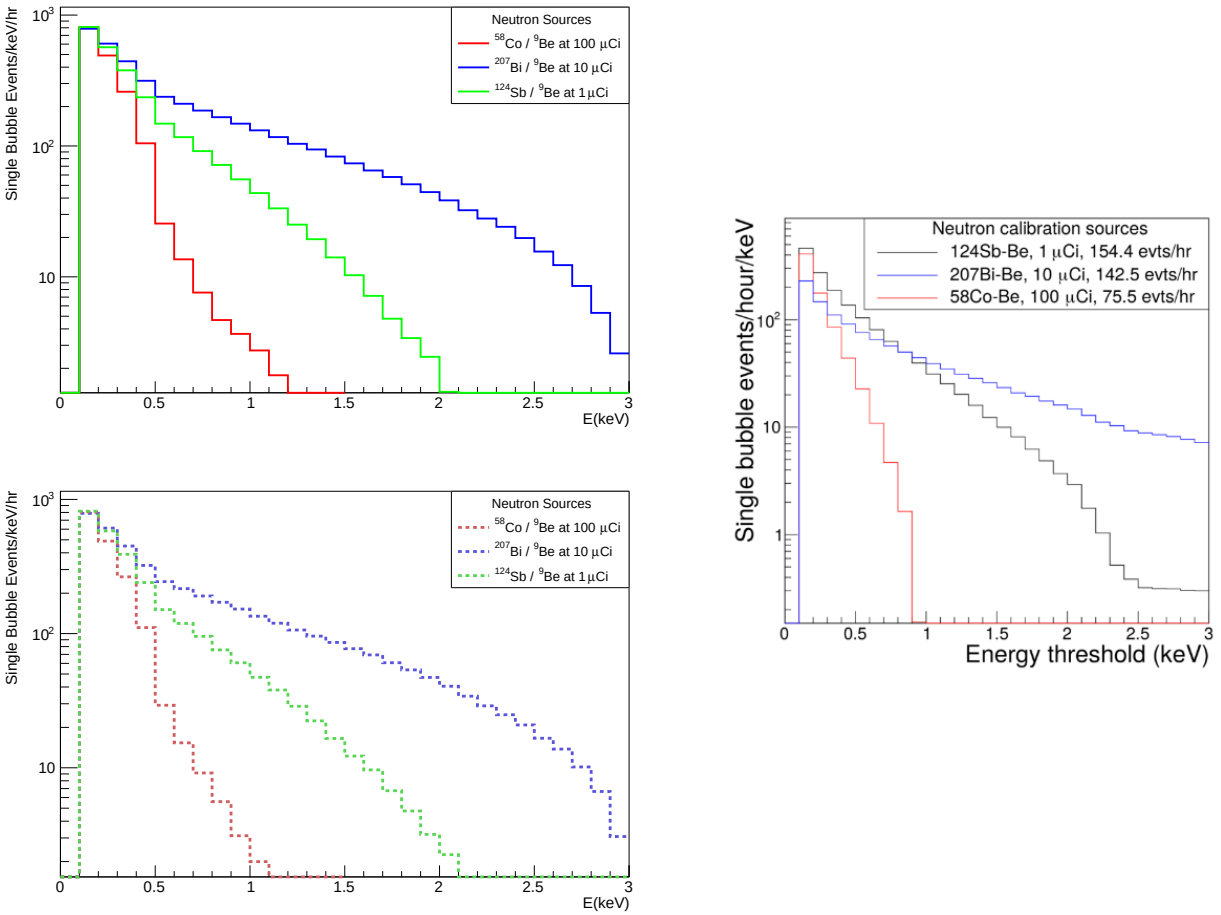

Figure 30: Energy Spectrum Histograms for Single Bubble Event Rate for Nucleus Recoils for all radioisotope-neutron sources given all simulation schemes. Top Left: Angular Bias. Bottom Left: Isotropic Emission. Right: E. Alfonso simulations [18].

While the performance, rates, and behavior of E. Alfonso simulations are generally comparable, it is essential to note that they do not account for argon capture events previously discussed. The incorporation of these events results in a more precise representation of the single bubble rates, especially in close proximity to the threshold limits in the ^{58}Co source.

To establish a comparable representation, it is imperative to contrast Elastic-only scatterings with E. Alfonso's simulations. This comparative analysis is presented in the following figures:

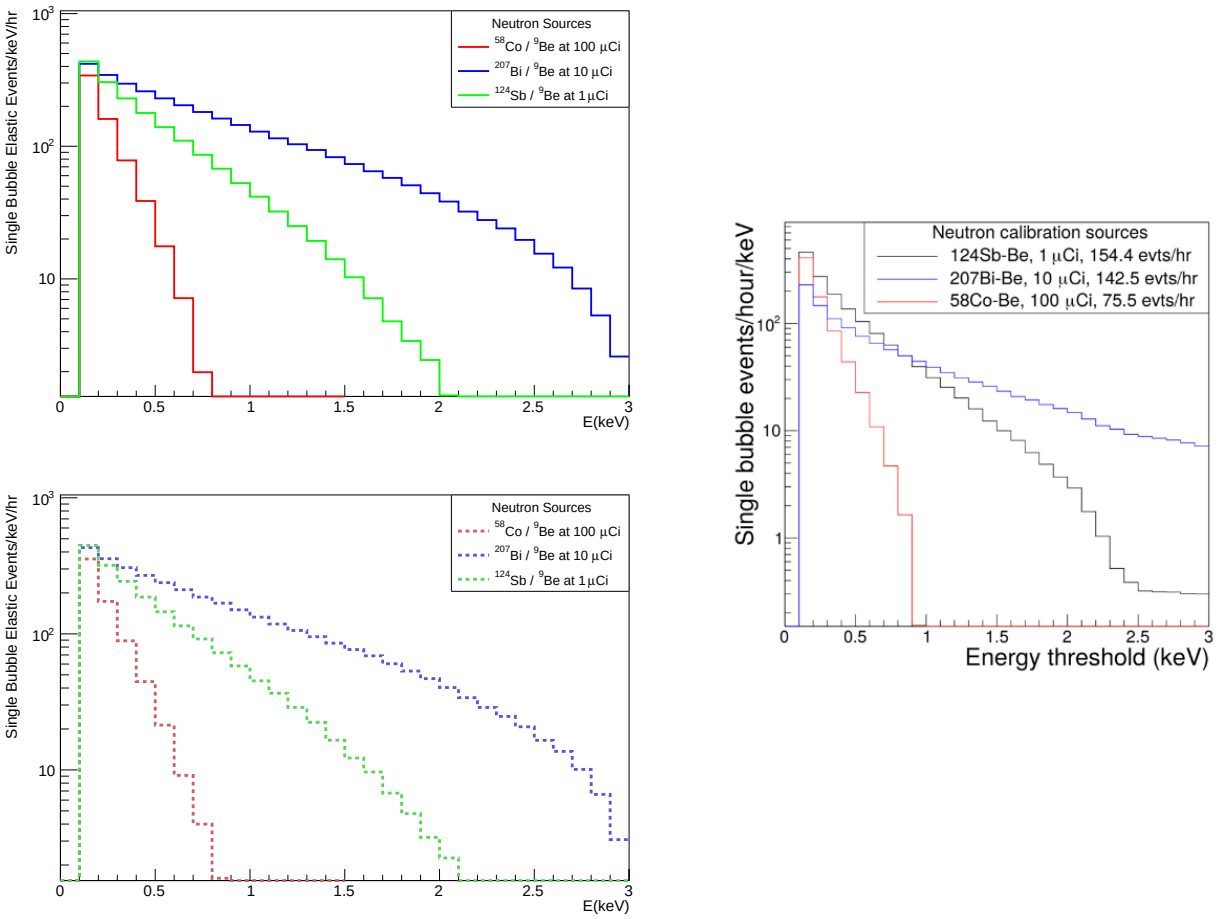

Figure 31: Energy Spectrum Histograms for Single Bubble Event Rate for Elastic Only Nucleus Recoils for all radioisotope-neutron sources given all simulation schemes. Top Left: Angular Bias. Bottom Left: Isotropic Emission. Right: E. Alfonso simulations [18].

In this comparison, a similar performance and behaviour is observed. However, when examining the ^{124}Sb source, it becomes evident that the rates diminish more rapidly in the neutron generator compared to E. Alfonso's simulations. This discrepancy could stem from either insufficient statistical data on our part or an underestimation of events in the high channel by E. Alfonso's simulations. Nevertheless, the overall rates remain consistent across all simulation schemes. Enhancing identification accuracy requires conducting further practical tests. To refine our analysis, we introduce a pivotal metric in Appendix E that evaluates simulation performance by comparing the ratios of doubles/multiples to singles events per energy alongside practical results. This additional metric offers a comprehensive assessment of the simulation's effectiveness.

With this, we conclude the analysis section. While we eagerly await experimental data, it is imperative to continue our analysis to substantiate future physics detections. The thorough exploration of our simulations outcomes has provided valuable insights into the expected calibration strategy, enhancing our understanding and enlisting for further research. I strongly encourage readers to delve into the Appendices, where they will find comprehensive information supporting our findings. Notably, practical plots crucial for proper argon-neutron identification events, offering indispensable visual aids to complement the analysis.

6 Conclusions

The examination of the SBC-LAr10 detector has provided valuable insights into low-energy nuclear recoil thresholds, particularly within the context of potential WIMP-like interactions. The focus of this study was to critically assess the theoretical detection capabilities of the detector.

To achieve this, we employed two simulation approaches to generate nearly mono-energetic neutrons through a photonuclear reaction, primarily for calibration purposes. The comprehensive investigation of the $^{9}\mathrm{Be}(\gamma, n)^{8}\mathrm{Be}$ reaction, coupled with the implementation of GEANT4 neutron scattering simulations, allowed us to precisely characterize nucleus recoil energy distributions and event rates. This achievement was made possible through the development of a neutron GEANT4 macro-generator, introducing a valuable tool for accurate neutron parameter generation. The simulations, in combination with their isotropic angular distribution counterparts, introduced features for the detector simulation, particularly in identifying low-energy threshold events. The dataset enabled effective discrimination among various interaction types.

Notably, we observed a significant concentration of events within the $^{36}\mathrm{Ar}$ channel, with a reported average close to 10%, notably higher than the expected 1%. Further analysis is warranted to explore potential resonances in the reaction cross-section at the simulated energies. Additionally, the thermal capture of neutrons in $^{36}\mathrm{Ar}$ may give rise to potential nucleation events within the energy range of 0.5 keV to 1.2 keV, necessitating careful consideration for practical applications and future research endeavors.

Furthermore, a compelling trend emerged, highlighting the preference for thermal neutron capture in $^{40}\mathrm{Ar}$ as the primary reaction channel for low-energy neutron sources. This characteristic could warrant further exploration as a potential calibration technique, given the accompanying photon emissions during the capture process, although in-depth analysis exceeds the scope of this work.

The nucleus recoil energy event rates for the selected neutron sources were reported for elastic scatterings ($^{40}\mathrm{Ar}$, $^{36}\mathrm{Ar}$, and $^{38}\mathrm{Ar}$), indicating a concentration of events at 0.2 keV. The simulation schemes presented similar results with minor differences, particularly in terms of the points of interaction, where no distinct zone preferences were observed.

It's worth emphasizing that the behavior of the two simulation schemes demonstrated remarkable similarity, with no significant disparities observed. However, the isotropic case exhibited a higher interaction rate, attributed to the angular dependency on the energy distribution, resulting in more events simulated at higher energies compared to the angular bias scheme.

In summary, this study serves as a foundation for probing nucleation events at energies near the desired threshold, based on the theory of photonuclear reactions for neutron production and the geometrical characteristics of GEANT4 SBC. These diverse interactions offer promising avenues for calibration techniques and future applications.

As we move forward, we eagerly await the results and construction progress of the SBC, anticipating the opportunity for further analysis and validation of the findings uncovered during this investigation.

A Radioisotope Photon Flux Calculation

The activity rate for a specific gamma-emitting radioactive isotope can be calculated by:

$$R = \log(2)\frac{N}{t_{1/2}}, \tag{A.1}$$

where N is the number of radioactive atoms and $t_{1/2}$ is the half life time of the radioisotope. N can be calculated by the following formula

$$N = \frac{N_A}{A} \times \rho \times V, \tag{A.2}$$

where N_A is Avogadro constant, A is the atomic weight of the isotope, ρ and V are, respectively, the density and volume of the source. Simplifying, $V \times \rho$ is the mass of the source, hence, to find the activity by unit mass, we can express the rate by mass unit and find that the specific activity for any source is:

$$a[\text{Bq/g}] = \log(2)\frac{N_A}{A \times t_{1/2}} \tag{A.3}$$

The previous formula was used to obtain column 3 of Table 4. Due to the fixed probability of radioactive decay for a particular radionuclide over a defined time interval (with minor exceptions as outlined in changing decay rates), the quantity of decays taking place in a specific mass (and consequently a precise number of atoms) of that radionuclide during a set period remains constant, disregarding statistical variations.

It is important to note the calculated activity rate in other relevant units, in specific, μCi. The Curie is a unit of measurement for radioactivity defined as the amount of a radioactive substance that undergoes 3.7 x 10^10 disintegration's per second. In the International System of Units (SI), the becquerel (Bq) is the standard unit for radioactivity, where 1 Curie is equal to approximately 3.7 x 10^{10} becquerels. This information will become relevant in upcoming discussions.

Source	Specific Activity (μCi/g)
^{58}Co	1.4052×10^6
^{124}Sb *low*	7.5933×10^6
^{124}Sb *high*	7.5933×10^6
^{207}Bi	2.3764×10^4

Table 13: Specific activity rate in μCi for ^{58}Co, ^{124}Sb, and ^{207}Bi sources.

Now, in the fourth column in Table 3, a Neutron Rate is presented, this is considered for a δx thick sheet of beryllium, and in no way should it be used for SBC simulations. SBC's calibration chamber geometry is not considered for this production rate, hence, the reported data can only be taken as an estimate of the rate capacities. The formula used for the neutron production rate is:

$$r = a \times g \times \rho_A \times \sigma_{\text{PN}} \times BR \times \delta x \tag{A.4}$$

where a is the specific activity of the source and g its mass, ρ_A is the nuclei density for beryllium-9, σ_{PN} is the photonuclear cross-section for the desired radioisotope photon energy,

BR the branching ratio of the reaction and δx is an infinitely small thick layer of beryllium. Let us do the following observation: $a \times g$ is just R, the photon flux from the radioisotope source, also, $\sigma_{\mathrm{PN}} \times BR$ is the yield of the reaction. Equation A.4 was used for calculating an approximate neutron rate per cm/g unit. For a comprehensive and precise neutron rate calculation specific to the SBC calibration chamber geometry, we recommend consulting Appendix C.

B Updated GEANT4 Libraries for Photo-Nuclear Calibration

As mentioned in section 5.1, this library updates interactions between the neutrons produced in a photonuclear reaction and the detector's target material. GEANT4 depends on models, theoretical calculations, and experimental data for their simulations. Neutron interactions with nuclei information are sampled from experimental data. Hence, processes like capture, elastic and inelastic scatterings, isotope production, and fission are all taken from experimental libraries.

This libraries are found in the *share/Geant4-10.3.3/data* section withing GEANT4. Inside this, there is a variety of compilation of libraries, each corresponding to different experimental data of particle interactions. The one concerning neutron interaction with nucleus is the **G4NDL** libraries. The primary source of G4NDL data is the ENDF/B-VI(VII since NDL3.15) library, which is overseen by the Cross Section Evaluation Working Group (CSEWG). You can find the original data files on the National Nuclear Data Center webpage: http://www.nndc.bnl.gov/csewg/.

Additionally, G4NDL data is also derived from the JENDL library, managed by the Nuclear Data Evaluation Center of the Japan Atomic Energy Agency. The original data files for JENDL can be accessed through the Japanese Evaluated Nuclear Data Library webpage: http://www.ndc.tokai-sc.jaea.go.jp/jendl/jendl.html.

G4NDL data can be updated by following the next steps:

1. Download either: JEFF-3.3, ENDF/B-VIII.0, BROND-3.1 or JENDL-4.0 in https://www-nds.iaea.org/geant4/ and decompress it.
2. Download Robinson A. updated Elastic libraries (contact alan.robinson@umontreal.ca for reference) and copy the files in the Elastic directory into the previously downloaded libraries. (Making sure to replace the data).
3. Move the new updated libraries to *path/to/geant4.10.03.p03/share/Geant4-10.3.3/data/*.
4. Head over to */bin/* directory and open *geant.sh* file.
5. Comment the line

```
$ export G4NEUTRONHPDATA="`cd $geant4_envbindir/..
        /share/Geant4-10.3.3/data/G4NDL4.5 >/dev/null ;pwd`"
```

and replace it by:

```
$ export G4NEUTRONHPDATA="`cd $geant4_envbindir/..
        /share/Geant4-10.3.3/data/ENDF-VIII.0/JEFF-3.3/BROND3.1
        /JENDL-4.0 >/dev/null ;pwd`"
```

where you choose from ENDF-VIII.0, JEFF-3.3, BROND3.1 or JENDL-4.0. After this is done, source the geant4.sh file. This should update the neutron interactions, when running a macro, the prompt will tell you the direction of where GEANT4 is compiling its neutron data. This will allow for more accurate neutron-Argon elastic interactions at low energies.

C Simulation Neutron Production Rate Calculation

This derivation is motivated by [63] and applies it for a similar problem with production rates. The neutron production rate due to a δx of beryllium is

$$r = \Phi \times \rho_A \times \sigma_{\mathrm{PN}} \times \delta x \tag{C.1}$$

where, Φ is the gamma flux coming from the radioisotope disk[1], ρ_A is the nuclei density of beryllium in a δx and σ is the photonuclear cross-section. Given the geometry of the beryllium block and radioisotope disk, we can calculate the the photon-flux: For a surrounded cylindrical block of beryllium, the flux can be seen as an surface integral:

$$\Phi \times \delta x = \int_V \vec{F} \cdot \hat{n} dV \tag{C.2}$$

where dV is the standard cylindrical Jacobian $\rho d\rho d\phi dz$ and $\vec{F}$ is the number density of photons at a distance r at a rate R and

$$\vec{F} = \frac{R}{4\pi r^2}\hat{r} \tag{C.3}$$

This flux is radially emitted. r is parameterized by cylindrical coordinates as $r^2 = \rho^2 + z^2$, thus, the integral to solve becomes

$$\Phi \times \delta x = \int_0^{2\pi} \int_0^a \int_{z_i}^{z_f} \frac{R}{4\pi(\rho^2 + z^2)} \rho dz d\rho d\phi \tag{C.4}$$

The integral in ϕ is trivial and independent of the integrant, thus

$$\Phi \times \delta x = \frac{R}{2} \int_0^a \int_{z_i}^{z_f} \frac{\rho}{\rho^2 + z^2} dz d\rho \tag{C.5}$$

This integral is a well known (from electrodynamics) and as analytical solutions. This are the following:

$$\begin{aligned} \Phi \times \delta x \left(\frac{4}{R}\right) = &-z_{\mathrm{i}} \log\left(z_{\mathrm{i}}^2 + a^2\right) + 2a \arctan\left(\frac{z_{\mathrm{i}}}{a}\right) - 2z_{\mathrm{i}} \log\left(z_{\mathrm{i}}\right) \\ &- z_{\mathrm{f}} \log\left(z_{\mathrm{f}}^2 + a^2\right) - 2a \arctan\left(\frac{z_{\mathrm{f}}}{a}\right) + 2z_{\mathrm{f}} \log\left(z_{\mathrm{f}}\right) \end{aligned} \tag{C.6}$$

Using the beryllium block geometry: $a = 2.38$ cm, $z_f = 3.81$ cm and $z_i = -3.81$ cm. Substituting this values in C.6 we have that:

$$\Phi \times \delta x = 0.92525 \text{ cm} \times R \tag{C.7}$$

where R is dependent on the density and dimensions of the radioisotopes. Thus, the neutron production rate is

$$r = R \times 0.923535 \text{ cm} \times \sigma_{\mathrm{PN}}(E_\gamma) \times BR \times \rho_A \tag{C.8}$$

where, R is the gamma flux, $\sigma_{\mathrm{PN}}(E_\gamma)$ is the photonuclear cross-section evaluated at the corresponding radioisotope photon-energy E_γ, BR is the branching ratio of the corresponding E_γ photon emission and ρ_A the nuclei density of beryllium-9.

[1] As a first point of approximation we shall consider an isotropic point-like flux inside the beryllium block.

The only unknown variable in this equation is now the gamma flux. As mentioned in section 5.3.1, in theory, one could use the calculations presented in Appendix A for the gamma flux. However, using a rate of the presented orders, as reported in Table 4, one ends up with thousands of events every second in the detector. As SBC's technical report states in [33], the time required for the detector to return to a super-heated fluid state is in the order of a couple of seconds. Hence, while the theoretical specific activity of the source are right, it will be useful to find a flux that would create a realistic rate of detection. For this, we will utilize the detector's geometry efficiency reported in Equation 5.7 and solve for R in Equation C.8:

$$R = \frac{r \times \epsilon_{\text{geo}}^{\text{MC}}}{0.923535 \text{ cm} \times \sigma_{\text{PN}}(E_\gamma) \times BR \times \rho_A} \tag{C.9}$$

where $r \times \epsilon_{\text{geo}}^{\text{MC}}$ is the rate of interaction in the detector. Utilizing the detector's geometric efficiency found in Table 9, and trying to fix the value for just a couple of events per seconds in the detector. The chosen rates are reported in Table 7.

D Multiples to Singles Ratios

The ratio of multiples to singles, in practical applications, as illustrated in Table 9, is ideally kept low. To observe this performance in terms of the integrated nucleus recoil probability function, we conducted a subtraction of Figure 29 from Figure 24 and subsequently divided the result by Figure 29. This statistical calculation was also performed in preliminary simulations following E. Alfonso's scheme, allowing for a comparative evaluation. In order to achieve this, we shall present both the full and the elastic-only single bubble ratios, considering E. Alfonso's considerations. The calculated ratios of multiples and doubles to singles are shown below:

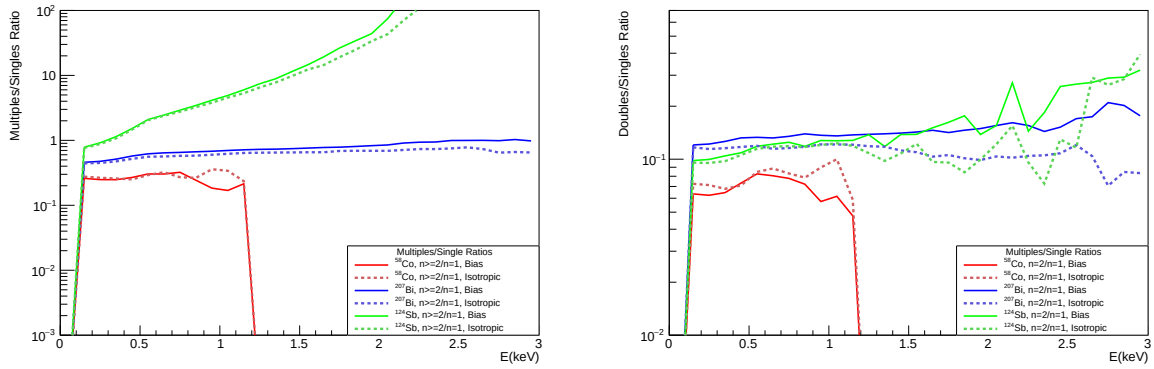

Figure 32: Multiple and Double to Single Event Ratio for Nucleus Recoils for all radioisotope-neutron sources given all simulation schemes. Left: Multiple to Single Ratio. Right: Double to Single Ratio.

As evident from the trend, Figure 32 showcases a lack of variation across the simulation schemes within the neutron generator. We can observe the following key characteristics:

- Regarding the ^{58}Co source, a consistently low ratio is observed across all interactions, notably going to 0 surpassing 1 keV. This dip is attributed to an excess of events around this energy range, primarily resulting from neutron capture. In the elastic case, the ratio aligns with the anticipated elastic scattering limit, suggesting that events near this threshold predominantly involve single bubble occurrences.
- Analyzing the behavior of the ^{207}Bi source, a steady and unwavering ratio is maintained within the plotted energy range. This stability is intriguing, indicating a persistent probability of single bubble events across the entire spectrum explored.
- In the context of the ^{124}Sb source, a noticeable surge in the ratio is observed above 2 keV, signifying an increased likelihood of multiple interactions beyond this energy level. This surge can be attributed to the comparatively *high* branching ratio of ^{124}Sb. As outlined in Table 4, the maximum elastic energy for the *low* channel is near 2 keV, consistent with the rapid growth observed above this energy. As discussed in preceding sections, the majority of multiple events originating from the ^{124}Sb source are predominantly attributed to this channel. Examining the ratio across all events reveals an exponential increase, indicating that numerous single interaction events stem from neutron capture. It is essential to explore identification and discrimination

techniques to address this trend. Furthermore, an important aspect is that in the case of the higher branching ratio, although the detection rate is low, the temporal element is not factored in when calculating the ratio. Consequently, this contributes to the prevalence of these preferences beyond the *low* nucleus recoil threshold.

To align with previous simulations, a focused comparison can be made by plotting the ratios of multiple to single and double to single events specifically within the elastic case. This targeted analysis aims to showcase the variations between E. Alfonso's findings and our own results, providing a clearer understanding of the discrepancies or similarities in this specific scenario.

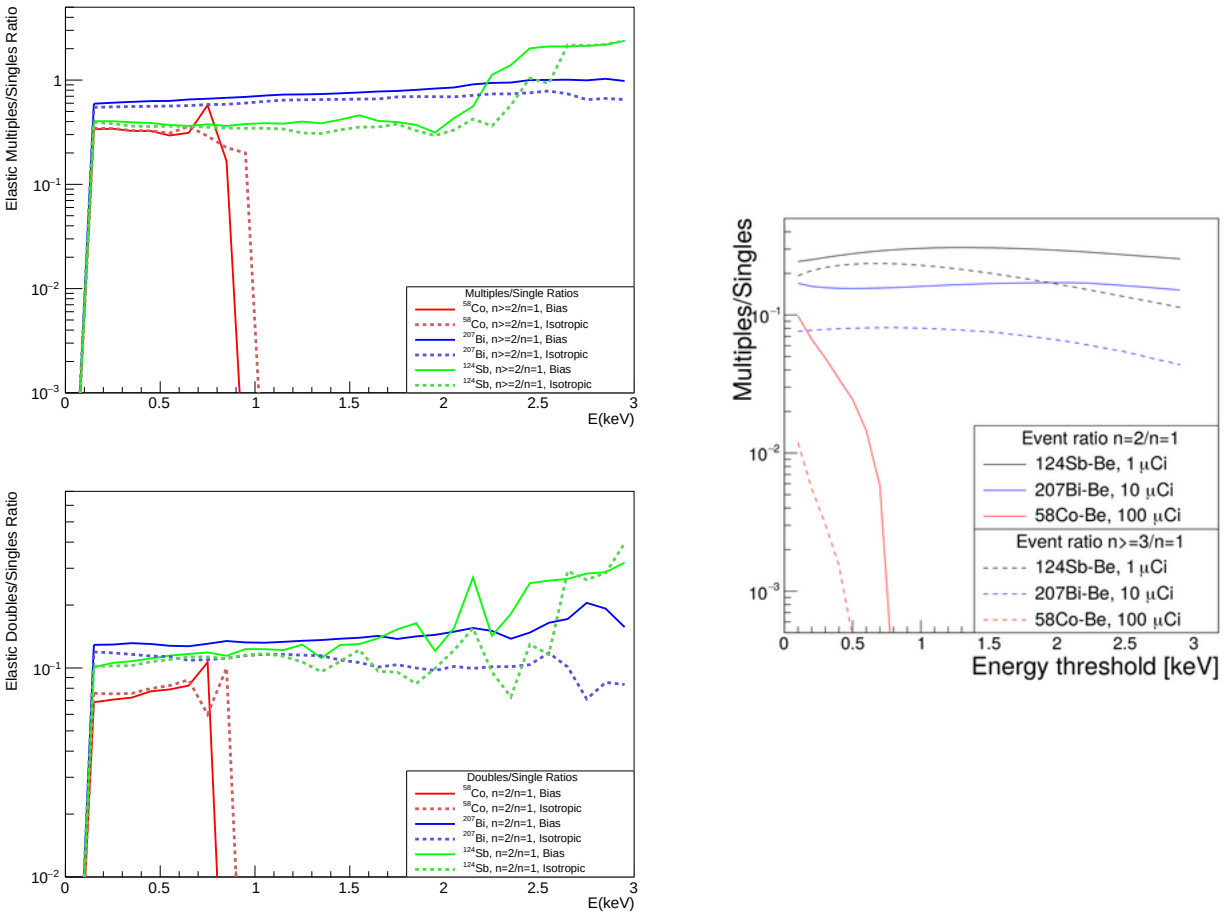

Figure 33: Multiple and Double to Single Event Ratio for Nucleus Recoils for all radioisotope-neutron sources given all simulation schemes. Left: Multiple to Single Ratio. Left: Double to Single Ratio.

Conclusions across both simulations are the following. The comparison shown in Figure 33, suggest the possibility that the analysis performed by E. Alfonso's simulations may have underestimated the *high* channel due to issues related to improper normalization or overlooked simulation considerations. Concerning the differences observed in the ^{58}Co source, it's likely that these variations arise from the simulation's neutron energy range. Given the emission parameters, more neutrons at lower energy rates may be generated in the source than accounted for in E. Alfonso's scheme. As for ^{207}Bi, it performs similarly across all three

schemes. It does however feature a smaller ratio for all sources, this has to be kept in mind since E. Alfonso ratios involve double and triples or more ratios. A thorough examination of the simulation parameters used in this specific scenario should offer insights into the reasons for these discrepancies.

In practical terms, this ratio serves as a valuable tool for comparing our simulations with real-world observations. It allows us to assess and verify the accuracy of our simulation's behavior against practical data.

E Analysis: Plots for All Sources and Simulation Schemes

Left: Angular Bias *Right: Isotropic Emission*

^{58}Co Neutron Parameters

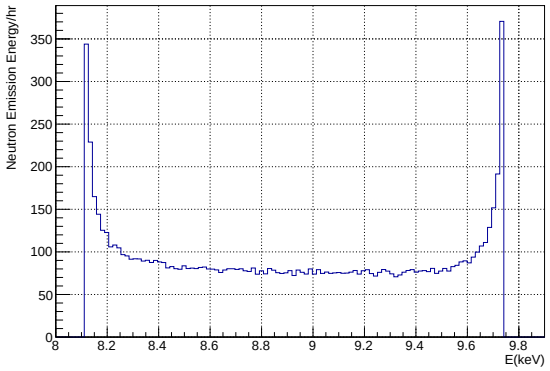

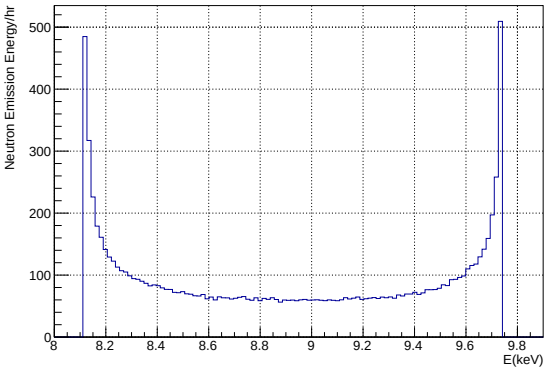

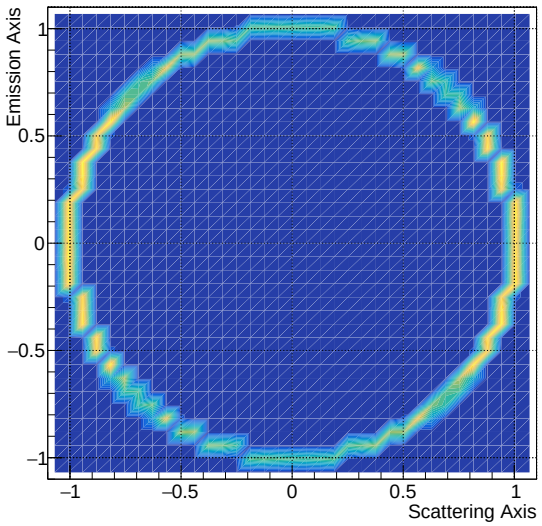

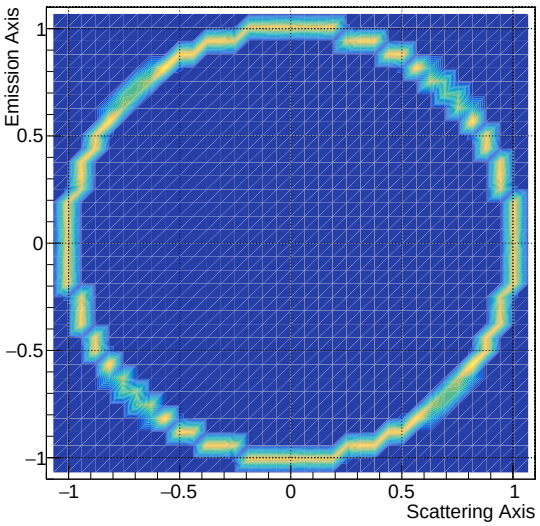

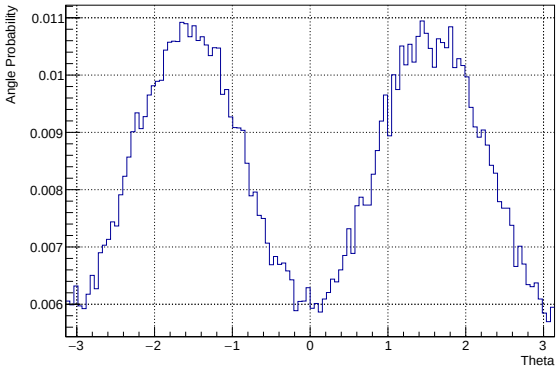

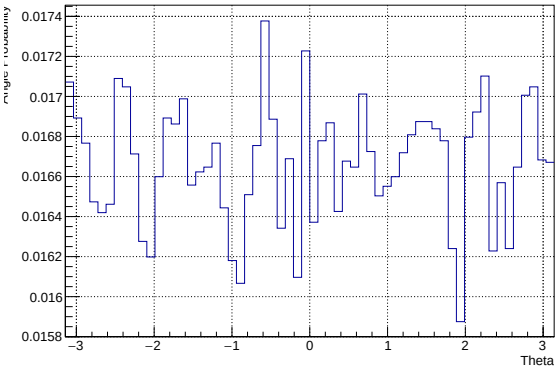

^{124}Sb - *low* Neutron Parameters

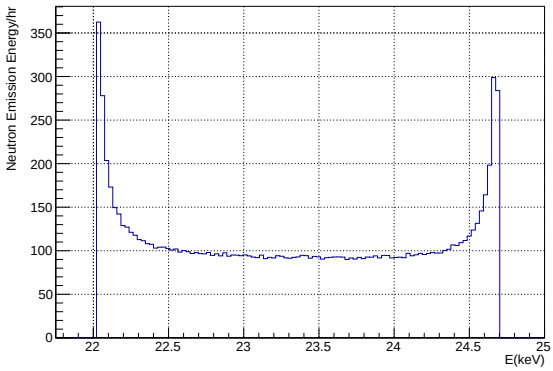

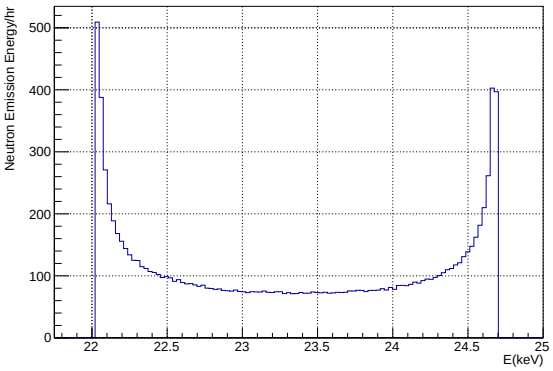

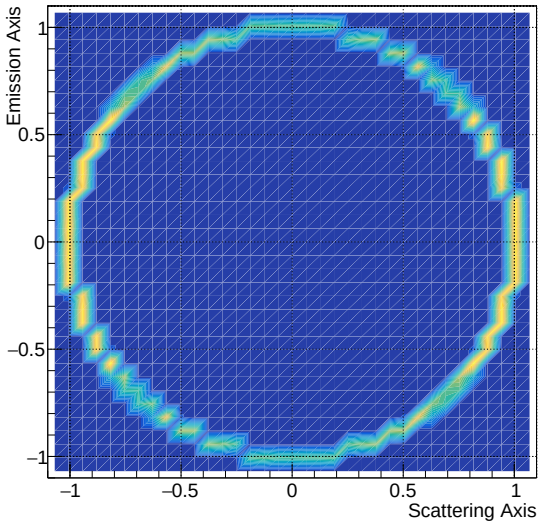

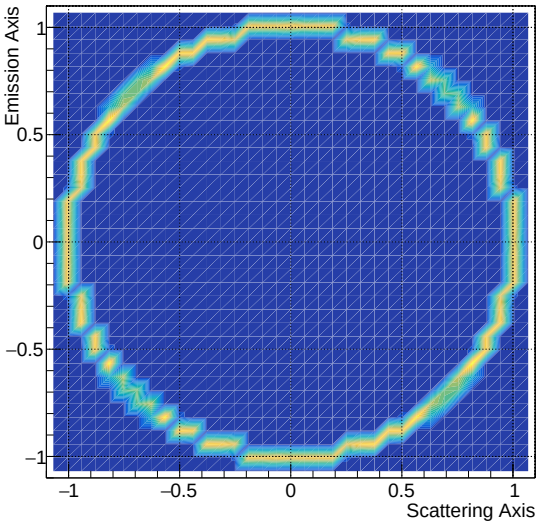

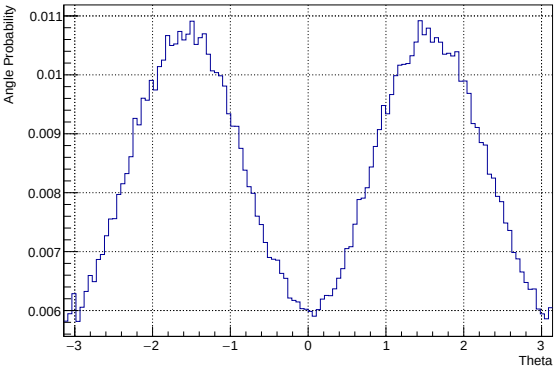

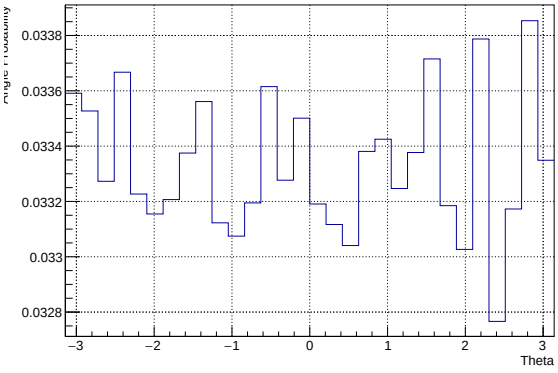

^{124}Sb - *high* Neutron Parameters

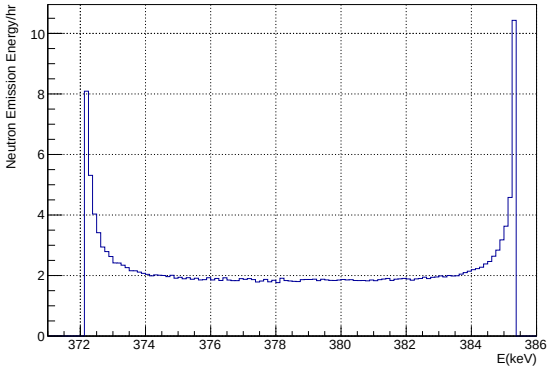

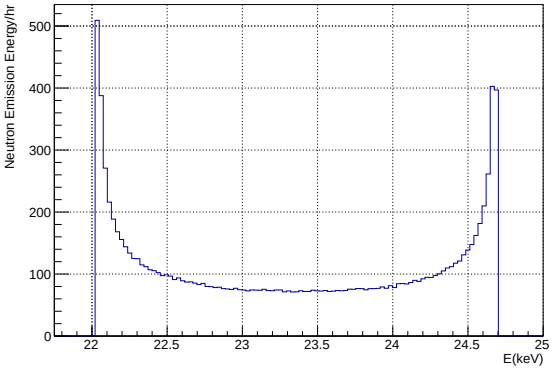

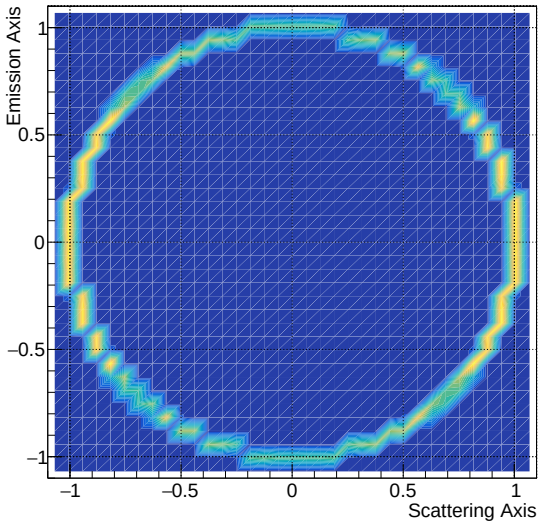

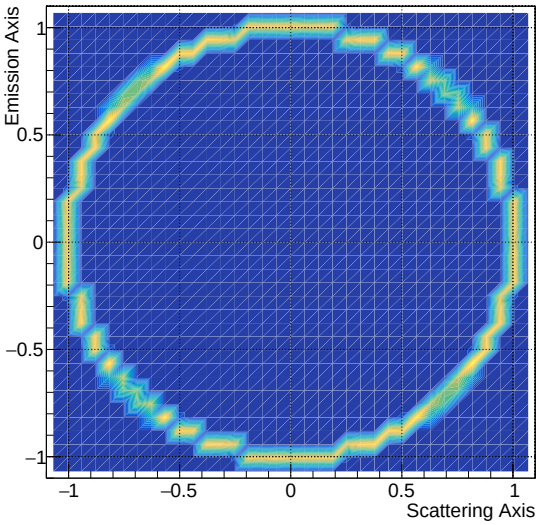

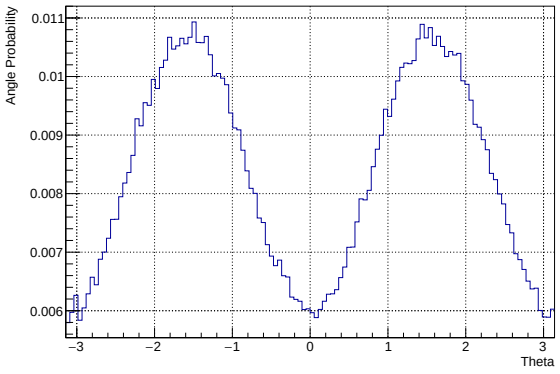

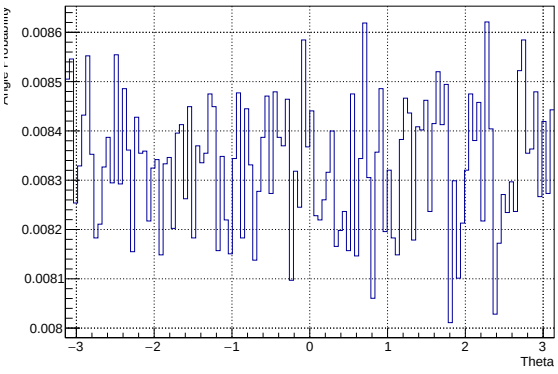

^{207}Bi Neutron Parameters

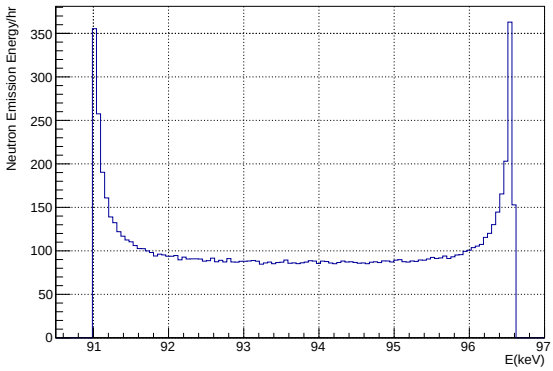

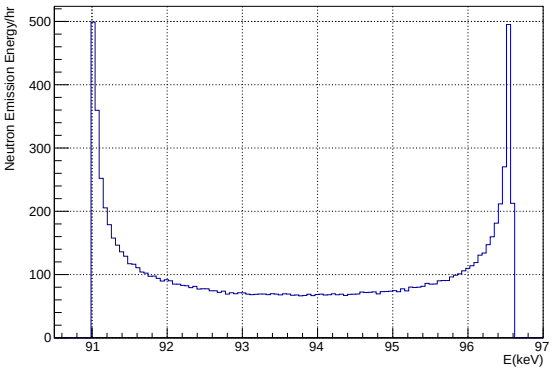

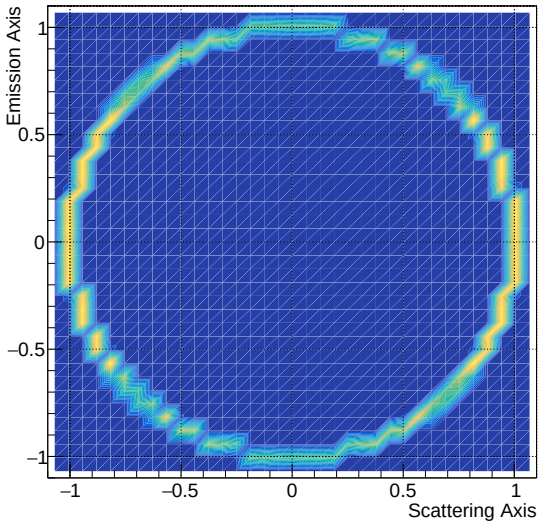

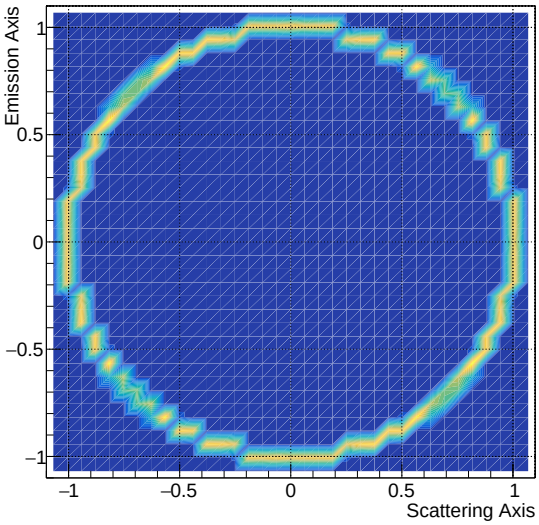

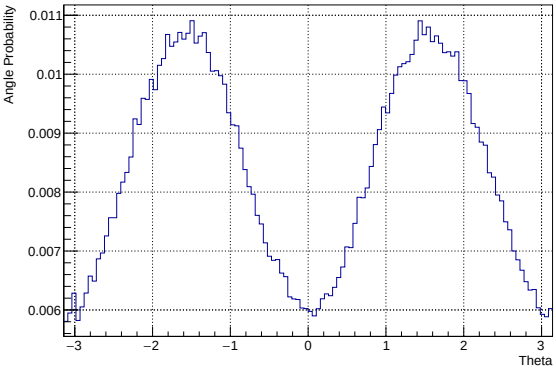

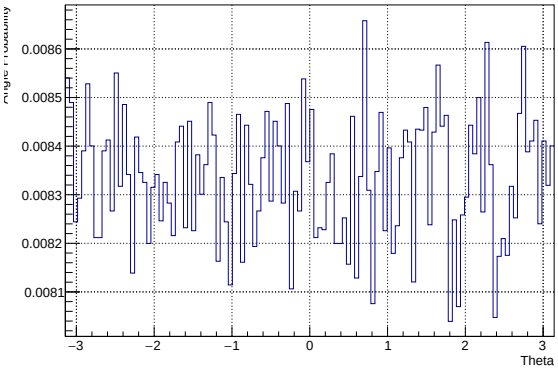

Event Multiplicities

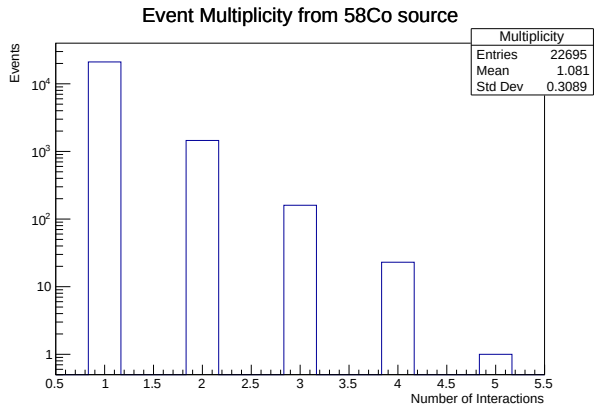

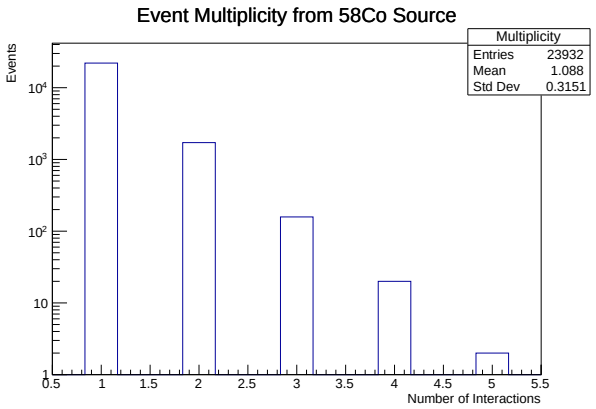

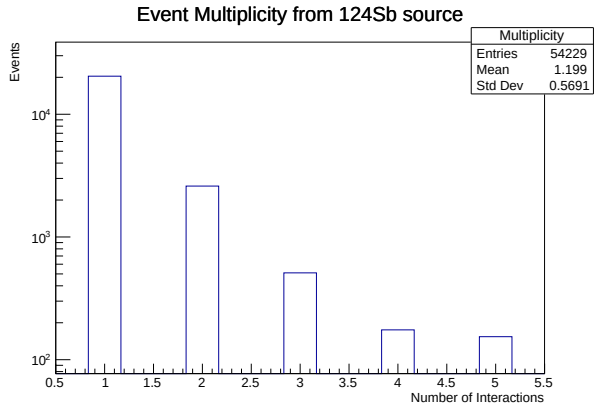

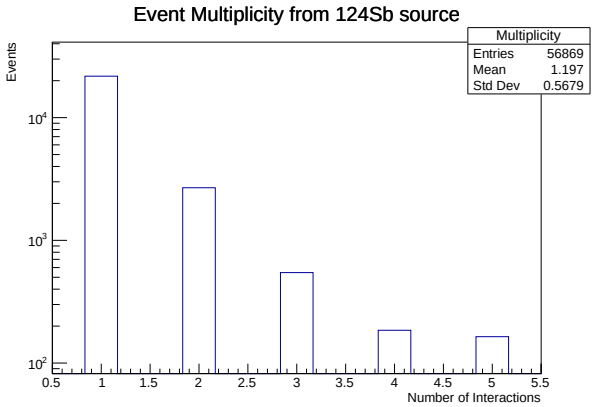

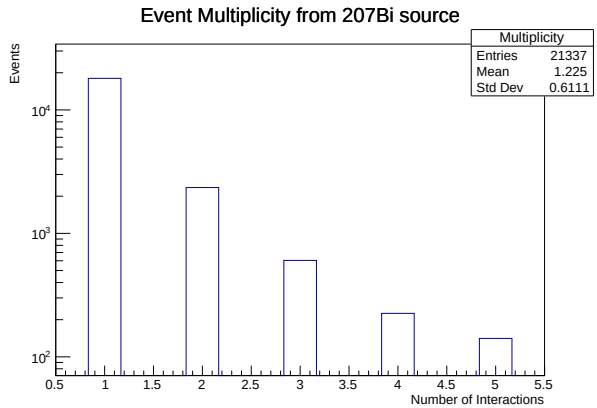

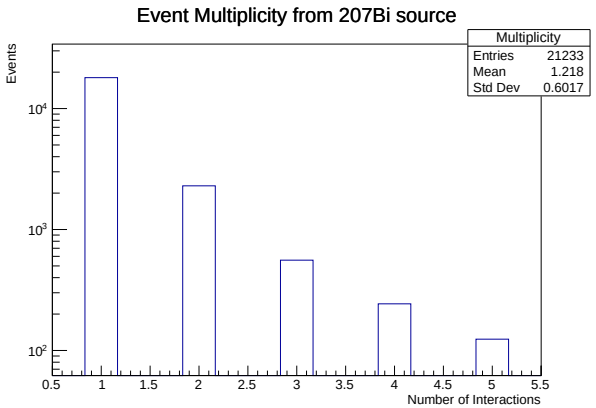

Isotope Interactions

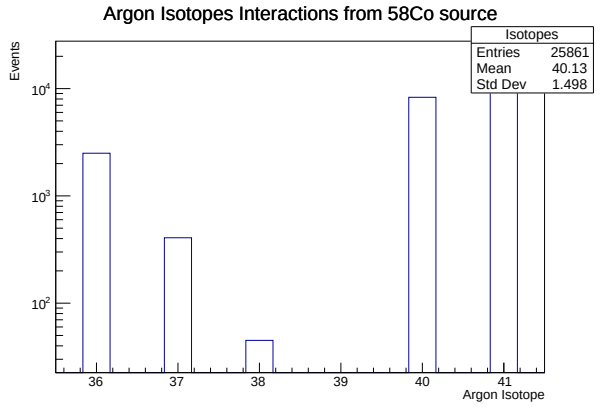

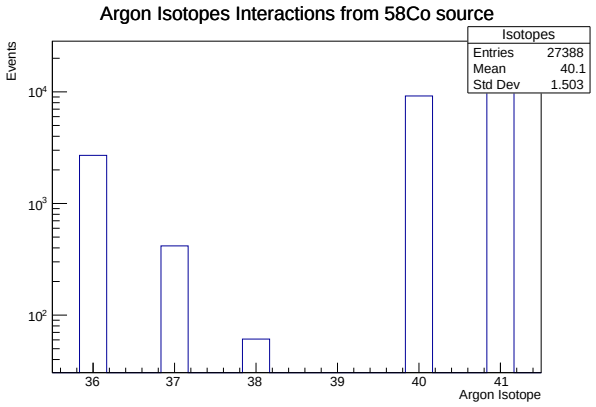

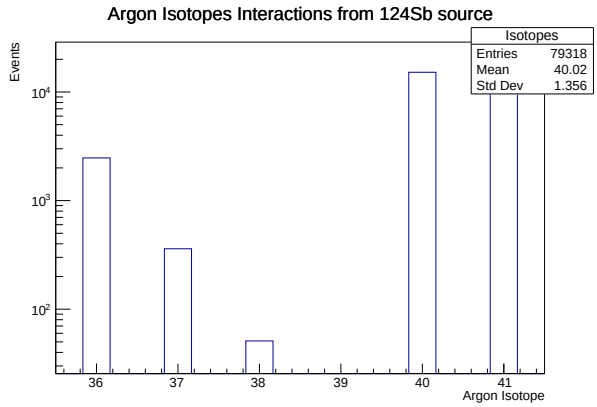

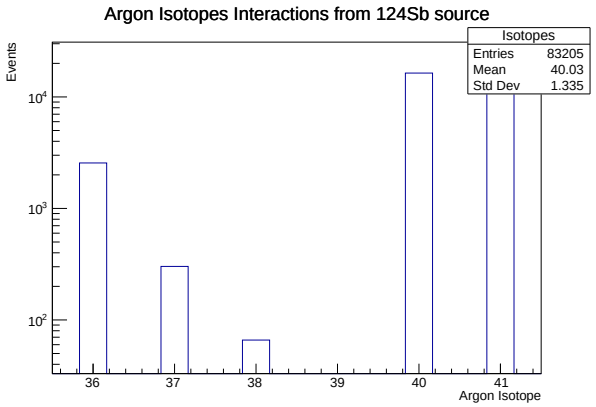

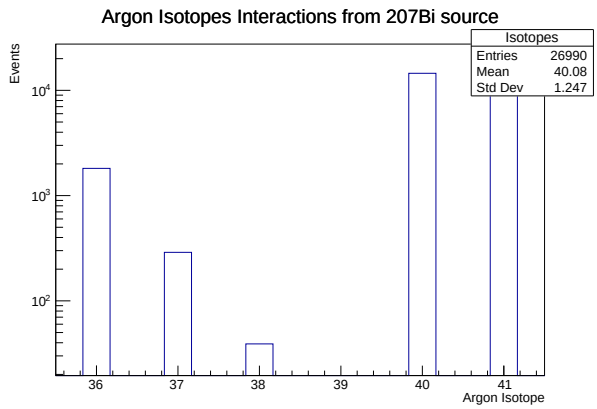

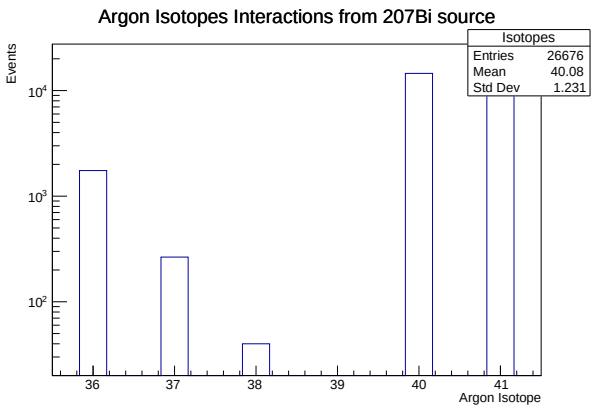

Point of Interactions

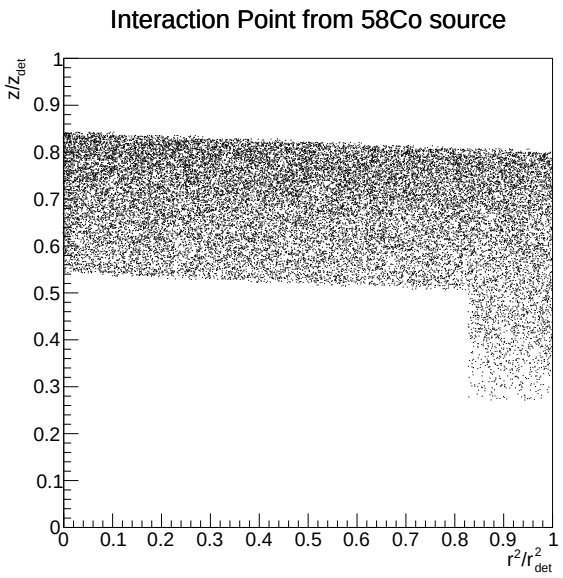

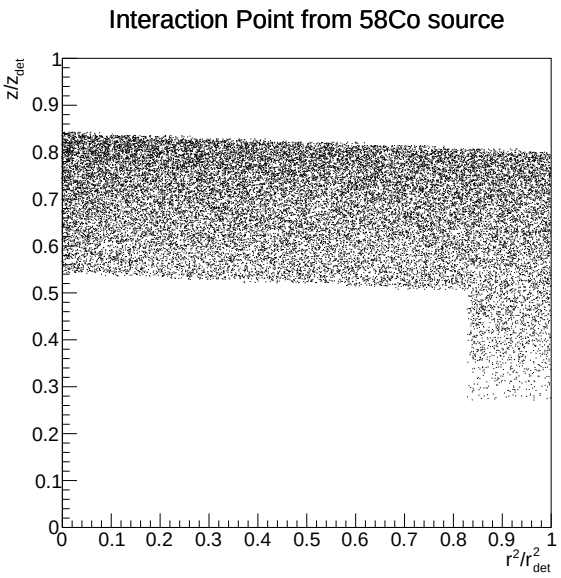

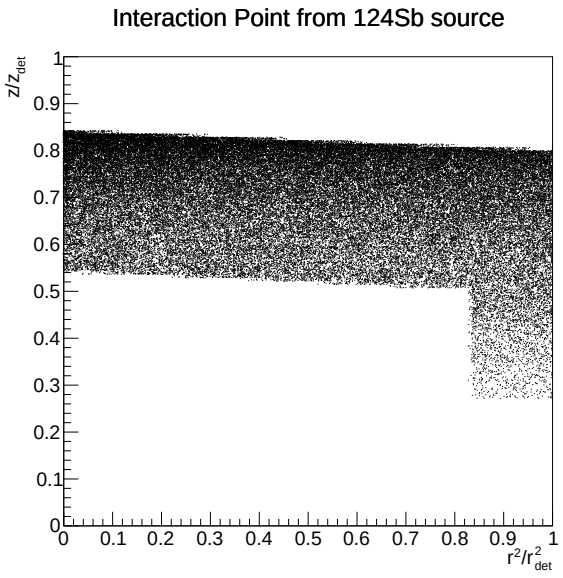

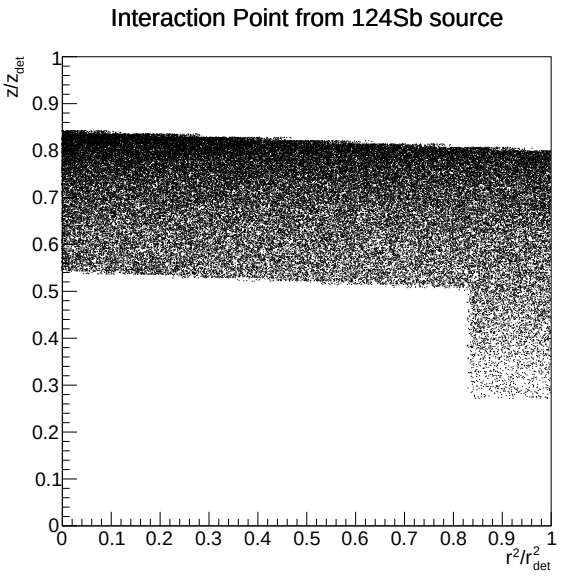

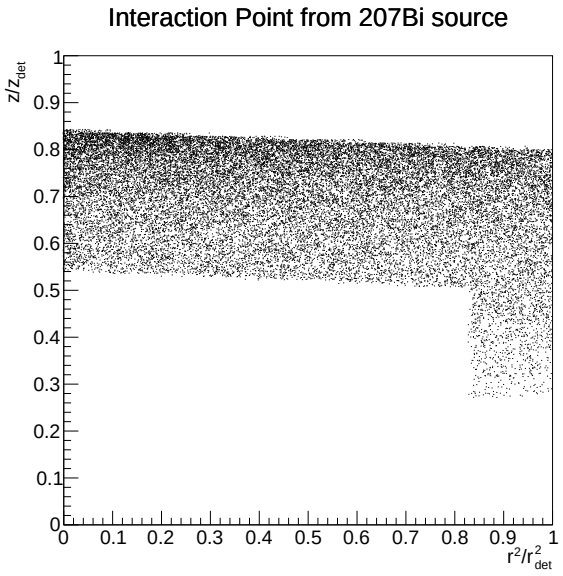

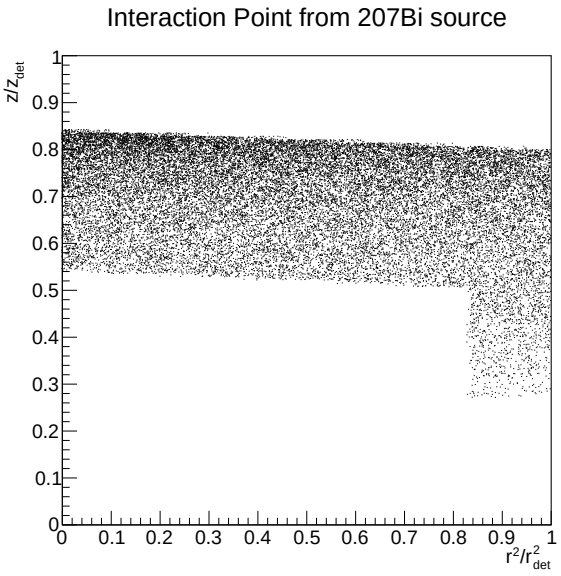

Elastic vs. Capture Position

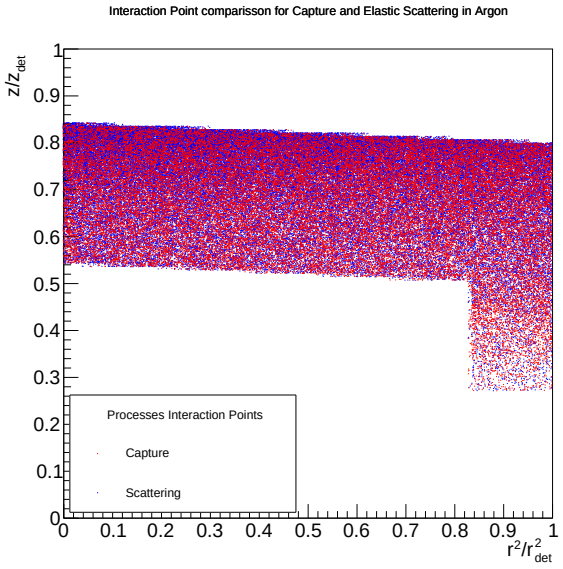

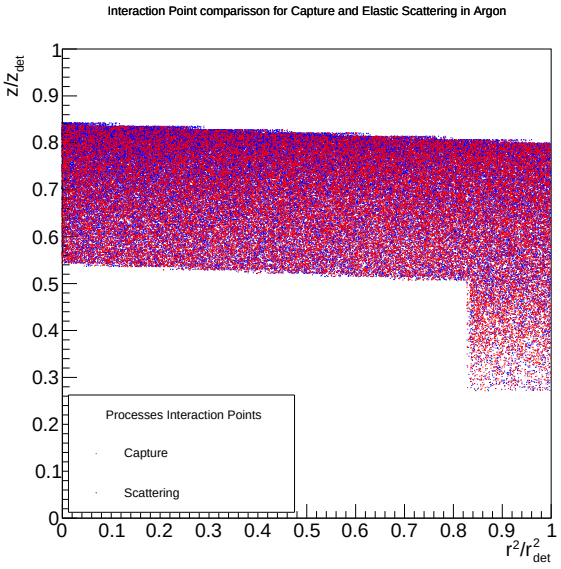

Capture Events Nucleus Recoil Energy Rate Distribution

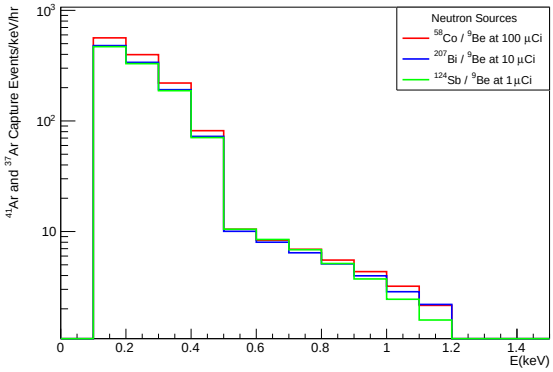

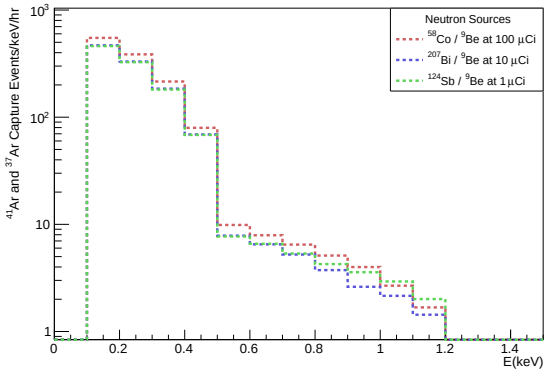

^{41}Ar Events Nucleus Recoil Energy Rate Distribution

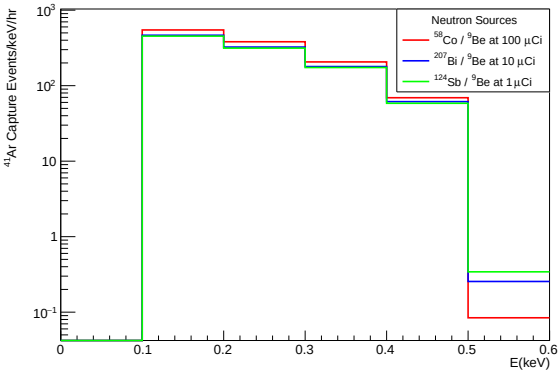

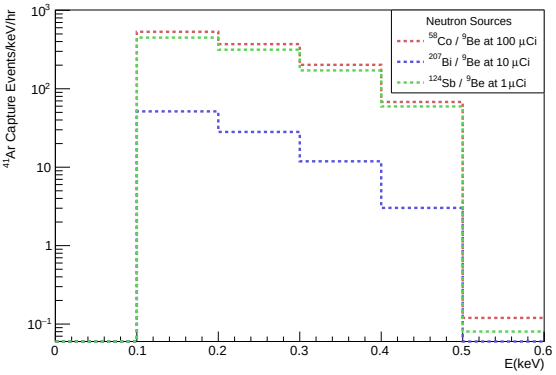

^{37}Ar Events Nucleus Recoil Energy Rate Distribution

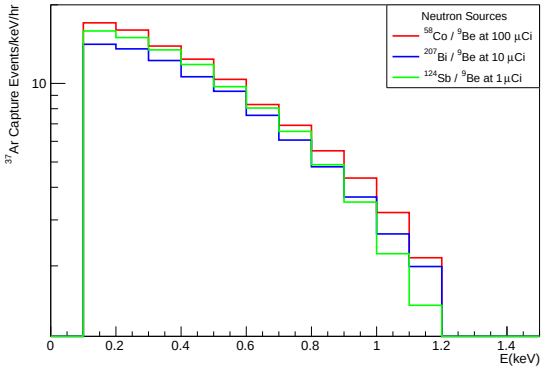

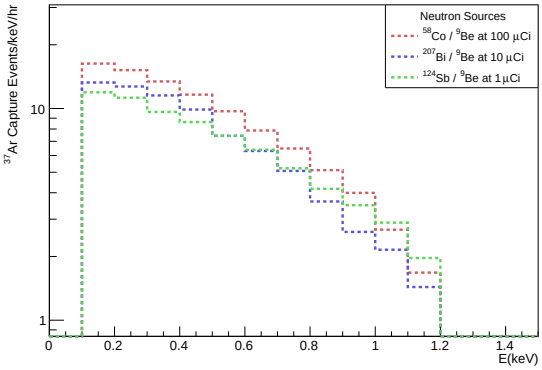

Elastic Events Nucleus Recoil Energy Rate Distribution

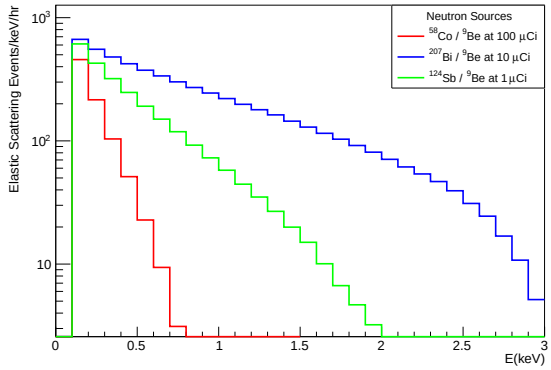

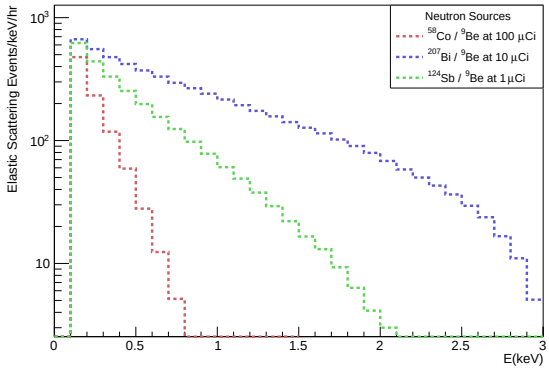

^{40}Ar Events Nucleus Recoil Energy Rate Distribution

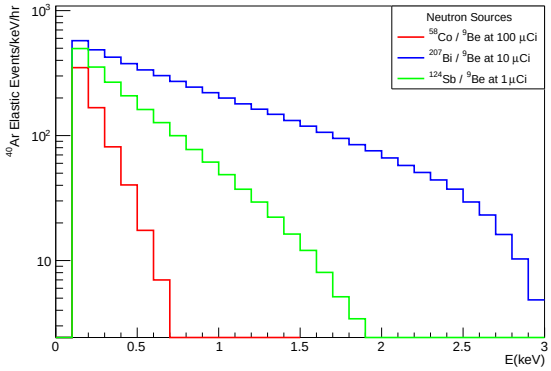

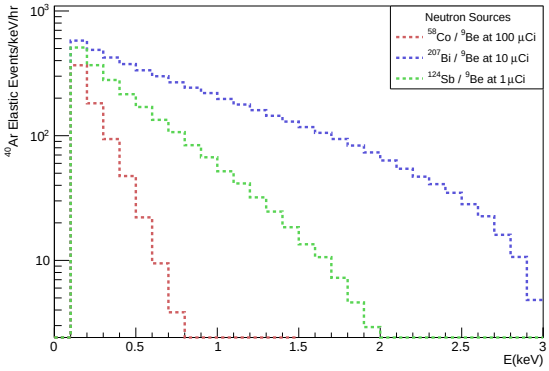

^{36}Ar and ^{38}Ar Events Nucleus Recoil Energy Rate Distribution

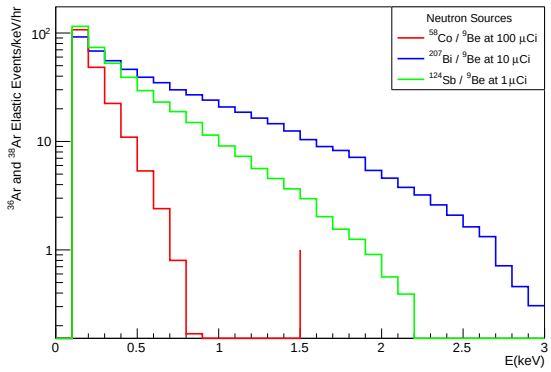

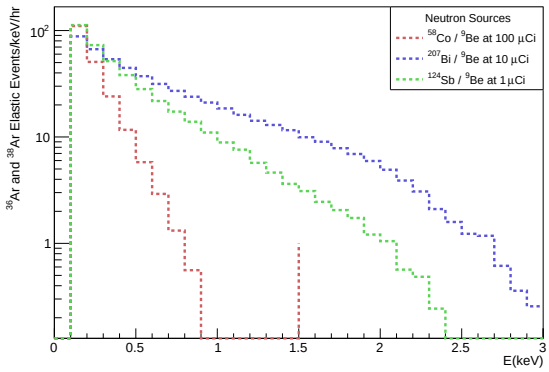

Single Bubble Capture Events Nucleus Recoil Energy Rate Distribution

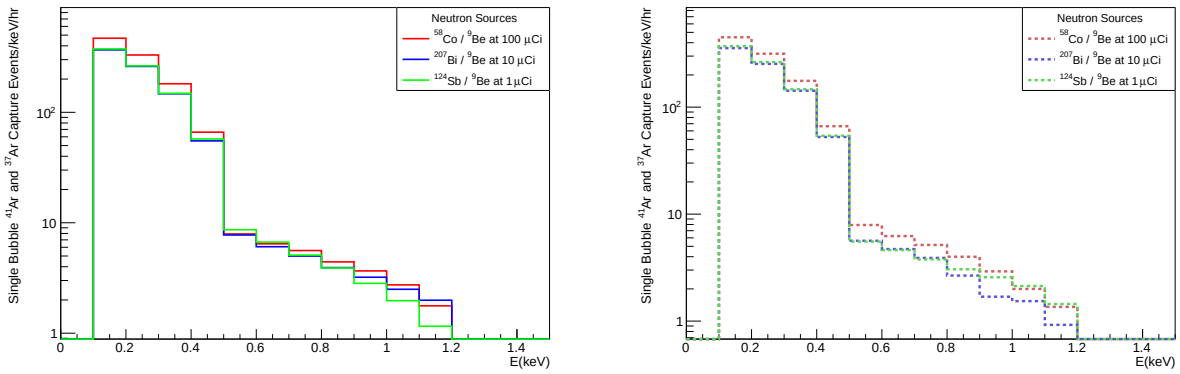

Single Bubble ^{41}Ar Events Nucleus Recoil Energy Rate Distribution

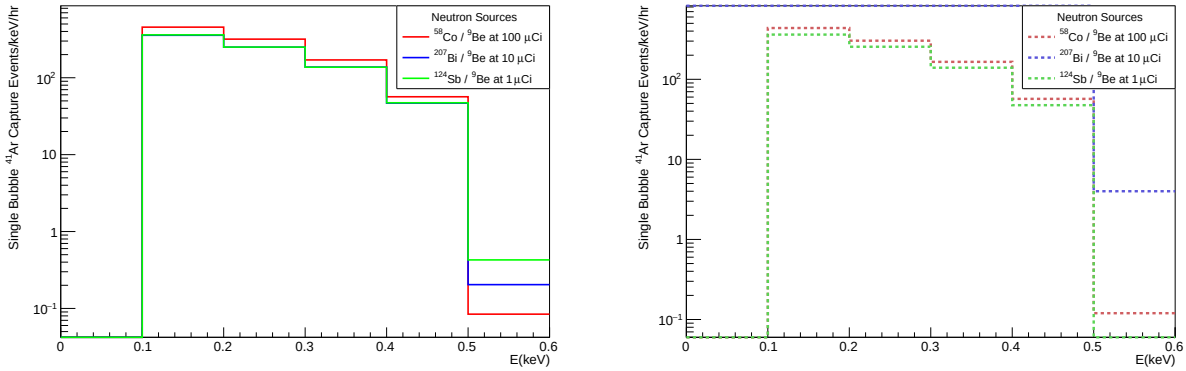

Single Bubble ^{37}Ar Events Nucleus Recoil Energy Rate Distribution

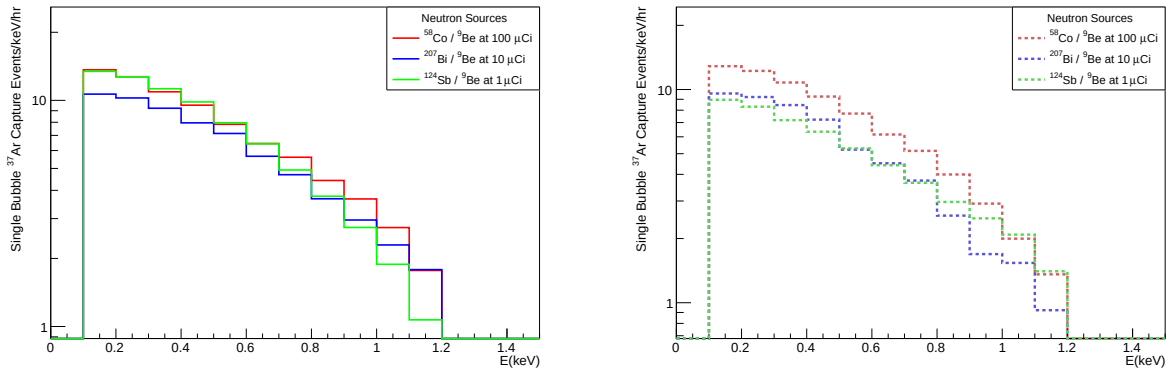

Single Bubble Elastic Events Nucleus Recoil Energy Rate Distribution

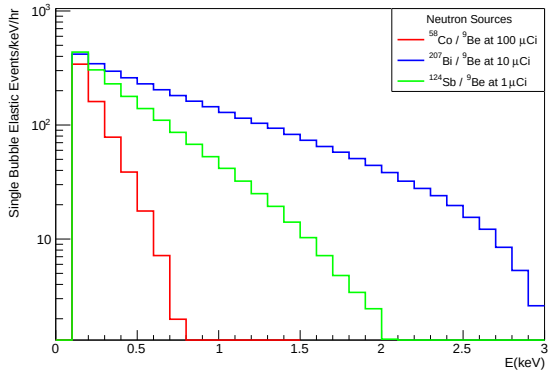

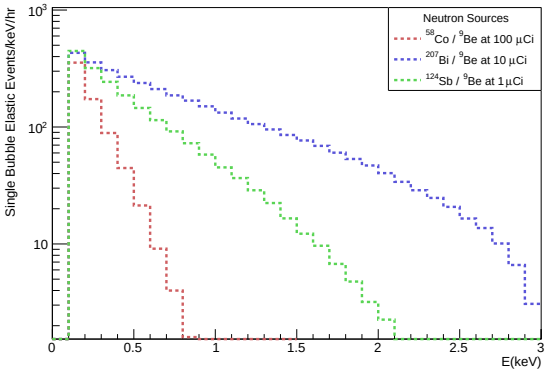

Single Bubble ^{40}Ar Events Nucleus Recoil Energy Rate Distribution

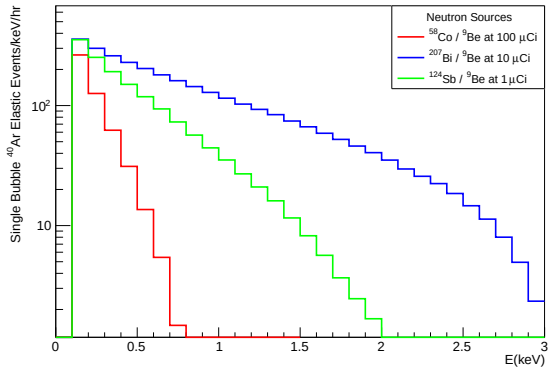

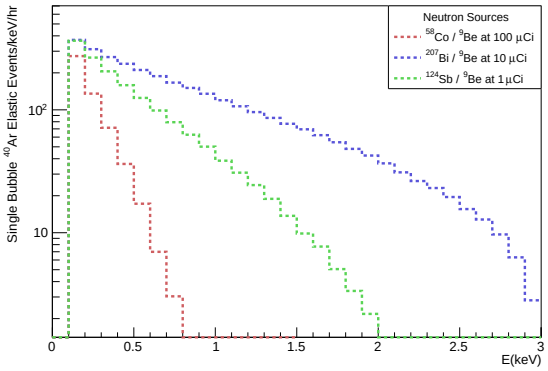

Single Bubble ^{36}Ar and ^{38}Ar Events Nucleus Recoil Energy Rate Distribution

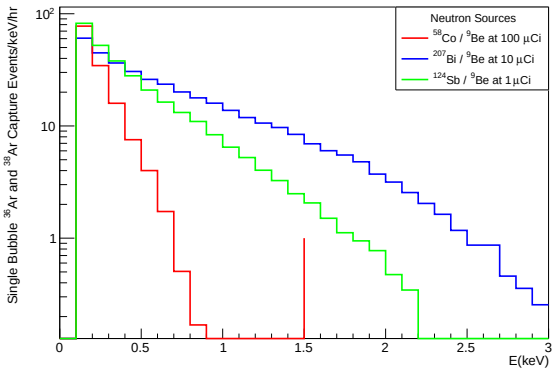

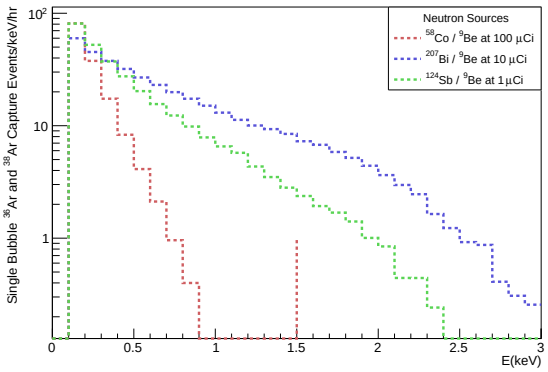

Single Bubble Capture Events

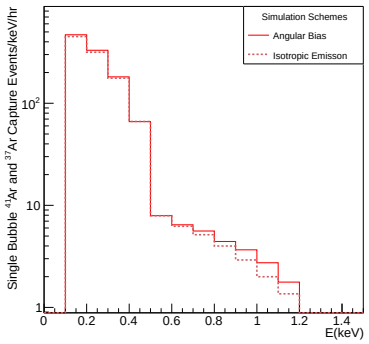

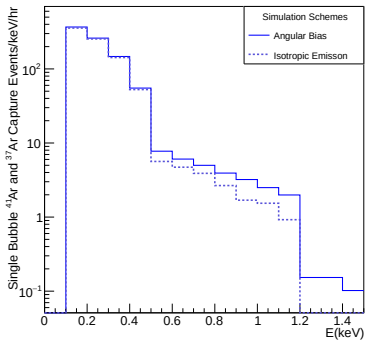

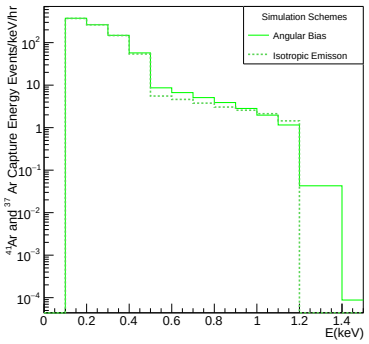

Single Bubble ^{41}Ar Capture Events

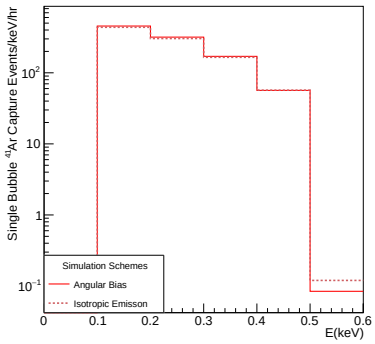

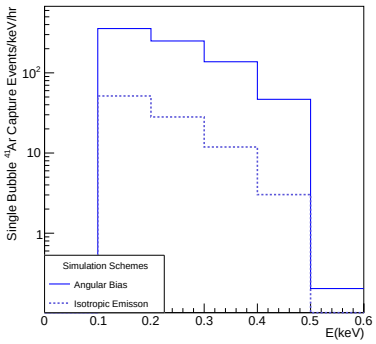

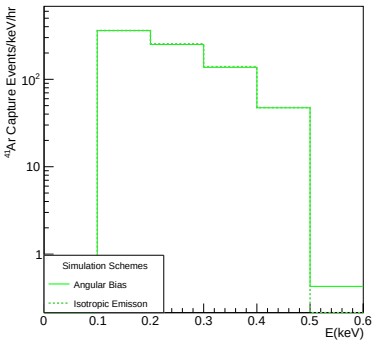

Single Bubble ^{37}Ar Capture Events

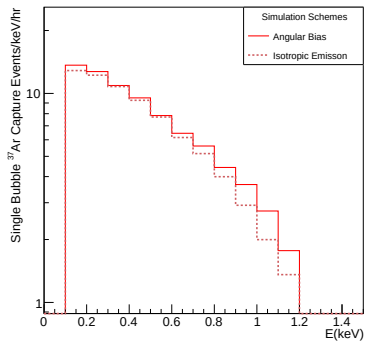

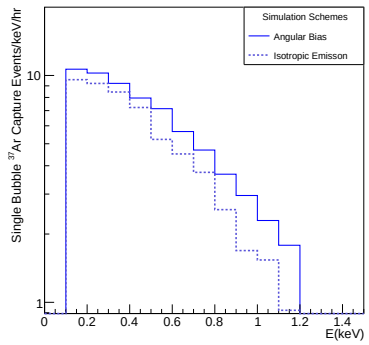

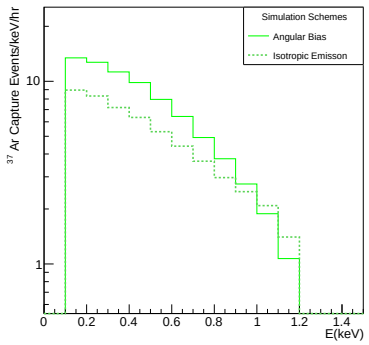

Single Bubble ^{40}Ar Elastic Events

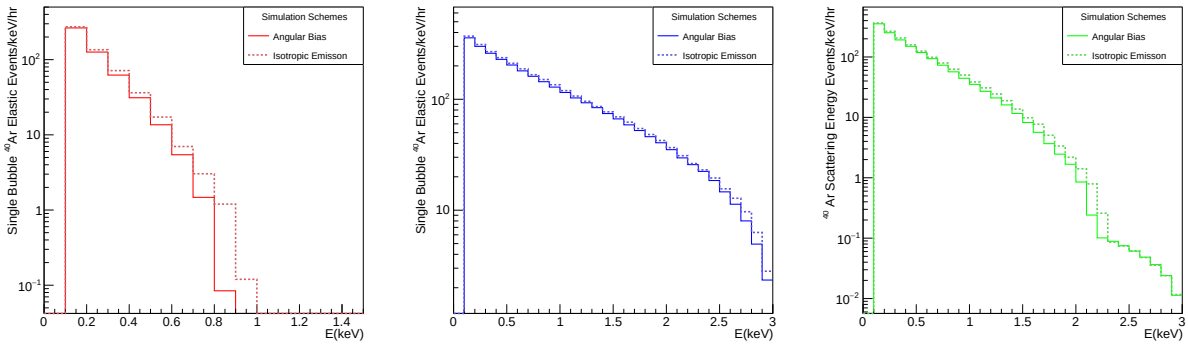

Single Bubble ^{38}Ar and ^{36}Ar Elastic Events

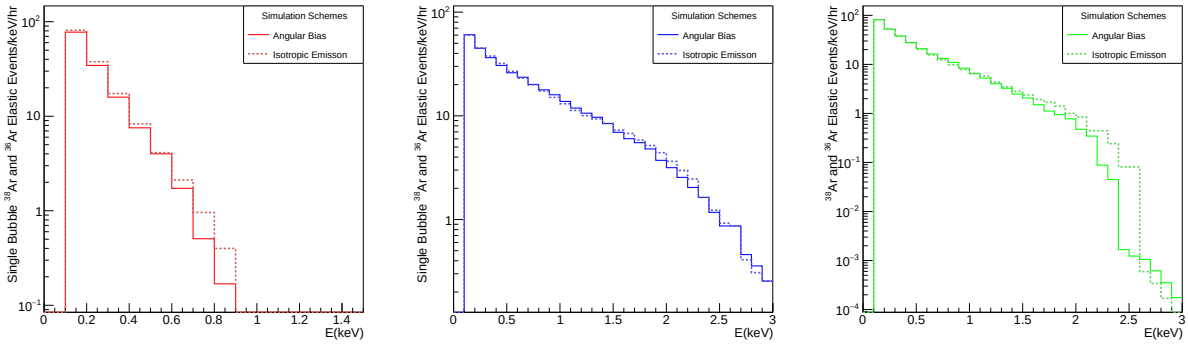

References

[1] F. Zwicky. On the Masses of Nebulae and of Clusters of Nebulae. , 86:217, October 1937.

[2] B. Ryden. *Introduction to Cosmology*. Cambridge University Press, 2017.

[3] Stefano Profumo, Leonardo Giani, and Oliver F. Piattella. An introduction to particle dark matter, 2019.

[4] Measurement of the coherent elastic neutrino-nucleus scattering cross section on csi by coherent. *Phys. Rev. Lett.*, 129:081801, Aug 2022.

[5] C. Andreopoulos et.al K. Kodama, N. Ushida. Observation of tau neutrino interactions. *Physics Letters B*, 504(3):218–224, apr 2001.

[6] A. W. P. Poon. Neutrino observations from the sudbury neutrino observatory. In *AIP Conference Proceedings*. AIP, 2002.

[7] T. Kajita, E. Kearns, and M. Shiozawa. Establishing atmospheric neutrino oscillations with super-kamiokande. *Nuclear Physics B*, 908:14–29, 2016. Neutrino Oscillations: Celebrating the Nobel Prize in Physics 2015.

[8] KATRIN Collaboration. First direct neutrino-mass measurement with sub-ev sensitivity, 2021.

[9] Planck Collaboration. iplanck/i2018 results. *Astronomy &amp Astrophysics*, 641:A6, sep 2020.

[10] FASER Collaboration. First direct observation of collider neutrinos with FASER at the LHC. *Physical Review Letters*, 131(3), jul 2023.

[11] IceCube Collaboration. The IceCube neutrino observatory: instrumentation and online systems. *Journal of Instrumentation*, 12(03):P03012–P03012, mar 2017.

[12] MINERvA Collaboration. Minerva neutrino detector response measured with test beam data, 2015.

[13] Martin Tzanov. Review of Neutrino Deep Inelastic Scattering Results. *AIP Conference Proceedings*, 1222(1):243–247, 03 2010.

[14] COUPP PICASSO and PICO collaboration. Picasso, coupp and pico - search for dark matter with bubble chambers. *EPJ Web of Conferences*, 95:04020, 2015.

[15] P. B. Cushman D. S. Akerib and et. al C. E. Dahl. Snowmass2021 cosmic frontier dark matter direct detection to the neutrino fog, 2022.

[16] L. J. Flores, Eduardo Peinado, E. Alfonso-Pita, and et. al. Physics reach of a low threshold scintillating argon bubble chamber in coherent elastic neutrino-nucleus scattering reactor experiments. *Phys. Rev. D*, 103:L091301, May 2021.

[17] SBC Collaboration. Snowmass 2021 scintillating bubble chambers: Liquid-noble bubble chambers for dark matter and ceνns detection, 2022.

[18] SBC Collaboration. Snowmass 2021 scintillating bubble chambers: Liquid-noble bubble chambers for dark matter and ceνns detection, 2022.

[19] *Handbook on Photonuclear Data for Applications Cross-sections and Spectra*. Number 1178 in TECDOC Series. INTERNATIONAL ATOMIC ENERGY AGENCY, Vienna, 2000.

[20] J. I. Collar. Applications of an ^{88}**Y**/Be photoneutron calibration source to dark matter and neutrino experiments. *Phys. Rev. Lett.*, 110:211101, May 2013.

[21] Alan E. Robinson. New libraries for simulating neutron scattering in dark matter detector calibrations. *Phys. Rev. C*, 89:032801, Mar 2014.

[22] Jonathan L. Feng. Dark matter candidates from particle physics and methods of detection. *Annual Review of Astronomy and Astrophysics*, 48(1):495–545, 2010.

[23] Francis Halzen and Spencer R. Klein. Invited review article: IceCube: An instrument for neutrino astronomy. *Review of Scientific Instruments*, 81(8), aug 2010.

[24] Michael Riordan. *Pauli's Ghost: The Conception and Discovery of Neutrinos*, pages 1–16. Springer Berlin Heidelberg, Berlin, Heidelberg, 2001.

[25] C. L. Cowan, F. Reines, F. B. Harrison, H. W. Kruse, and A. D. McGuire. Detection of the free neutrino: A Confirmation. *Science*, 124:103–104, 1956.

[26] Carlo Giunti and Kim Chung Wook. *Fundamentals of Neutrino Physics and Astrophysics*. Oxford Univ., Oxford, 2007.

[27] Oleksandr Tomalak and Richard J. Hill. Theory of elastic neutrino-electron scattering. *Physical Review D*, 101(3), feb 2020.

[28] Jan T. Sobczyk, S. K. Singh, J. G. Morfin, Makoto Sakuda, and K. D. Purohit. Quasi-elastic neutrino scattering—an overview. In *AIP Conference Proceedings*. AIP, 2011.

[29] G. Danby, J-M. Gaillard, K. Goulianos, L. M. Lederman, N. Mistry, M. Schwartz, and J. Steinberger. Observation of high-energy neutrino reactions and the existence of two kinds of neutrinos. *Phys. Rev. Lett.*, 9:36–44, Jul 1962.

[30] Kapil Saraswat, Prashant Shukla, Vineet Kumar, and Venktesh Singh. Coherent pion production in neutrino-nucleus scattering. *Physical Review C*, 93(3), mar 2016.

[31] Paul Kyberd, David Smith, L. Coney, and at. al Pascoli. nustorm: Neutrinos from stored muons. 06 2012.

[32] M. Abdullah et al. Coherent elastic neutrino-nucleus scattering: Terrestrial and astrophysical applications. 3 2022.

[33] E. Alfonso-Pita, L. J. Flores, Eduardo Peinado, and E. Vázquez-Jáuregui. New physics searches in a low threshold scintillating argon bubble chamber measuring coherent elastic neutrino-nucleus scattering in reactors. *Phys. Rev. D*, 105:113005, Jun 2022.

[34] Chenguang Su, Qian Liu, and Tianjiao Liang. CENS experiment proposal at CSNS. In *NuFACT 2022*. MDPI, jul 2023.

[35] Testing wimps to the limit. https://cerncourier.com/a/testing-wimps-to-the-limit/. Accessed: 2023-09-30.

[36] G. Barello, Spencer Chang, and Christopher A. Newby. A model independent approach to inelastic dark matter scattering. *Physical Review D*, 90(9), nov 2014.

[37] Gary Steigman, Basudeb Dasgupta, and John F. Beacom. Precise relic WIMP abundance and its impact on searches for dark matter annihilation. *Physical Review D*, 86(2), jul 2012.

[38] Kalle Ala-Mattinen and Kimmo Kainulainen. Precision calculations of dark matter relic abundance. *Journal of Cosmology and Astroparticle Physics*, 2020(09):040–040, sep 2020.

[39] Mark W. Goodman and Edward Witten. Detectability of certain dark-matter candidates. *Phys. Rev. D*, 31:3059–3063, Jun 1985.

[40] Guillaume Giroux. Search for dark matter with the pico-500 experiment. *Journal of Physics: Conference Series*, 2156(1):012068, dec 2021.

[41] Andrzej K. Drukier, Katherine Freese, and David N. Spergel. Detecting cold dark-matter candidates. *Phys. Rev. D*, 33:3495–3508, Jun 1986.

[42] David N. Spergel. Motion of the earth and the detection of weakly interacting massive particles. *Phys. Rev. D*, 37:1353–1355, Mar 1988.

[43] Annika H.G. Peter, Vera Gluscevic, Anne M. Green, Bradley J. Kavanagh, and Samuel K. Lee. Wimp physics with ensembles of direct-detection experiments. *Physics of the Dark Universe*, 5-6:45–74, 2014. Hunt for Dark Matter.

[44] Martin Hoferichter, Philipp Klos, Javier Mené ndez, and Achim Schwenk. Analysis strategies for general spin-independent WIMP-nucleus scattering. *Physical Review D*, 94(6), sep 2016.

[45] P. Pirinen, J. Kotila, and J. Suhonen. Spin-dependent wimp-nucleus scattering off 125te, 129xe, and 131xe in the microscopic interacting boson-fermion model. *Nuclear Physics A*, 992:121624, 2019.

[46] Aldo Ianni. Solar neutrinos and the solar model. *Physics of the Dark Universe*, 4:44–49, 2014. DARK TAUP2013.

[47] Joel Kostensalo, Jouni Suhonen, and K. Zuber. Calculated solar-neutrino capture rate for a radiochemical-based solar-neutrino detector. *Physical Review C*, 101(3), mar 2020.

[48] Anna M. Suliga. Diffuse supernova neutrino background. In *Handbook of Nuclear Physics*, pages 1–18. Springer Nature Singapore, 2022.

[49] T. K. Gaisser. Atmospheric neutrino event rates: The expectations. *Philosophical Transactions: Physical Sciences and Engineering*, 346(1678):75–84, 1994.

[50] Ciaran A. J. O'Hare. New definition of the neutrino floor for direct dark matter searches. *Phys. Rev. Lett.*, 127:251802, Dec 2021.

[51] J. I. Collar E. Behnke and et.al P. S. Cooper. Spin-dependent WIMP limits from a bubble chamber. *Science*, 319(5865):933–936, feb 2008.

[52] Zhen Cao, Zan Wu, Mohammad Faghri, and Bengt Sundén. Chapter two - coating engineering for boiling heat transfer toward immersion cooling. volume 53 of *Advances in Heat Transfer*, pages 97–158. Elsevier, 2021.

[53] S Archambault, F Aubin, M Auger, M Beleshi, E Behnke, J Behnke, B Beltran, K Clark, X Dai, M Das, A Davour, F Debris, J Farine, M-H Genest, G Giroux, R Gornea, R Faust, H Hinnefeld, A Kamaha, C Krauss, M Lafrenière, M Laurin, I Lawson, C Leroy, C Lévy, L Lessard, I Levine, J-P Martin, S Kumaratunga, R MacDonald, P Nadeau, A Noble, M-C Piro, S Pospisil, N Starinski, I Stekl, N Vander Werf, U Wichoski, V Zacek, and (The PICASSO Collaboration). New insights into particle detection with superheated liquids. *New Journal of Physics*, 13(4):043006, apr 2011.

[54] Frederick Seitz. On the Theory of the Bubble Chamber. *The Physics of Fluids*, 1(1):2–13, 01 1958.

[55] Dark matter search results from the pico-60 cf_3I bubble chamber. *Phys. Rev. D*, 93:052014, Mar 2016.

[56] Data-driven modeling of electron recoil nucleation in pico c_3f_8 bubble chambers. *Phys. Rev. D*, 100:082006, Oct 2019.

[57] Stopping powers for electrons and positrons. [26 elements, 49 compounds and mixtures]. 10 1984.

[58] J. L. Brown, D. A. Glaser, and M. L. Perl. Liquid xenon bubble chamber. *Phys. Rev.*, 102:586–587, Apr 1956.

[59] Gert Harigel, Gerhard Linser, and Ferdinand Schenk. Operation of a bubble chamber filled with argon, nitrogen, and argonnitrogen mixtures. *Nuclear Instruments and Methods in Physics Research*, 187(2):363–369, 1981.

[60] J. Lindhard and M. Scharff. Energy dissipation by ions in the kev region. *Phys. Rev.*, 124:128–130, Oct 1961.

[61] D. Baxter, C. J. Chen, M. Crisler, T. Cwiok, C. E. Dahl, A. Grimsted, J. Gupta, M. Jin, R. Puig, D. Temples, and J. Zhang. First demonstration of a scintillating xenon bubble chamber for detecting dark matter and coherent elastic neutrino-nucleus scattering. *Phys. Rev. Lett.*, 118:231301, Jun 2017.

[62] V.P Skripov, V.G Baidakov, and A.M Kaverin. Nucleation in superheated argon, krypton and xenon liquids. *Physica A: Statistical Mechanics and its Applications*, 95(1):169–180, 1979.

[63] M. J. Bressler. *Operation and Calibration of Right-Side-Up Bubble Chambers at keV Thresholds: Towards New Superheated Dark Matter Searches.* PhD thesis, 2022.

[64] Ernesto Alfonso-Pita, Edward Behnke, and et.al Bressler. Scintillating bubble chambers for rare event searches. *Universe*, 9(8), 2023.

[65] Pietro Giampa. The Scintillating Bubble Chamber (SBC) Experiment for Dark Matter and Reactor CEvNS. *PoS*, ICHEP2020:632, 2021.

[66] M. Bressler, P. Campion, V.S. Cushman, A. Morrese, J.M. Wagner, S. Zerbo, R. Neilson, M. Crisler, and C.E. Dahl. A buffer-free concept bubble chamber for PICO dark matter searches. *Journal of Instrumentation*, 14(08):P08019–P08019, aug 2019.

[67] Sandra C. Greer and Lothar Meyer. CF4: Crystal Structure and Solid Phase Diagram with Ar. *The Journal of Chemical Physics*, 51(10):4583–4586, 09 2003.

[68] A. W. Bradley. *LUX Thermosyphon Cryogenics and Radon-Related Backgrounds for the First WIMP Result*. PhD thesis, 2014.

[69] D Akimov, V Belov, A Burenkov, A Konovalov, A Kumpan, D Rudik, and G Simakov. Study of xe-doping to lar scintillator. *Journal of Physics: Conference Series*, 798(1):012210, jan 2017.

[70] Ardid M. Arnquist I. J. et.al Amole, C. Dark matter search results from the complete exposure of the pico-60 c_3f_8 bubble chamber. *Phys. Rev. D*, 100:022001, Jul 2019.

[71] Alan E. Robinson. Coherent photon scattering background in sub gev direct dark matter searches. *Physical Review D*, 95(6), mar 2017.

[72] R. L. Macklin, R. R. Winters, and D. M. Schmidt. Resonance neutron capture by argon-40. , 216(1-2):109–112, June 1989.

[73] D. E. Sinclair and O. K. Manuel. Argon-36 from neutron capture on chlorine in nature. *Zeitschrift für Naturforschung A*, 29(3):488–492, 1974.

[74] D. Durnford. Phenomenological studies and analysis techniques to search for light dark matter with news-g, 2018.

[75] D. J. Temples, J. McLaughlin, J. Bargemann, D. Baxter, A. Cottle, C. E. Dahl, W. H. Lippincott, A. Monte, and J. Phelan. Measurement of charge and light yields for 127xe l-shell electron captures in liquid xenon. *Physical Review D*, 104(11), dec 2021.

[76] Ilya Obodovskiy. Chapter 19 - neutron sources. In Ilya Obodovskiy, editor, *Radiation*, pages 289–292. Elsevier, 2019.

[77] Hans Bichsel and T. W. Bonner. Reactions $li^7(\alpha, n)b^{10}$, $li^7(\alpha, \alpha')li^{7*}$, and $b^{10}(n, \alpha)li^7$. *Phys. Rev.*, 108:1025–1027, Nov 1957.

[78] V.A. Kudryavtsev, P. Zakhary, and B. Easeman. Neutron production in (,n) reactions. *Nuclear Instruments and Methods in Physics Research Section A: Accelerators, Spectrometers, Detectors and Associated Equipment*, 972:164095, 2020.

[79] Douglas A. Fynan. Photoneutron reaction kinematics and error of commonly used approximations. *Nuclear Instruments and Methods in Physics Research Section A: Accelerators, Spectrometers, Detectors and Associated Equipment*, 977:164271, 2020.

[80] H. Utsunomiya, S. Katayama, I. Gheorghe, S. Imai, H. Yamaguchi, D. Kahl, Y. Sakaguchi, T. Shima, K. Takahisa, and S. Miyamoto. Photodisintegration of ^{9}Be through the $1/2^+$ state and cluster dipole resonance. *Phys. Rev. C*, 92:064323, Dec 2015.

[81] M. Fujishiro, T. Tabata, K. Okamoto, and T. Tsujimoto. Cross section of the reaction 9be(, n) near threshold. *Canadian Journal of Physics*, 60(11):1672–1677, 1982.

[82] B. Čujec. Photonuclear effect with be9. *Nuclear Physics*, 37:396–411, 1962.

[83] D. E. Alburger, R. E. Chrien, R. J. Sutter, and J. F. Wishart. Search for the three-body photodisintegration of be. *Phys. Rev. C*, 70:064611, Dec 2004.

[84] Alan E. Robinson. Reanalysis of radioisotope measurements of the $^9\mathrm{Be}(\gamma, n)^8\mathrm{Be}$ cross section. *Phys. Rev. C*, 94:024613, Aug 2016.

[85] Alan E. Robinson. *Dark Matter Limits from a 2L C3F8 filled bubble chamber*. PhD thesis, 2015.

[86] Eugene Guth and Charles J. Mullin. Theory of the photo- and electrodisintegration of be^9. *Phys. Rev.*, 76:234–244, Jul 1949.

[87] W. Czyż. Angular distribution of neutrons from the be$^9(\gamma, n)$be^8 reaction. *Phys. Rev.*, 102:1185–1185, May 1956.

[88] B. P. Fabricand, B. A. Allison, and J. Halpern. Angular distribution of photoneutrons from carbon and beryllium. *Phys. Rev.*, 103:1755–1757, Sep 1956.

[89] et.al S. Agostinelli. Geant4—a simulation toolkit. *Nuclear Instruments and Methods in Physics Research Section A: Accelerators, Spectrometers, Detectors and Associated Equipment*, 506(3):250–303, 2003.

[90] K. Sigman. Acceptance-rejection method. http://www.columbia.edu/ ks20/4703-Sigman/4703-07-Notes-ARM.pdf, 2007. Accessed: 2023-06-21.

[91] Jack B Kuipers. *Quaternions and rotation sequences: a primer with applications to orbits, aerospace and virtual reality*. Princeton Univ., Princeton, NJ, 1999.

[92] N.R. Brereton. Corrections for interfering isotopes in the40ar/39ar dating method. *Earth and Planetary Science Letters*, 8(6):427–433, 1970.